Understanding defect related luminescence processes in wide bandgap materials using low temperature multi-spectroscopic techniques

Prasad, Amit Kumar

Publication date:
2017

Document Version
Publisher's PDF, also known as Version of record

Understanding defect related luminescence processes in wide bandgap materials using low temperature multi-spectroscopic techniques

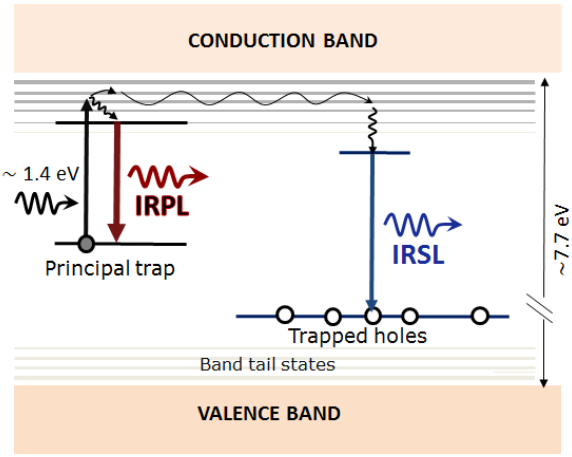

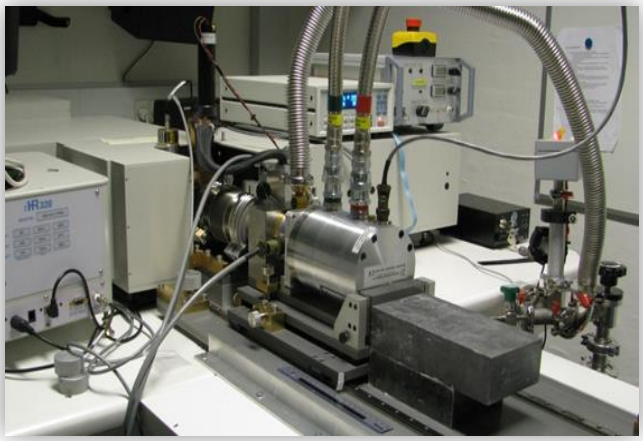

Amit Kumar Prasad

Ph.D. Thesis

January 2017

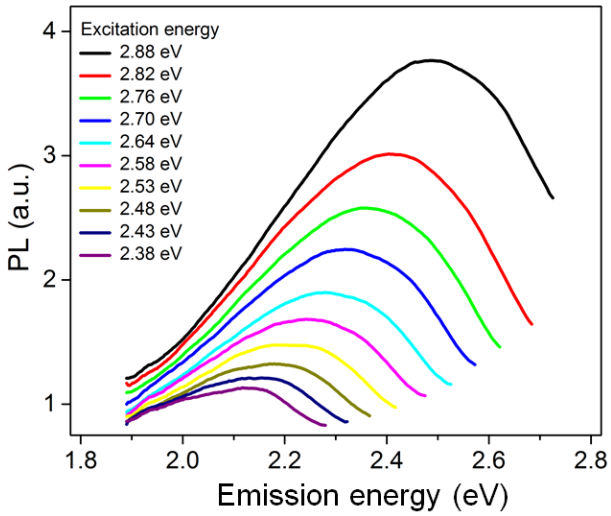

DTU Nutech
Center for Nuclear Technologies

Understanding defect related luminescence processes in wide bandgap materials using low temperature multi-spectroscopic techniques

Amit Kumar Prasad

Ph.D. Thesis
January 2017

DTU Nutech
Center for Nuclear Technologies

Contents

Dedicated to my beloved parents and all well wishers

"Look at the sky. We are not alone. The whole universe is friendly to us and conspires only to give the best to those who dream and work."

-A. P. J. Abdul Kalam

"Have no fear of perfection; you'll never reach it. Nothing in life is to be feared; it is only to be understood."

-Madam Marie Curie

Preface

This dissertation is submitted as a partial fulfillment of the requirement for the Ph.D. degree in Physics, at the Technical University of Denmark (DTU). The Ph.D. research work was carried out at Luminescence physics laboratory at DTU Nutech from 1st November 2013 to 31st January 2017. The project was supervised by Senior Scientist Mayank Jain, Ph.D. (Main supervisor) from 1st November 2013 to 31st January 2017, and Senior R & D Engineer Torben Lapp, Ph.D. from 1st November 2013 to 30th April 2016 (co-supervisor).

Acknowledgements

I am grateful to all the people who have generously shared their time and considerable talent to help me to achieve my goal. They have made my stay in Denmark forever memorable.

First of all, I would like to express my sincere gratitude to my supervisor, Dr. Mayank Jain, for giving me this opportunity to pursue doctoral study under his esteemed supervision. This research would not have been possible without his constant guidance, sharing of knowledge and ideas, and encouragement. He helped me in my learning process and gave me confidence and motivation to be always ready for new challenges. His ever-friendly yet caring attitude, supported me to explore new ideas and pursue them until the end; he encouraged me to become an independent researcher. I am deeply indebted to him for all his support for a successful completion of my Ph.D. thesis.

It is my pleasure to thank my co-supervisor Dr. Torben Lapp for all

his support from the beginning of my Ph.D. until his retirement, and for helping me with his knowledge in instrumentation. His guidance helped me immensely in the early 'instrumentation phase' of my research. I am deeply grateful for all his support.

It is my pleasure to thank Dr. Myungho Kook for all his support on instrumentation/software, for introducing me Zemax, and for his encouragement. I am deeply grateful for all his support.

It is my pleasure to thank Dr. Nigel Poolton for all his support on instrumentation, for introducing and teaching me the luminescence processes of metastable defect states, for sharing his knowledge, and for his encouragement. I am deeply grateful for all his support.

It is my pleasure to thanks Dr. Bent Lauritzen and Dr. Jens-Peter Lynov for their support and encouragement. It is my pleasure to thanks Ms. Pia Elhauge and Ms. Merete Holmegaard Larsen for their support on Ph.D. official matters.

It is my pleasure to thank Dr. Jan-Pieter Buylaert and Dr. Reza Sohbati for their support, encouragement, proof reading and for sharing their feldspars samples. My sincere thanks to Prof. Andrew Murray and Dr. Kristina Thomsen for support and encouragement.

It is my pleasure to thank Mr. Karsten Bracht Nielsen for software of spectroscopy data analysis; Mr. Søren Vig Dalsgaard for opto-mechanics; Mr. Jørgen Hesselbjerg Jakobsen, Mr. Lars Peter Pirtzel, Mr. Per Günther Sørensen and Mr. Bo Dalbjerg for electronics; Mr. Finn Jørgensen for computer related issues; and Mr. Ole Flyvbjerg and to Mr. Minqiang Bu for general support. It is my pleasure to thanks Ms. Louise Maria Helsted. Ms. Vicki Hansen, Ms. Eunyoung Yeo, Ms. Sannie Herleen Hoffgaard for their support and encouragement.

My special thanks to Dr. Per Roos for his help with ICP-MS experiments. It is my pleasure to thank Dr. Claus Andersen, Dr. Lars Lindvold, Dr. Erik Nonbøl, for support and encouragement. My sincere thanks to Ms. Nina Jensen, Ms. Linda Bohn and Prof. Arne Miller for helping me to irradiate my samples with the gamma facility. It is my pleasere to thank Dr. Franciscus Winfried for his help with MATLAB.

I would like to thank to Siritron, Nicola, Nicolai, Rocio, Trine, Martin, Grichar, Nicolo, Jeppe, Raju, and Dr. Xiao Xiao Cai, for their support and friendship. It is my pleasure to express my special thank to Jeppe and Raju for the great last-minute support with their expertise in LaTeX and proof reading of the thesis. My sincere thanks to a large

number of visiting researchers to our laboratory during my Ph.D., for their friendship and support. I also thank the DTU library staff for their support.

I extend thanks to all friends and people from DTU Risø, and DTU Lyngby for their support and encouragement.

It is my pleasure to thank Ms. Grete and Mr. Torben for being a supportive landlord. I extend my thanks to all the researchers, whom I met in conferences for their encouragement.

It is my pleasure to thanks Dr. Sumiko Tsukamoto of LIAG, Hannover, who hosted me in her laboratory as a visiting research student, for teaching me the ESR technique, and for sharing her feldspar samples. I gratefully acknowledge Idella foundation for a visit grant, which covered my stay at LIAG. I would like to extend my thanks to all the members of the section - S3 of LIAG for their support and friendship.

My sincere thanks to Prof. A. V. Gopal and Prof. S. S. Prabhu, who happily offered me the facilities to do some experiments with femtosecond pump probe spectroscopy at TIFR, Mumbai. I also thank the entire group member of FOTON for their support and friendship.

I am expressing my gratitude to my Optics and Photonics teachers Prof. V. P. N. Nampoori, Prof. C. P. Grijavallabhan, Prof. P. Radhakrishnan, Dr. Sheenu Thomas, Dr. Rama chari, Prof. S. Umapathy, Dr. P. K. Gupta, Dr. S. Venugopal Rao for their all-time support and encouragement.

My special thanks to Sunil bhaiya who introduced me to some of the teachings of Swami Vivekananda, which gave me good energy at all times. My thanks to Maumita didi for her support and encouragement. I have been very lucky to have good friends, my love to you all.

I am deeply grateful to my parents, my family and relatives, who have always supported whichever path I have chosen in my life, and given me faith in myself to accomplish tasks set out before me.

At finally and very importantly, it is my pleasure to thank all the people I know but have forgotten to mention here. At the end, I appreciate your time for reading this thesis; my special thanks to you.

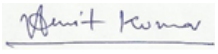

Amit Kumar Prasad
DTU Nutech, Roskilde-4000 (Denmark)
07/08/2017

Abstract

Feldspar is a dominant, naturally occurring mineral which comprises about $\sim 60\%$ of the Earth's crust. It is widely used in optically stimulated luminescence (OSL) dating of sediments to obtain chronologies of past events as old as ~ 0.5 Ma, and thus, plays a crucial role in understanding Quaternary climate changes, landscape development and human evolution and dispersal. Optical properties of feldspar originate from a) a wide band gap ($\sim 7.7\,\mathrm{eV}$, b) crystal defects (impurity atoms and distortions) that create localized energy states within the bandgap, and c) the low-mobility band tail states, which play a role in charge transport. The main defect used in optical dating is called the infra-red dosimetric trap (IR trap), which has a thermal lifetime of millions of years, appropriate for dating Middle to Late Quaternary time scales. However, this trap is known to suffer from instability arising from tunneling loss of the trapped electrons over geological time (so called anomalous fading); this gives rise to apparent ages that underestimate the true age. Despite a rapid progress in the infra-red stimulated luminescence (IRSL) dating technique using feldspar, a clear understanding of luminescence processes is still lacking. Some unknown aspects of the feldspar dosimeter system are: the exact electron and hole trapping centers and their physical characteristics, the interaction of defects (charge trapping states) with the crystal lattice, the kinetics of tunneling loss and the time scales of intra-defect transitions. A better understanding of feldspar as a physical system is expected to lead to its improved performance as a luminescence chronometer. The purpose of my Ph.D. research is to improve the understanding of the nature of luminescence generating defects and processes

in feldspar, and to test if the intra-defect relaxation transitions can be successfully exploited to improve the OSL dating technique. My Ph.D. work is entirely experimental. It includes mapping the energy levels of the defects individually and characterizing their emission process, understanding the dynamics of the excited state relaxation and tunneling, and defect interactions with the crystal lattice and the band tail states. All these experiments were carried out using the Risø station for CryOgenic LUminescence Research (COLUR) and a highly sensitive spectrometer attached to the Risø TL/OSL reader.

Chapter 1 is an introduction to the thesis, while Chapter 2 describes the instrumentation and samples used to carry out this research. The key findings of my Ph.D. research are summarized in five different chapters (Chapter 3 to Chapter 7). I discovered a 'red edge effect' in the green-orange emission in feldspar, and demonstrated that this effect arises from interaction of a deep lying defect with the band tail states. The deep red emission is shown to vary with site dependence of Fe^{3+} even within a single sample. Furthermore, it is observed that there exists an excitation-energy dependence of the main radiative transition ($^4T_1 \rightarrow {}^6A_1$) in Fe^{3+}; this is possibly related to spin-lattice interaction during resonant excitation. I also examined the YPO_4:Ce, Sm system, a model analogue material for feldspar to understand the tunneling mechanism in randomly distributed defects. For the first time, a precise mapping of the energy levels of the metastable Sm^{2+} was carried out, and the temperature-dependent relaxation lifetime of Sm^{2+} excited state was determined using the defects internal radiative-transition mechanism. It was then demonstrated that OSL decay curves resulting from optically induced, sub-conduction band electron transfer ($Sm^{2+} \rightarrow Ce^{4+}$) can be adequately described using the prevalent mathematical model of excited-state tunneling. Finally, inspired by the results of YPO_4:Ce, Sm, I discovered a Stokes shifted infra-red photoluminescence (IRPL) signal in feldspar. Current methods of OSL rely on transfer of electrons from the dosimetric trap to holes located elsewhere in the lattice, which is affected by sensitivity changes leading to several uncertainties in the dose measurement. In contrast, it is shown here that the IRPL signal arises from intra-defect excitation and subsequent radiative emission within the IR dosimetric trap; it is, therefore, not likely to suffer from same problems as the IRSL signal. The IRPL signal, increases with dose and can be probed non-destructively (especially at low temperatures). Preliminary dating

investigations suggest that this signal does not suffer from anomalous fading.

There are two important technique developments in my thesis. Firstly, based on the model of the red edge effect, a simple method is proposed for estimation of the width of the band tail states in feldspar. Secondly, it is shown that the infra-red photoluminescence (IRPL) technique can be used for non-destructive probing of dosimetric information in the IR trap; this signal opens a new window in optical dating methods.

In summary, my research has significantly advanced our understanding of the feldspar luminescence dosimeter system, and has led to development of new measurement techniques, which will significantly impact the future of luminescence dating.

Dansk Resumé

Feldspat er et dominerende, naturligt forekommende mineral, som omfatter ca. $\sim 60\%$ af Jordens skorpe. Det er almindeligt anvendt i optisk stimuleret luminescensdatering (OSL) til at opnå kronologier af tidligere begivenheder op til $\sim$ 0,5 Ma, og spiller derfor en afgørende rolle i forståelsen af kvaternære klimaforandringer, landskabsudvikling og menneskelige evolution og spredning.

Optiske egenskaber af feldspat stammer fra a) et bredt energibånd ($\sim 7.7\,\mathrm{eV}$), b) krystaldefekter (atomare urenheder og forvridninger), der skaber lokaliserede energitilstande i energibåndet, og c) de lavmobile bånd-haler, som spiller en rolle i ladningstransport. Den vigtigste defekt, der anvendes i optisk datering, kaldes den infrarøde dosimetriske fælde (IR-fælde), som har en termisk levetid på millioner af år, er passende til datering af mellem- til sen-kvaternære tidsskalaer. Denne fælde er midlertidig kendt for at være ustabil, da de indfangende elektroner tunnelerer væk over geologisk tid; dette giver anledning til målte aldre, der undervurderer den sande alder.

På trods af hurtige fremskridt indenfor infrarødt stimuleret luminescensdateringsteknik ved hjælp af feldspat, mangler en klar forståelse af luminescensprocessen stadig. Nogle ukendte aspekter af feldspat-dosimetersystemet er: De nøjagtige elektron- og hulfældecentre og deres fysiske egenskaber, interaktioner mellem defekter (ladningsfælder) og krystalgitter, kinetikken bag tab grundet tunnelering, og tidsskalaer af intra-defekt-overgange. En bedre forståelse af feldspat som et fysisk system forventes at føre til, at feldspat bliver et bedre luminescenskronometer.

Formålet med min ph.d.-forskning er at forstå karakteren bag lu-

minescensdefekter og -processer i feldspat, og at teste, hvorvidt intra-defekt-relaksationsovergange kan udnyttes til at forbedre OSL-dateringsteknikken. Mit ph.d.-arbejde er udelukkende eksperimentelt. Det omfatter kortlægning af energiniveauer af de individuelle defekter og karakterisering af deres emissionsprocesser, for at forstå dynamikken i den exciterede tilstands relaksation og tunnelering, og defektvekselvirkninger med krystalgitteret og bånd-hale-stadier. Alle disse eksperimenter blev udført ved anvendelsen af Risø station til CryOgenic LUminescence Research (COLUR), og et højfølsomt spektrometer knyttet til Risø TL / OSL.

Kapitel 1 introducerer min ph.d afhandling og kapitel 2 beskriver instrumenteringen brugt i min forskning. De vigtigste resultater af min ph.d.-forskning er sammenfattet i fem forskellige kapitler (kapitel 3 til 7). Jeg opdagede en 'rød kant-effekt' i den grønne-orange emission i feldspat, og demonstrerede, at denne effekt skyldes interaktion fra en dybt liggende defekt med bånd-hale-stadierne. Det vises, at den dybrøde emission er stedsafhængig af Fe^{3+} placeringen, selv inden for en enkelt prøve. Endvidere ses det, at der eksisterer en eksitations-energiafhængighed af den vigtigste lysdannede overgang ($^4T_1 \rightarrow {}^6A_1$) i Fe^{3+}; dette er muligvis relateret til spin-gitterinteraktion under resonanseksitering. Jeg undersøgte også YPO_4:Ce,Sm-systemet som en analog model til feldspat for at forstå tunneleringsmekanismen i tilfældigt fordelte defekter. Jeg påviste, for første gang, den præcise kortlægning af energiniveauerne af den metastabile Sm^{2+}, og den temperaturafhængige relaksationslevetid af den eksiterede tilstand af Sm^{2+}, ved at benytte defekternes interne lysdannede transitionsmekanisme. Det blev derefter vist, at OSL-henfaldskurver som er resultatet af elektronoverførsel fra optisk induceret sub-ledningsbånd ($Sm^{2+} \rightarrow Ce^{4+}$), kan være tilstrækkeligt beskrevet ved hjælp af den fremherskende matematiske model af eksiteret-tilstand tunnelering.

Endelig, inspireret af resultaterne af YPO_4:Ce,Sm, opdagede jeg en Stokes-skiftet infrarødt fotoluminescenssignal (IRPL) i feldspat. Aktuelle metoder til OSL hviler på overførsel af elektroner fra den dosimetriske fælde til huller lokaliseret andre steder i gitteret. Det er her vist, at IRPL-signalet oprinder fra intra-defekt-eksitation og efterfølgende lysdannede emission inden for den IR-dosimetriske fælde. IRPL-signalet stiger med dosis og kunne måles på en ikke-destruktiv måde (særligt ved lave temperaturer). Foreløbige dateringsundersøgelser tyder på, at dette signal ikke bliver svagere med tiden.

Der er to vigtige teknikudviklinger i min afhandling. For det første, baseret på modellen for den røde kanteffekt, foreslås en simpel metode til estimering af bredden af bånd-haler i feldspat. For det andet er det vist, at IRPL-teknikken kan anvendes til ikke-destruktive måling af dosimetrisk information i IR-fælder; dette signal åbner et nyt vindue i optiske dateringsmetoder.

Sammenfattende har min forskning betydeligt avancerede vores forståelse af feldspat dosimeter systemet, og har ført til udvikling af nye målemetoder, som i væsentlig grad vil påvirke fremtiden for luminescens datering.

List of Publications

Publications based on this thesis:

1. **Prasad, A. K.**, Lapp, T., Kook, M., & Jain, M. (2016). Probing luminescence centers in Na rich feldspar. Radiation Measurements, 90, 292-297.

2. **Prasad, A. K.**, & Jain, M.(Under review). Breakdown of Kasha's Rule in a Ubiquitous Naturally Occurring Aluminosilicate Mineral (Feldspar).

3. **Prasad, A. K.**, & Jain, M.(Under review). Dynamics of the deep red Fe^{3+} photoluminescence emission in feldspar.

4. **Prasad, A. K.**, Kook, M., & Jain, M. (2016). Probing Metastable Sm^{2+} and Optically Stimulated Tunnelling Emission in YPO_4: Ce, Sm. Radiation Measurements (in press).

5. **Prasad, A. K.**, Poolton, N. R. J., Kook, M., & Jain, M.(2017). Optical dating in a new light: A direct, non-destructive probe of trapped electrons. Scientific Reports - Nature (accepted).

Presentations at conferences:

1. **Prasad, A. K.**, Poolton, N.R.J.,Bos, A.J.J., Lapp, T., Kook, M., & Jain, M. (2016).Probing metastable state of Sm^{2+} in YPO_4: Ce^{3+}, Sm^{3+} through tunnelling recombination and direct excitation at cryogenic temperatures. (Oral presentation, 18th International conference on Solid-state dosimetry-SSD, Munich).

2. **Prasad, A. K.**, Tsukamoto, S., & Jain, M. (2016). Multi-spectroscopic characterization of sea salt, gypsum and chewing gum for retrospective dosimetry. (Poster presentation, 18th International conference on Solid-state dosimetry-SSD, Munich).

3. **Prasad, A. K.**, Poolton, N.R.J., Kook, M., & Jain, M. (2016). New method to map the band-tail state in feldspars. (Oral presentation, UK luminescence and ESR Meeting-UKLUM 2016, Liverpool).

4. **Prasad, A. K.**, Jain, M. Poolton, N.R.J., Lapp, T., & Kook, M. (2015).Probing the non-radiative process in Fe^{3+} emission in Na and K rich feldspars. (Oral presentation, 9th International Conference on Luminescent Detectors and Transformers of Ionizing Radiation – LUMDETR 2015, Tartu).

5. **Prasad, A. K.**, Jain, M., Lapp, T., Kook, M. & Poolton, N.R.J. (2015). A comparative study on XEOL, RL, TL, PL and OSL emission spectra of Na and K rich feldspars (Oral presentation, UK luminescence and ESR Meeting-UKLUM 2015, Glasgow)

6. **Prasad, A. K.**, Lapp, T., Kook, M., & Jain, M. (2014). Radio luminescence and dose dependent photoluminescence spectra in feldspars. (Oral presentation, 17th International conference on luminescence and optical spectroscopy of condensed matter -ICL2014, Wroclaw).

Co-authored publications and presentations :

Publications:

1. Jain,M., Sohbati,R.,Guralnik,B., Murray,A.S., Kook,M., Lapp,T. **Prasad, A. K.**, Thomsen,K. J., Buylaert,J. P. (2015). Kinetics of infrared stimulated luminescence from feldspars. Radiation Measurements, Vol.81, 242-250.

Presentations:

1. Nielsen, K. B., Lapp, T., Kook, M.,**Prasad, A. K.**, & Jain, M. Extraction of OSL and TL curves from spatially or spectrally resolved luminescence acquisition. (Poster presentation, UK luminescence and ESR Meeting-UKLUM 2016, Liverpool).

2. Jain, M., Poolton, N.R.J., **Prasad, A. K.**, Lapp, T., Kook, M., & Bos, A.J.J. (2015). A versatile low temperature facility for luminescence measurements. (Poster presentation, 9th International Conference on Luminescent Detectors and Transformers of Ionizing Radiation – LUMDETR 2015, Tartu).

3. Lapp, T., Kook, M., **Prasad, A. K.**, & Jain, M. (2015). A single photon EMCCD based spectrograph system for time-resolved measurements on the Risø TL/OSL Reader. (Oral presentation, UK luminescence and ESR Meeting-UKLUM 2015, Glasgow).

4. Jain, M., **Prasad, A. K.**, Poolton, N.R.J., Lapp, T., & Kook, M. (2015). Cool quartz and feldspars – what can we learn? (Oral presentation, UK luminescence and ESR Meeting-UKLUM 2015, Glasgow).

List of Abbreviations

Ca	Calcium
CB	Conduction Band
CCD	Charge Coupled Device
CL	Cathodoluminescence
COLUR	CryOgenic LUminescence Research
CW-IRSL	Continuous Wave Infrared Stimulated Luminescence
CW-OSL	Continuous Wave Optically Stimulated Luminescence
DOS	Density of States
EMCCD	Electron-Multiplying Charge Coupled Device
ESR	Electron Spin Resonance
FWHM	Full Width Half Maximum
ICPMS	Inductively Coupled Plasma Mass Spectrometry
IL	Ionoluminescence
IR	Infrared
IRPL	Infrared Photo-Luminescence
IR-RF	Infrared Radiofluorescence
IRSL	Infrared Stimulated Luminescence
K	Potassium
LED	Light Emitting Diode
Na	Sodium
OSL	Optically Stimulated Luminescence
PID	Proportional Integral Derivative
pIRIR	Post Infrared Infrared luminescence
PIRSL	Pulsed Infrared Stimulated Luminescence
PL	Photoluminescence
PMT	Photomultiplier Tube
RC	Recombination Centre
RL	Radioluminescence
SAR	Single Aliquot Regenerative Dose Protocol
TCSPC	Time-Correlated Single Photon Counting

TL	Thermoluminescence
UV	Ultra-violet
VB	Valence Band
XEOL	X-Ray Excited Optical Luminescence
XRF	X-Ray Fluorescence
YPO_4:Ce,Sm	Yttrium Phosphate co-doped with Cerium and Samarium

Chapter 1

Introduction and Overview

1.1 Motivation and Purpose

Human excellence is nurtured by our inherent curiosity to know about the past (Gould, 1987). The age determination of geological and archeological events in the last $\sim$ 2.5 million years (the Quaternary period) is critical for understanding past climate and environmental changes, landscape changes, and human evolution and dispersal. This understanding is important for future predictions of climate, environmental changes, and for resource planning. In this connection, the Optical dating technique, a novel and rapidly developing application of Geophotonics, has played an important role in age determination of the archaeological and geological events (e.g., see Aitken, 1998; Rhodes, 2011; Liritzis et al., 2013; Roberts et al., 2015; Duller, 1997). In particular, it has proven to be a highly useful and widely applicable technique for obtaining chronologies for the Late and Middle Pleistocene (e.g., see Buylaert et al., 2008; Rittenour, 2008; Cunha et al., 2012; Herman et al., 2013; Guralnik et al., 2015;Henshilwood et al., 2002; Singhvi and Porat, 2008; Fattahi and Walker, 2007; Wallinga, 2002).

Luminescence dating has done wonders for understanding the past changes on Earth, and has the potential to do the same for the other planetary bodies. For example, there is immense interest to understand

recent climate change and its impact on Mars, and to know if there existed life on this planet. Optical dating has the potential for in-situ dating on Mars using a robotic system (e.g. Kalchgruber et al., 2007; Jain el al., 2006; Banerjee et al., 2002; McKeever et al., 2006). The technique of remote optical dating using robotic systems provides us the possibility to extend our knowledge in Planetary science (Lepper and McKeever,2000). It can also contribute to understanding the interior dynamics of a planet as well as interplanetary events such as a giant asteroid hitting the Earth (e.g., Prescott et al., 2004). However, the success of dating other planetary objects relies heavily on our ability to date accurately using feldspar.

Optical dating is an interdisciplinary technique based on solid state physics, radiation physics, and Earth and archaeological sciences; all these areas have contributed synergistically to the development of the technique. Despite the immense success of the optical dating technique, there are continuous attempts from laboratories across the world to further improve the technique for wider applications. Some of the active research areas are: increasing the accuracy and precision, extending the age range, solving the problem of poor bleaching, and modelling charge build up in thermally and optically dynamic environments. Even a slight improvement in the method can have a significant positive impact on the application of the technique, and on the age resolution of the past events. The researchers rely on the fact that natural minerals such as quartz and feldspars, which are widely used in dating, are rich in luminescent defects and have complex charge transfer processes. It is expected that a better understanding of these defects and processes will give rise to more robust dating methods, and help to place the existing dating protocols on a solid foundation. In comparison to quartz, feldspar is a much more diverse system, not just mineralogically but also in terms of the luminescence generating processes (e.g., Jain and Ankjærgaard, 2011). From this point of view, feldspars are inherently more interesting to study compared to quartz.

The purpose of my Ph.D. research is to understand the nature of luminescent defects and processes in feldspar, and to test if the intra-defect emissions can be successfully exploited in optically stimulated luminescence (OSL) dating. As a student of Photonics, I have always been interested in understanding the optical properties of natural materials. This Ph.D. gave me the opportunity to explore a different application

outside the conventional optics and photonics research; it has been particularly motivating for me to work in an interdisciplinary area which has a significant impact on our effort to understand our past, and thereby our future.

1.2 OSL Dating

Luminescence dating is based on the process called 'stimulated luminescence' from naturally occurring minerals such as quartz and feldspar. The most commonly used form of this technique is optically stimulated luminescence (OSL), where the term 'optical' usually refers to visible light which is commonly used to date quartz (e.g. violet, blue or green wavelengths). In case of feldspar, near infra-red light is used for stimulation giving rise to the infra-red stimulated luminescence (IRSL).

The OSL process was first used for age determination by Huntley et al. (1985), and has since then become one of the most important methods for dating the Late Quaternary (e.g. Rhodes, 2011; Roberts et al., 2015, Duller, 1996). OSL is a two-step process: a) ionization of the lattice by interaction with high-energy radiation, creation of free electrons and holes, and subsequent trapping of these charge carriers at the lattice defects (traps), and b) optical eviction of trapped charge from light sensitive traps followed by a radiative electron-hole recombination resulting in the OSL. The charge trapping centers form localized energy states within the bandgap of the feldspar ($\sim$ 7.7–7.8 eV; Malins et al., 2004) and quartz ($\sim$ 8.3–8.7 eV; Itoh, 1989), thereby providing metastable states to the electrons and holes released by exposure of ionizing radiation. Some of these states depending on the energy potential (trap depth) may have a lifetime of millions of years, which makes them useful for geochronology.

The OSL clock in quartz and feldspar is zeroed by exposure to daylight during erosion and sediment transport prior to burial. After burial, the population of trapped charge increases over time due to the impact of ionizing radiations from the environment (^{238}U, ^{232}Th, ^{40}K and cosmic rays). The geological age (a = annum) of the sample is estimated as the ratio between the absorbed ionizing radiation dose (also known as palaeodose or equivalent dose; unit Gy) and the environmental dose rate (unit Gy.a^{-1}), acquired since the sample was last buried and blocked from daylight (Aitken, 1985, 1994).

1.3 Luminescence processes in feldspars

Since the discovery of IRSL by Hütt et al.(1988), a considerable attention has been given to age determination using feldspar. Feldspar is the most abundant mineral on the Earth's crust; it is an aluminosilicate that occurs as the alkali series (K_x,$Na_{1-x}AlSi_3O_8$) or the plagioclase series (Na_{1-x} $Ca_xAl_{1+x}Si_{3-x}O_8$). In luminescence dating, feldspar is preferable over quartz because of the potential to extend the upper limit of the age range to 0.5 million years (Ma) (e.g. Wintle, 2008; Rhodes, 2011;Duller,1997). However, feldspar suffers from the gradual athermal loss of trapped electrons, a phenomenon termed as anomalous fading, which leads to age under-estimates (Wintle, 1973). Over the last three decades, significant attention has been paid towards understanding the origins of luminescence in feldspar to solve the anomalous fading problem. A detailed description of the feldspar luminescence model is given by Jain and Ankjærgaard (2011). Different aspects of this feldspar model are briefly described in the following subsections. See Figure 1.1 for a simplified illustration.

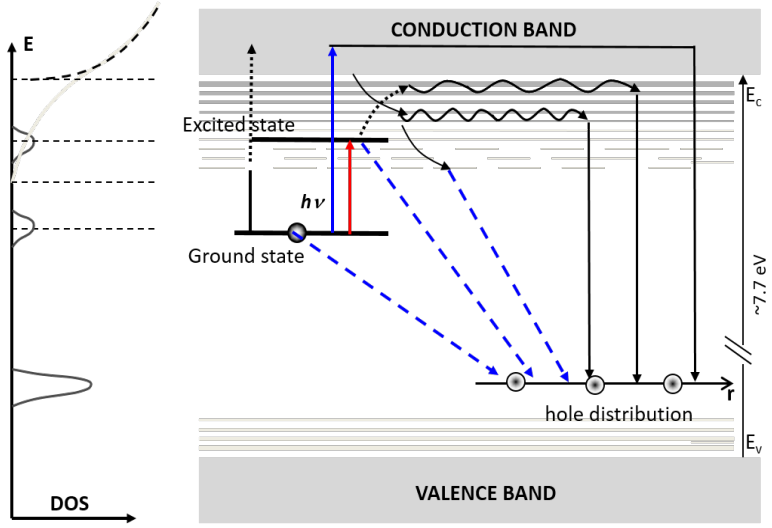

Figure 1.1: Luminescence model of feldspars (modified from Jain and Ankjærgaard, 2011)

1.3.1 The infrared dosimetric trap

The infrared dosimetric trap (hereafter the IR trap) consists of a ground state and an excited state below the conduction band; the excited state gives rise to the IRSL signal. There have been many investigations to understand the IRSL emission process, the nature of the IR dosimetric trap and electron transport dynamics after IR excitation. Optical excitation measurements suggest that the IR dosimetric trap is located well below ($> 2\,\text{eV}$) the conduction band edge, and it is stable over the geological time (e.g. Hütt et al., 1988; Bailiff and Poolton, 1991; Clark and Sanderson, 1994; Baril and Huntley, 2003; Huntley and Lian, 2006; Jain and Ankjærgaard, 2011). Kars et al. (2013) estimated the IR trap depth to be $\sim 2.1\,\text{eV}$ for Na feldspar and $\sim 2.5\,\text{eV}$ for K feldspar using IRSL measurements at 10 K. The question of whether there is one or several IR traps has been debated for a long time (e.g., see Duller, 1997). Excitation spectroscopy at different temperatures and preheat treatments has demonstrated that there is only one IR dosimetric trap that contributes to the IRSL emission (Andersen et al., 2012). This one trap interpretation is further confirmed by theoretical modelling and experimental results involving different emission centers (Jain et al., 2015a).

1.3.2 The band tail states

The bandgap of semiconductors or insulators plays an important role in their optical properties. The random distribution of impurities, structural disorder (local fluctuations of bond length), thermal vibrations and variations in bond angles introduce distortions in the band structure. As a result, the formation of localized energy states takes places towards the valence band and the conduction band edges, leading to the bandgap narrowing. Anderson (1958) first predicted the existence of localized states in disordered material. Mott (1969) demonstrated that any random potential introduces localized states in the tails of the band. The density distribution of band-tail states $\rho(E)$ can be described by the equation (Sritrakool et al., 1986):

$$\rho(E) \propto \exp\left(-E^n/E_B\right) \tag{1.1}$$

Where E is the energy of the state measured away from the band edge, and for n=1 (the Urbach tail; Urbach, 1953), E_B is a constant (commonly

referred to as the band tail width) at which the density falls by e^{-1} of that at the band edge.

Several aspects of feldspar luminescence can be explained by the presence of the low mobility band tail states below the conduction band (Poolton et al., 2002 a, b). These states have a potential impact on charge trapping, thermal stability of trapped electrons, and electron transport subsequent to optical or thermal eviction. It has been shown that the main excited state of the IR electron trap lies within the band tail states (Poolton et al., 2009) and that these states allow phonon-assisted transport of detrapped electrons subsequent to IR or visible light stimulation (Jain and Ankjærgaard, 2011; Andersen et al., 2012). Furthermore, tunneling from the lowest band states is also an important route of charge recombination (Jain and Ankjærgaard, 2011).

The presence of the band tail states affects the measurement of thermal trap depth in feldspar by providing multiple detrapping routes. Li and Li (2013) proposed a thermal eviction model involving the band tail states. The thermal lifetime of the trap (E_t) is decreased by the presence of the band tail of energy E_b in the vicinity of the trap:

$$\tau = s^{-1} \exp\left((E_t - E_b)/kT\right) \tag{1.2}$$

Here, s is the frequency factor, k is the Boltzmann constant and T is the absolute temperature (K). Assuming an exponential distribution of the band tail states, Li and Li (2013) derived the trap depths of the order of $\sim$ 1.9 to 2.1 eV in their sample (Li and Li, 2013). There have also been many attempts to use first-order kinetics without considering the effect of the band tail states; these values, for example, have been found to be in the range of 1.7 eV (Murray et al., 2009), 1.66 eV (Li and Tso, 1997) and 1.8 eV (Li and Li, 2011b).

1.3.3 Anomalous fading

Anomalous fading is a phenomenon of spontaneous decrease in luminescence intensity with time after laboratory irradiation (Wintle, 1973). The underlying physical process of anomalous fading is widely accepted to be quantum mechanical tunneling of electrons from the IR trap to the hole centers (Visocekas et al., 1985), resulting from the overlap between the electron and hole wave functions. Unless properly corrected, this undesirable loss of electrons causes age underestimation (e.g. Spooner, 1994).

Huntley and Lamothe (2001) suggested a fading correction method based on the observed t^{-1} (t: time after irradiation) dependence of tunneling emission (Visocekas, 1979; Aitken, 1985 - Appendix F). Huntley (2006) proposed a more comprehensive model based on nearest neighbor recombination to demonstrate that tunneling law follows a power law decay over several decades of time. Based on the model of Huntley (2006), Kars et al. (2008) suggested a new method of age correction; the advantage of this method is that it can be applied to a wider dose (age) range compared to the linear dose range of the Huntley and Lamothe (2001) model.

Instead of applying model corrections to feldspar ages, a more desirable approach is to find signals that do not suffer from fading. There have been many attempts in search of non-fading signals in the past two decades, for example, the red IRSL (Fattahi and Stokes, 2003), pulsed IRSL (PIRSL; Sanderson and Clark, 1994; Tsukamoto et al., 2006; Jain and Ankjærgaard, 2011; Jain et al., 2015b), post IR-IRSL (pIRIR; Thomsen et al., 2008; Buylaert et al., 2009, 2012; Thiel et al., 2011), Multi elevated temperatures post IR-IRSL (MET-pIRSL; Li and Li, 2011a), thermally redistributed IRSL (RD-IRSL; Morthekai et al., 2015) and IR – RadioFluorescence (IR-RF; Trautmann et al., 1999a,b; Buylaert et al., 2012; Frouin et al., 2017). Although, this is still an active area of research, it appears that the most successful methods are based on signals from trapped electrons that are sufficiently far from recombination sites, and thus do not suffer from anomalous fading during sediment burial. The preferential selection of such electrons can be achieved by sequential excitation techniques, such as in the pIRIR or MET-pIRSL signals, where the prior stimulation removes most of the unstable charge.

1.3.4 Charge transport under IR stimulation

Time-resolved measurements have been used to understand charge transport and relaxation lifetimes of the recombination centers. A range of time constants ranging from ns to ms have been observed in the IRSL process reflecting a range of pathways of electron transport within band tail states (see e.g., Sanderson et al., 1994; Tsukamoto et al., 2006; Clark and Bailiff, 1998; Ankjærgaard and Jain, 2010).

At 10 K the dominant mode of charge transfer is tunneling of the IR-excited electron to the hole centers (Poolton et al., 2009). The extensive work on the electron transport mechanisms using wavelength-

dependent time-resolved measurements by Jain and Ankjærgaard, (2011) gave insights into the dynamics of hopping within the band tail states. It was shown that electron diffusion and its eventual recombination with a trapped hole is dependent on the energy of the band tail states, and that the activation energy for diffusion can be correlated with the phonon modes of the sample. These data contributed to the development of a comprehensive phenomenological model of feldspar luminescence.
Morthekai et al. (2012) further contributed to the understanding of hopping of the IR-excited electrons based on diffusion theory within the band tail states; these authors suggested that a variable-hopping mechanism is in action in time-resolved IRSL processes. There have also been studies to understand the kinetics of the IRSL process. Thomsen et al. (2011) observed that for longer times the IRSL decay shape was independent of stimulation power, possibly reflecting a tunneling phenomenon. Jain et al. (2012) developed a mathematical model to describe tunneling from the excited state; this model is based on the tunneling recombination of excited electrons to a distribution of randomly distributed holes. This model has been successfully tested against several experimental data for temperature dependence (Jain et al., 2015a), thermoluminescence (e.g., Kitis and Pagonis, 2013), continuous wave IRSL (e.g., Jain et al., 2015a; Pagonis et al., 2015) and time-resolved IRSL (e.g., Pagonis et al., 2016).

1.4 Luminescent defects

In order to get insights into the luminescence generating defects it is necessary to investigate the spectral characteristics of luminescence emission. Spectroscopy is a powerful tool to understand defects in semiconductors and insulators. Figure 1.2 shows a simple electronic band structure of wide bandgap materials (such as feldspar) where traps and recombination centers lie within the bandgap of the materials. Some commonly-used spectroscopic techniques in luminescence studies of feldspar can be grouped based on the excitation mode:
(i) Interaction with high-energy radiations: Radioluminescence (RL, typically from beta irradiation), Cathodoluminescence (CL), X-ray Excited Optical Luminescence (XEOL) or Ionoluminescence (IL).
(ii) Interaction with low-energy radiations: Optically Stimulated Luminescence (OSL) or Thermoluminescence (TL).
(iii) Internal defect excitation: Photoluminescence (PL). These tech-

niques and their results on feldspar are briefly described in the following text:

1.4.1 X-ray excited optical luminescence (XEOL) or Radioluminescence (RL)

The excitation with the high-energy particle or X-ray leads to the ionization of the lattice (as this energy is greater than the bandgap of the lattice). The excited electrons are promoted to the conduction band, while leaving a corresponding hole behind in the valence band. Some of the free electrons and holes are trapped within the defect centers, T: Trap (electron trapping center) and RC: Recombination center (hole trapping center), respectively, thus creating their metastable states. Luminescence can be generated via different transitions (Figure 1.2(a)):

- Electrons in the conduction band can recombine with the holes in the valence band to produce the so-called "intrinsic" luminescence (interband transition).

- Electron trapping i.e. transition of electrons from the conduction band to the electron trapping center (T), and

- Recombination of electrons from the conduction band with the trapped holes at RCs.

The spectral distribution of the luminescence emission (emission spectra) gives insights into the radiative recombination/relaxation processes. The basic differences between the CL, XEOL, RL and IL methods arise from the penetration depths of different radiations. CL, for example, typically only accesses the surface of the sample, while the RL samples the full volume. The range of XEOL can vary depending on the X-ray energy.

1.4.2 Optically stimulated luminescence (OSL) or Thermoluminescence (TL)

Upon absorption of sufficient thermal or optical energy, the trapped electron from the trapping centers (T) can be excited to the excited state of the trap (T^*) or to the conduction band. Subsequently, the excited electron can find the trapped hole at the recombination center (RC), via conduction band transport or sub-conduction band tunneling, leading to emission of photons ($RC^* \rightarrow RC$). The resulting signal is called optically stimulated luminescence (OSL) or thermoluminescence (TL) depending upon whether the excitation of trapped electron is optical or thermal,

respectively (Figure 1.2(b)). On prior irradiated samples, one can obtain the OSL excitation spectra, by tuning the excitation energy and monitoring the OSL emission energy in a fixed emission window. On the other hand, keeping a constant excitation energy and scanning the emission energy gives rise to the OSL emission spectra. In case of TL, it is only possible to measure the TL emission spectra during temperature ramp or at constant temperature. Typically, for dosimetric signals, the excitation spectra give insight into the energy levels of the metastable state (trapped electron center), whereas the emission spectra gives information on the energy levels of the recombination site.

1.4.3 Photoluminescence (PL)

The electrons in the ground state of the luminescence center can be optically excited to the higher electronic states. The process of subsequent radiative relaxation to the ground state of the centre gives rise to the photoluminescence (PL) signal (Figure 1.2(c)). PL is a Stokes shifted emission which reflects the resonant radiative relaxation, modified by the vibrational levels of the system. Excitation with selective photon energies can map the discrete energy states of the centre (**site selective probing**). Similar to OSL, one can obtain the PL excitation spectra or PL emission spectra by tuning the excitation or emission energies, respectively.

There have been many studies to understand the luminescence spectra from feldspar. An excellent review of these studies is given in Krbetschek et al. (1997). The principle luminescence bands, the method of excitation, and possible origins are given in the Table 1 (summarised from Krbetschek et al., 1997; Gaft et al., 2015).

Although these data are not exhaustive, it can be seen that the exact defects responsible for electron and hole trapping sites in feldspar are still ambiguous. Furthermore, the defect assignments are often tentative as they are typically based on correlations. The details of the electron trapping sites, in particular, are still elusive.

The luminescence emission during IR excitation occurs in various energy bands $\sim$ 1.7, 2.2, 3.1 and 4.1 eV (see Krbetschek et al., 1997; Baril and Huntley, 2003). Special focus on IRSL spectroscopy suggests that the IRSL emission is influenced by stimulation energy, stimulation temperature and ionizing radiation dose (e.g., see Baril and Huntley, 2003; Rieser et al., 1997; Clarke and Rendell, 1997; Huntley et al., 1991).

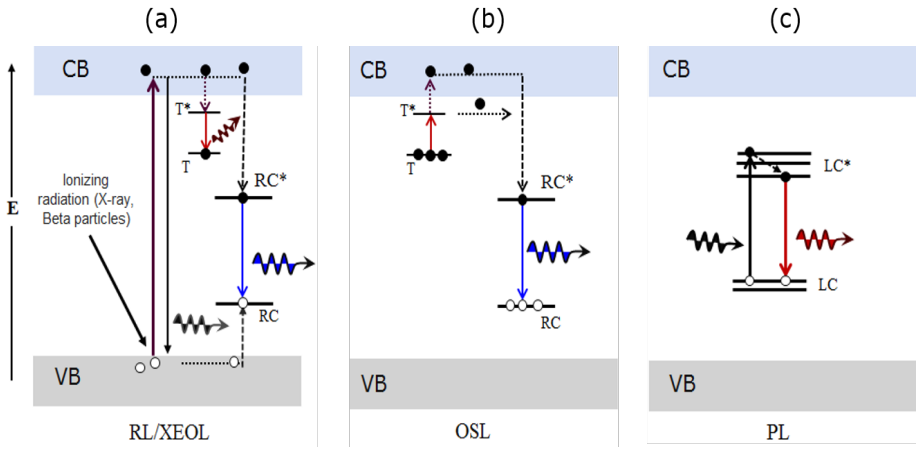

Figure 1.2: Simple band model of a wide bandgap material: (a) the processes of ionization with high energy radiation and subsequent trapping of free electrons and holes (T – electron trap, T^*-excited state of T; RC - recombination center or hole trapping centre, RC^*- excited state of RC; CB - conduction band; VB - valence band). Radiative trapping or prompt electron-hole recombination ($RC^* \rightarrow RC$) gives rise to radioluminescence (RL) or X-ray excited optical luminescence (XEOL). (b) Optically or thermally stimulated detrapping and subsequent recombination giving rise to OSL or TL (c) Photoluminescence: internal luminescence within a luminescence center (LC), LC^* -excited state of LC; this may or may not require a prior exposure to ionizing radiation.

Table 1.1: The main emission bands observed in feldspars. TL: Thermoluminescence, IRSL: Infrared stimulated luminescence, CL: Cathodoluminescence, RL: Radioluminescence, PL: Photoluminescence.

Emission band (eV)	Excitation method	Possible origin	References
$\sim$ 3.8- 4.4 eV (280-320 nm)	TL	Strain and/or ionic diffusion	Garcia-Guinea et al., (1999)
	PL	Tl^{+}	Gorobets et al., (1995)
	IRSL		Baril and Huntley, (2003)
	TR-OSL		Clark and Bailiff, (1998)
$\sim$ 3.1 eV (400 nm)	CL	O Paramagnetic defect	Finch and Klein, (1999)
	IRSL	?	Rieser et al., (1997)
	IRSL	?	Baril and Huntley, (2003)
$\sim$ 2.2 eV (560 nm)	IRSL	Mn^{2+}	Rieser et al., (1997),
	IRSL		Baril and Huntley, (2003)
	CL		Geake et al., (1977)
	TR-OSL		Clark and Bailiff, (1998)
	CL		Telfer and Walker, (1978)
$\sim$ 1.7 eV, (730 nm)	Absorption	Fe^{3+}	White et al., (1986)
	PL		Telfer and Walker, (1975)
	IRSL		Krbetschek et al.,(1996)
	PL		Poolton et al., (1996,2006)
$\sim$ 1.45 eV, (855 nm)	RL	IR dating trap	Trautmann et al., (1999a)
$\sim$ 1.3-1.36 eV, (910 nm)	RL	Pb^{+}	Erfurt, (2003)
	Post IR phosphorescence	IR dating trap	Baril and Huntley, (2003)
	TL	?	Krbetschek and Rieser, (1995)

The most commonly used emission for IRSL dating is the ~ 3.1 eV blue band, which seems to dominantly arise from K-feldspar (Baril and Huntley, 2003) and shows lesser anomalous fading than the UV band (Thomsen et al., 2008). It has also been suggested that the IRSL emission may not only depend on the physical properties of the IR electron trap and the recombination site, but also on the electron transport route (Poolton et al., 2009; Andersen et al., 2012).

1.5 Objective of this Ph.D. research

Despite the rapid progress in IRSL dating in the last decade, the details of the luminescence processes in feldspar are still poorly understood. There are unanswered questions relating to underlying mechanisms of prompt decay (fading) and IRSL production, and their mineralogical dependence. Finding a better understanding of these processes will pave the way for an improved and more reliable optical dating technology. A robust feldspar model is especially important for new applications that involve dynamic evolution of trapped charge such as rock surface dating (e.g. Sohbati, 2015) and thermochronometry (e.g. Guralnik et al., 2015; King et al., 2016). In such applications, it is critical to accurately predict (model) the result of a complex history of simultaneous charge trapping due to ionizing radiation and detrapping due to heat or optical stimulation. However, in order to develop a robust feldspar model it is important to gain knowledge of the physical parameters of the system such as the trap depth, optical cross-section, photon-phonon interaction, width of the band tail states, excited-state lifetime, distribution of luminescence defects, etc. It is non-trivial to obtain such a knowledge since OSL arises from a recombination of electrons with holes; it becomes, therefore, challenging to isolate the electron traps and study their physical characteristics such as the energy structure, trapping and detrapping cross-sections, lifetime, transport dynamics, etc., individually.

Spectroscopy is a powerful tool to study these processes and has had only limited application to understand the dosimetric signals in feldspars. The objective of my Ph.D. is to obtain better understanding of the luminescence generating mechanisms through defect characterisation in feldspar and to develop new improved method(s) of optical dating. The specific objective of my research is to probe and characterise the main luminescence defects/centers in feldspar and its analogue

material (YPO_4:Ce,Sm) using site selective (energy selective) spectroscopic techniques, to characterise the band tail states to study charge (energy) transfer across defects, and to search for the dosimetric photoluminescence signal (Stokes shifted)from the metastable states that may be relevant to luminescence dating.

1.6 Outline of my Ph.D. thesis (research work)

My main research is contained in five chapters, organised as research articles. Three of the articles are published (Chapter 3, 6 and 7) and two are under review (Chapter 4 and 5) . Additionally, there is an introduction chapter (the current chapter), an instrumentation and samples chapter, and a summary and conclusion chapter. The brief thesis outline is presented below.

Chapter 1 (the current chapter): Introduction and overview

This chapter gives a brief background relevant to my research, and presents the objectives and outline of my thesis.

Chapter 2: Instrumentation and Samples

This chapter gives a brief summary of the instrumentation, experimental techniques and samples used in this research. The main facilities used in my study are Risø station for CryOgenic LUminescence Research (COLUR), and a high-sensitivity spectrometer attached to the Risø TL/OSL reader.

The materials used in my research are feldspar samples of different compositions and YPO_4 co-doped with Ce and Sm. The main experimental techniques employed in my research are:

1. Photoluminescence (PL) emission and excitation spectroscopy
2. Time-resolved PL(fluorescence & phosphorescence) measurements
3. Low-temperature investigations ($\geq 7\,K$)
4. Optically stimulated luminescence (OSL) spectroscopy
5. XEOL/RL spectroscopy

These different techniques are used to characterize the defects' electronic transitions, energy transfer and relaxation lifetimes. PL is an important tool to understand the energy structure of the luminescence centers; excitation spectroscopy added details about the energy levels of the tar-

get luminescence defect, whereas the lifetime of the emission has given temporal dynamics of the excited states. The low-temperature measurements have improved our understanding of the non-radiative processes and phonon interactions in the system. OSL spectroscopy has given insight into the charge transport process, the nature of the electron trapping center (excitation spectra) and the nature of the recombination site (emission spectra). XEOL/RL spectroscopy has provided further understanding of the nature of the recombination site.

Chapter 3: Probing luminescence centers in Na-rich feldspar (Published[1])

Chapter 3 presents a study on the use of different techniques to understand the general features of feldspar luminescence. It compares RL, XEOL and PL emission spectra and further explores the site-selective excitation and emission of individual defects and luminescence centers. It also examines the decay dynamics of the different PL emissions. After the general characterization, this study focusses on the excitation-dependent emission energy shift in the orange-green emission (giant 'red-edge effect' observed for the first time in crystals according to my knowledge) and deep-red Fe^{3+} emission (red emission); both aspects are explored in detail in chapters 4 and 5, respectively. Chapter 3 makes a bold suggestion that the orange-green emission may not arise from Mn^{2+} as commonly believed, and that this emission perhaps maps the energy levels in the band tail states.

Chapter 4: Strong excitation energy dependent PL emission in a wide band gap aluminosilicate (feldspar): role of the Sub-conduction band tail states (Under review)

Chapter 4 is presented as a research article, which is at a near-submission stage. It further develops the model of orange-green emission in feldspar in Chapter 3. The phenomenon of excitation-energy-dependent emission (red edge effect) is well known from photoluminescence (PL) of polar solvents and carbon-based nanoparticles. However, to my knowledge, the red edge effect has never been reported from large crystalline materials. This chapter presents detailed investigations on the red-edge effect (discovered in chapter 3) in the orange-green emission in six different feldspar (alkali and plagioclase) samples. Based on low

[1] https://doi.org/10.1016/j.radmeas.2016.02.033, Radiation Measurements, 2016.

temperature photoluminescence investigations and time-resolved fluorescence and phosphorescence studies, it is concluded that this effect results from photo-ionisation of a deep lying defect and subsequent interaction of its higher electronic state with the sub-conduction band tail states. We confirm further the suggestion from Chapter 3 that the orange-green emission does not arise from Mn^{2+}; instead it may arise from surface related defects. These results are important because band tail states play an important role in charge transfer and in determining the thermal stability of the IR trap; an issue of immense importance for the use of feldspar in luminescence geochronology and thermochronometry. However, as yet there is no simple method to characterize band tails on a routine basis. The red edge effect shown here has the potential to be used as a simple, robust method to determine the width of the band tail states. This study may also have implications for understanding the red edge effect in quantum dots, where the mechanism behind the effect is a subject of intense debate.

Chapter 5: Dynamics of the deep-red photoluminescence emission in feldspar: role of the Fe^{3+} site dependence (Under review)

Chapter 5 is presented as a research article, which is at a near-submission stage. It further explores the origin and the dynamics of the deep-red emission in feldspar, briefly reported in Chapter 3. The deep red emission arises from Fe^{3+} substituting for Al^{3+} in the feldspar lattice. This emission has been previously used in thermoluminescence (red TL) and IRSL dosimetry (e.g. Zink and Visocekas, 1997; Fattahi & Stokes, 2003), and is considered not to suffer from anomalous fading. Despite its importance in feldspar-based dosimetry, the details of deep red emission are not very well known. The objective of this study is to further enrich the Fe^{3+} model in feldspar by addressing issues such as the site dependence of Fe^{3+} emission in complex samples, and understanding the dynamics of the forbidden $^4T_1 \rightarrow {}^6A_1$ radiative relaxation. We surveyed eleven different feldspar samples, and then used one of these samples (R56) for detailed site-selective spectroscopy and time-resolved photoluminescence measurements at cryogenic temperatures. The peak energy of the Fe^{3+} emission has been known to vary across feldspar samples, depending on the composition and structure; we demonstrate that this emission energy can vary dynamically, depending on the site selection,

even within a single sample. The observed excitation-energy dependent emission (red edge effect) may be used to discriminate Fe^{3+} sites, especially at the cryogenic temperatures; this behaviour potentially provides a powerful tool for characterising single crystals. We also show, contrary to expectation, that the radiative relaxation ($^4T_1 \rightarrow {}^6A_1$) in Fe^{3+} depends upon mode of excitation (resonant vs. non-resonant). We infer that the excited state of Fe^{3+} undergoes a slow energy-transfer during resonant excitation, possibly a spin-lattice interaction, a process that leads to a time delay in radiative relaxation. This study demonstrates yet another mechanism of red edge effect in feldspar (see chapter 4), conveying the richness of photonic processes in feldspar. This work leads to a better understanding of the interaction of Fe^{3+} with the feldspar lattice, and may have a potential application in 'quality' assessment of samples (single grains) for luminescence dating.

Chapter 6: Probing metastable Sm^{2+} and optically stimulated tunnelling emission in YPO_4: Ce, Sm. (Published[2])

Chapter 6 takes a detour to a lanthanide co-doped model dosimeter material YPO_4: Ce, Sm developed by the Delft group (e.g. Bos et al., 2008; Dorenbos et al., 2011). The purpose of this work was to understand the dose-dependent intra-defect luminescence (probing the metastable state), and sub-conduction band charge transfer from the electron to the hole-trapping center ($Sm^{2+} \rightarrow Ce^{4+}$). This system works as a model analogue for feldspar, which also has a sub-conduction band excited state and tunneling from the excited state of the electron trap to the hole center (Poolton et al., 2009; Jain and Ankjærgaard, 2011). This contribution has for the first time shown: a) direct high-resolution mapping of the excited states of the metastable Sm^{2+} electron trapping site using the defects internal relaxation mechanism, b) temperature-dependent lifetime of the metastable Sm^{2+}, and c) kinetics of the excited state tunneling recombination from Sm^{2+} to Ce^{4+} (Figure 1.3(a)).The results of this study gave inspiration for searching a Stoke's shifted dosimetric IRPL signal in feldspar.

[2] `http://dx.doi.org/10.1016/j.radmeas.2016.11.012`, Radiation Measurements, 2016, in press.

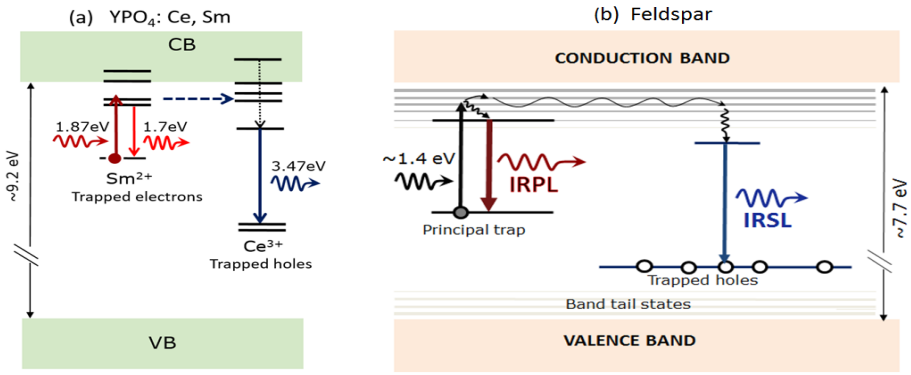

Figure 1.3: The luminescence process in (a) YPO_4: Ce, Sm - an analogous system to feldspar (b) Feldspar.

Chapter 7: Optical dating in a new light: A direct, non-destructive probe of trapped electrons (Accepted in : Scientific Reports - Nature)

Chapter 7 explores and introduces a new Stoke's shifted signal for optical dating for the first time, named InfraRed PhotoLuminescence (IRPL; Figure 1.3(b)). This signal is generated by the radiative relaxation of excited electrons within the IR dosimetric trap; thus unlike IRSL, the IRPL signal directly monitors the trapped electrons via defects internal relaxation, without relying on any electron-hole recombination. Low-temperature spectroscopy and time-resolved measurements are used to understand the mechanisms behind the IRPL generation. It is demonstrated that the signal can be read out non-destructively at cryogenic temperatures. Preliminary investigations are carried out to test the suitability of the IRPL signal for dating using single-aliquot additive-dose and single-aliquot regenerative (SAR) dose procedures. The signal appears to be non-fading as expected from theoretical considerations, and has a high dose response (kGy range). This signal opens a new, highly promising window in optical dating since the development of IRSL, and offers a powerful tool to examine the luminescence physics of feldspar as it, for the time, enables us to study the trapped electrons individually.

Chapter 8: Summary and Conclusion

This chapter provides a summary of the major results, contributions towards understanding luminescence mechanisms in feldspar and the expected impact of this research.

Bibliography

[1] Aitken, M. J. (1998). Introduction to optical dating: the dating of Quaternary sediments by the use of photon-stimulated luminescence. Clarendon Press.

[2] Aitken, M. J. (1994). Optical dating: a non-specialist review. Quaternary Science Reviews, 13(5-7), 503-508.

[3] Aitken, M. J. (1985). Thermoluminescence dating. Academic press.

[4] Anderson, P. W. (1958). Absence of diffusion in certain random lattices. Physical review, 109(5), 1492.

[5] Andersen, M. T., Jain, M., Tidemand-Lichtenberg, P. (2012). Red-IR stimulated luminescence in K-feldspar: Single or multiple trap origin? Journal of Applied Physics, 112(4), 043507.

[6] Ankjærgaard, C., & Jain, M. (2010). Optically stimulated phosphorescence in orthoclase feldspar over the millisecond to second time scale. Journal of Luminescence, 130(12), 2346-2355.

[7] Bailiff, I. K., & Poolton, N. R. J. (1991). Studies of charge transfer mechanisms in feldspars. International Journal of Radiation Applications and Instrumentation. Part D. Nuclear Tracks and Radiation Measurements, 18(1-2), 111-118.

[8] Banerjee, D., Blair, M., Lepper, K., & McKeever, S. W. S. (2002). Optically stimulated luminescence signals of polymineral fine grains in the JSC Mars-1 soil simulant sample. Radiation protection dosimetry, 101(1-4), 321-326.

[9] Baril, M. R., & Huntley, D. J. (2003). Infrared stimulated luminescence and phosphorescence spectra of irradiated feldspars. Journal of Physics: Condensed Matter, 15(46), 8029.

[10] Bos, A. J. J., Dorenbos, P., Bessière, A, Viana, B. (2008) Lanthanide energy levels in YPO4. Radiation Measurements 43, 222 – 226.

[11] Bøtter-Jensen, L., McKeever, S. W., & Wintle, A. G. (2003). Optically stimulated luminescence dosimetry. Elsevier.

[12] Buylaert, J. P., Jain, M., Murray, A. S., Thomsen, K. J., & Lapp, T. (2012). IR-RF dating of sand-sized K-feldspar extracts: a test of accuracy. Radiation Measurements, 47(9), 759-765.

[13] Buylaert, J. P., Murray, A. S., Vandenberghe, D., Vriend, M., & De Corte, F. (2008). Optical dating of Chinese loess using sand-sized quartz: establishing a time frame for Late Pleistocene climate changes in the western part of the Chinese Loess Plateau. Quaternary Geochronology, 3(1), 99-113.

[14] Buylaert, J. P., Murray, A. S., Thomsen, K. J., & Jain, M. (2009). Testing the potential of an elevated temperature IRSL signal from K-feldspar. Radiation Measurements, 44(5), 560-565.

[15] Buylaert, J. P., Jain, M., Murray, A. S., Thomsen, K. J., Thiel, C., & Sohbati, R. (2012). A robust feldspar luminescence dating method for Middle and Late Pleistocene sediments. Boreas, 41(3), 435-451.

[16] Clark, R. J., & Bailiff, I. K. (1998). Fast time-resolved luminescence emission spectroscopy in some feldspars. Radiation measurements, 29(5), 553-560.

[17] Clarke, M. L., & Rendell, H. M. (1997). Infra-red stimulated luminescence spectra of alkali feldspars. Radiation Measurements, 27(2), 221-236.

[18] Clark, R. J., & Sanderson, D. C. W. (1994). Photostimulated luminescence excitation spectroscopy of feldspars and micas. Radiation Measurements, 23(2-3), 641-646.

[19] Cunha, P. P., Almeida, N. A., Aubry, T., Martins, A. A., Murray, A. S., Buylaert, J.P., Sohbati, R., Raposo, L. & Rocha, L. (2012). Records of human occupation from Pleistocene river terrace and aeolian sediments in the Arneiro depression (Lower Tejo River, central eastern Portugal). Geomorphology, 165, 78-90.

[20] Dorenbos, P., Bos, A. J. J., Poolton, N. R. J. (2011) Electron transfer processes in double lanthanide activated YPO4, Optical Materials 33, 1019–1023

[21] Duller, G. A. T. (1996). Recent developments in luminescence dating of Quaternary sediments. Progress in Physical Geography, 20(2), 127-145.

[22] Duller, G. A. T. (1997). Behavioural studies of stimulated luminescence from feldspars. Radiation Measurements, 27(5), 663-694.

[23] Erfurt, G. (2003). Infrared luminescence of Pb^{+} centres in potassium-rich feldspars. Physica status solidi (a), 200(2), 429-438.

[24] Fattahi, M., & Walker, R. T. (2007). Luminescence dating of the last earthquake of the Sabzevar thrust fault, NE Iran. Quaternary Geochronology, 2(1), 284-289.

[25] Fattahi, M., & Stokes, S. (2003). Red luminescence from potassium feldspar for dating applications: a study of some properties relevant for dating. Radiation Measurements, 37(6), 647-660.

[26] Finch, A. A., & Klein, J. (1999). The causes and petrological significance of cathodoluminescence emissions from alkali feldspars. Contributions to Mineralogy and Petrology, 135(2-3), 234-243.

[27] Frouin, M., Huot, S., Kreutzer, S., Lahaye, C., Lamothe, M., Philippe, A., & Mercier, N. (2017). An improved radiofluorescence single-aliquot regenerative dose protocol for K-feldspars. Quaternary Geochronology, 38, 13-24.

[28] Gaft, M., Reisfeld, R., & Panczer, G. (2015). Modern luminescence spectroscopy of minerals and materials. Springer.

[29] Geake, J. E., Walker, G., Telfer, D. J., Mills, A. A. (1977). The Cause and Significance of Luminescence in Lunar Plagioclase. Philosophical Transactions of the Royal Society A: Mathematical, Physical and Engineering Sciences, 285, 403-405.

[30] Garcia-Guinea, J., Townsend, P. D., Sanchez-Munoz, L., & Rojo, J. M. (1999). Ultraviolet-blue ionic luminescence of alkali feldspars from bulk and interfaces. Physics and chemistry of minerals, 26(8), 658-667.

[31] Gorobets, B. S., Portnov, A. M., & Rogozhin, A. A. (1995). Luminescence spectroscopy of the earth. Radiation measurements, 24(4), 485-491.

[32] Gould, S. J. (1987). Time's arrow, time's cycle: Myth and metaphor in the discovery of geological time (Vol. 2). Harvard University Press.

[33] Guralnik, B., Jain, M., Herman, F., Ankjærgaard, C., Murray, A. S., Valla, P. G., ... & Kook, M. (2015). OSL-thermochronometry of feldspar from the KTB borehole, Germany. Earth and Planetary Science Letters, 423, 232-243.

[34] Henshilwood, C. S., d'Errico, F., Yates, R., Jacobs, Z., Tribolo, C., Duller, G.A., Mercier, N., Sealy, J.C., Valladas, H., Watts, I. & Wintle, A. G. (2002). Emergence of modern human behavior: Middle Stone Age engravings from South Africa. Science, 295(5558), 1278-1280.

[35] Herman, F., Seward, D., Valla, P. G., Carter, A., Kohn, B., Willett, S. D., & Ehlers, T. A. (2013). Worldwide acceleration of mountain erosion under a cooling climate. Nature, 504(7480), 423-426.

[36] Huntley, D. J. (2006). An explanation of the power-law decay of luminescence. Journal of Physics: Condensed Matter, 18(4), 1359.

[37] Huntley, D. J., & Lamothe, M. (2001). Ubiquity of anomalous fading in K-feldspars and the measurement and correction for it in optical dating. Canadian Journal of Earth Sciences, 38(7), 1093-1106.

[38] Huntley, D. J., Godfrey-Smith, D. I., & Haskell, E. H. (1991). Light-induced emission spectra from some quartz and feldspars. International Journal of Radiation Applications and Instrumentation. Part D. Nuclear Tracks and Radiation Measurements, 18(1-2), 127-131.

[39] Huntley, D. J., & Lian, O. B. (2006). Some observations on tunnelling of trapped electrons in feldspars and their implications for optical dating. Quaternary Science Reviews, 25(19), 2503-2512.

[40] Huntley, D. J., Godfrey-Smith, D. I., & Thewalt, M. L. (1985). Optical dating of sediments. Nature, 313(5998), 105-107.

[41] Hütt, G., Jaek, I., & Tchonka, J. (1988). Optical dating: K-feldspars optical response stimulation spectra. Quaternary Science Reviews, 7(3-4), 381-385.

[42] Itoh, C., Tanimura, K., Itoh, N., & Itoh, M. (1989). Threshold energy for photogeneration of self-trapped excitons in Si O 2. Physical Review B, 39(15), 11183.

[43] Jain, M., Andersen, C. E., Bøtter-Jensen, L., Murray, A. S., Haack, H., & Bridges, J. C. (2006). Luminescence dating on Mars: OSL characteristics of Martian analogue materials and GCR dosimetry. Radiation Measurements, 41(7), 755-761.

[44] Jain, M., & Ankjærgaard, C. (2011). Towards a non-fading signal in feldspar: insight into charge transport and tunnelling from time-resolved optically stimulated luminescence. Radiation Measurements, 46(3), 292-309.

[45] Jain, M., Guralnik, B., & Andersen, M. T. (2012). Stimulated luminescence emission from localized recombination in randomly distributed defects. Journal of Physics: Condensed Matter, 24(38), 385402.

[46] Jain, M., Sohbati, R., Guralnik, B., Murray, A. S., Kook, M., Lapp, T., Prasad, A.K., Thomsen, K.J. & Buylaert, J. P. (2015a). Kinetics of infrared stimulated luminescence from feldspars. Radiation Measurements, 81, 242-250.

[47] Jain, M., Buylaert, J. P., Thomsen, K. J., & Murray, A. S. (2015b). Further investigations on 'non-fading' in K-Feldspar. Quaternary International, 362, 3-7.

[48] King, G. E., Guralnik, B., Valla, P. G., & Herman, F. (2016). Trapped-charge thermochronometry and thermometry: A status review. Chemical Geology, 446, 3-17.

[49] Kitis, G., & Pagonis, V. (2013). Analytical solutions for stimulated luminescence emission from tunneling recombination in random distributions of defects. Journal of Luminescence, 137, 109-115.

[50] Kalchgruber, R., Blair, M. W., McKeever, S. W., Benton, E. R., & Reust, D. K. (2007). Progress towards robotic in-situ dating of martian sediments using optically stimulated luminescence. Planetary and Space Science, 55(14), 2203-2217.

[51] Kars, R. H., Wallinga, J., & Cohen, K. M. (2008). A new approach towards anomalous fading correction for feldspar IRSL dating—tests on samples in field saturation. Radiation Measurements, 43(2), 786-790.

[52] Kars, R. H., Poolton, N. R., Jain, M., Ankjærgaard, C., Dorenbos, P., & Wallinga, J. (2013). On the trap depth of the IR-sensitive trap in Na-and K-feldspar. Radiation Measurements, 59, 103-113.

[53] Krbetschek, M. R., Rieser, U., & Stolz, W. (1996). Optical dating: some luminescence properties of natural feldspars. Radiation Protection Dosimetry, 66(1-4), 407-412.

[54] Krbetschek, M. R., Götze, J., Dietrich, A., & Trautmann, T. (1997). Spectral information from minerals relevant for luminescence dating. Radiation Measurements, 27(5), 695-748.

[55] Krbetschek, M. R., & Rieser, U. (1995). Luminescence spectra of alkalifeldspars and plagioclases. Radiation Measurements, 24(4), 473-477.

[56] Lepper, K., & McKeever, S. W. (2000). Characterization of fundamental luminescence properties of the Mars soil simulant JSC Mars-1 and their relevance to absolute dating of Martian eolian sediments. Icarus, 144(2), 295-301.

[57] Liritzis, I., Singhvi, A. K., & James, K. (2013). Luminescence dating in archaeology, anthropology, and geoarchaeology: an overview. Heidelberg, Germany: Springer.

[58] Li, S. H., & Tso, M. Y. W. (1997). Lifetime determination of OSL signals from potassium feldspar. Radiation Measurements, 27(2), 119-121.

[59] Li, B., & Li, S. H. (2011a). Luminescence dating of K-feldspar from sediments: a protocol without anomalous fading correction. Quaternary Geochronology, 6(5), 468-479.

[60] Li, B., & Li, S. H. (2011b). Thermal stability of infrared stimulated luminescence of sedimentary K-feldspar. Radiation Measurements, 46(1), 29-36.

[61] Li, B., & Li, S. H. (2013). The effect of band-tail states on the thermal stability of the infrared stimulated luminescence from K-feldspar. Journal of Luminescence, 136, 5-10.

[62] Malins, A. E. R., Poolton, N. R. J., Quinn, F. M., Johnsen, O., & Denby, P. M. (2004). Luminescence excitation characteristics of Ca, Na and K-aluminosilicates (feldspars) in the stimulation range 5–40 eV: determination of the band-gap energies. Journal of Physics D: Applied Physics, 37(10), 1439.

[63] McKeever, S. W., Kalchgruber, R., Blair, M. W., & Deo, S. (2006). Development of methods for in situ dating of martian sediments. Radiation Measurements, 41(7), 750-754.

[64] Morthekai, P., Chauhan, P. R., Jain, M., Shukla, A. D., Rajapara, H. M., Krishnan, K., Sant, D.A., Patnaik, R., Reddy, D.V. & Singhvi, A. K. (2015). Thermally re-distributed IRSL (RD-IRSL): A new possibility of dating sediments near B/M boundary. Quaternary Geochronology, 30, 154-160.

[65] Morthekai, P., Thomas, J., Pandian, M. S., Balaram, V., & Singhvi, A. K. (2012). Variable range hopping mechanism in band-tail states of feldspars: A time-resolved IRSL study. Radiation Measurements, 47(9), 857-863.

[66] Mott, N. F. (1969). Conduction in non-crystalline materials: III. Localized states in a pseudogap and near extremities of conduction and valence bands. Philosophical Magazine, 19(160), 835-852.

[67] Murray, A. S., Buylaert, J. P., Thomsen, K. J., & Jain, M. (2009). The effect of preheating on the IRSL signal from feldspar. Radiation Measurements, 44(5), 554-559.

[68] Pagonis, V., Polymeris, G., & Kitis, G. (2015). On the effect of optical and isothermal treatments on luminescence signals from feldspars. Radiation Measurements, 82, 93-101.

[69] Pagonis, V., Ankjærgaard, C., Jain, M., & Chithambo, M. L. (2016). Quantitative analysis of time-resolved infrared stimulated luminescence in feldspars. Physica B: Condensed Matter, 497, 78-85.

[70] Poolton, N. R. J., Bøtter-Jensen, L., & Johnsen, O. (1996). On the relationship between luminescence excitation spectra and feldspar mineralogy. Radiation measurements, 26(1), 93-101.

[71] Poolton, N. R. J., Mauz, B., Lang, A., Jain, M., & Malins, A. E. R. (2006). Optical excitation processes in the near band-edge region of KAlSi3O8 and NaAlSi3O8 feldspar. Radiation measurements, 41(5), 542-548.

[72] Poolton, N. R. J., Kars, R. H., Wallinga, J., & Bos, A. J. J. (2009). Direct evidence for the participation of band-tails and excited-state tunnelling in the luminescence of irradiated feldspars. Journal of Physics: Condensed Matter, 21(48), 485-505.

[73] Poolton, N. R. J., Wallinga, J., Murray, A. S., Bulur, E., & Bøtter-Jensen, L. (2002a). Electrons in feldspar I: on the wavefunction of electrons trapped at simple lattice defects. Physics and Chemistry of Minerals, 29(3), 210-216.

[74] Poolton, N. R. J., Ozanyan, K. B., Wallinga, J., Murray, A. S., & Bøtter-Jensen, L. (2002b). Electrons in feldspar II: a consideration of the influence of conduction band-tail states on luminescence processes. Physics and Chemistry of Minerals, 29(3), 217-225.

[75] Prescott, J. R., Robertson, G. B., Shoemaker, C., Shoemaker, E. M., & Wynn, J. (2004). Luminescence dating of the Wabar meteorite craters, Saudi Arabia. Journal of Geophysical Research: Planets, 109(E1).

[76] Rhodes, E. J. (2011). Optically stimulated luminescence dating of sediments over the past 200,000 years. Annual Review of Earth and Planetary Sciences, 39, 461-488.

[77] Rittenour, T. M. (2008). Luminescence dating of fluvial deposits: applications to geomorphic, palaeoseismic and archaeological research. Boreas, 37(4), 613-635.

[78] Rieser, U., Hütt, G., Krbetschek, M. R., & Stolz, W. (1997). Feldspar IRSL emission spectra at high and low temperatures. Radiation Measurements, 27(2), 273-278.

[79] Roberts, R. G., & Lian, O. B. (2015). Dating techniques: Illuminating the past. Nature, 520(7548), 438-439.

[80] Sanderson, D. C. W., & Clark, R. J. (1994). Pulsed photostimulated luminescence of alkali feldspars. Radiation Measurements, 23(2-3), 633-639.

[81] Singhvi, A. K., & Porat, N. (2008). Impact of luminescence dating on geomorphological and palaeoclimate research in drylands. Boreas, 37(4), 536-558.

[82] Spooner, N. A. (1994). The anomalous fading of infrared-stimulated luminescence from feldspars. Radiation Measurements, 23(2-3), 625-632.

[83] Sohbati, R. (2015). Luminescence, rock surfaces. In Encyclopedia of Scientific Dating Methods (pp. 485-488). Springer Netherlands.

[84] Sritrakool, W., Sa-Yakanit, V., & Glyde, H. R. (1986). Band tails in disordered systems. Physical Review B, 33(2), 1199.

[85] Telfer, D. J., & Walker, G. (1975). Optical detection of Fe^{3+} in lunar plagioclase. Nature, 258(5537), 694-695.

[86] Telfer, D. J., & Walker, G. (1978). Ligand field bands of Mn^{3+} + and Fe^{3+} luminescence centres and their site occupancy in plagioclase feldspars. Modern Geology, 6, 199-210.

[87] Thiel, C., Buylaert, J. P., Murray, A., Terhorst, B., Hofer, I., Tsukamoto, S., & Frechen, M. (2011). Luminescence dating of the Stratzing loess profile (Austria)–Testing the potential of an elevated temperature post-IR IRSL protocol. Quaternary International, 234(1), 23-31.

[88] Thomsen, K. J., Murray, A. S., Jain, M., & Bøtter-Jensen, L. (2008). Laboratory fading rates of various luminescence signals from feldspar-rich sediment extracts. Radiation measurements, 43(9), 1474-1486.

[89] Thomsen, K. J., Murray, A. S., & Jain, M. (2011). Stability of IRSL signals from sedimentary K-feldspar samples. Geochronometria, 38(1), 1-13.

[90] Trautmann, T., Dietrich, A., Stolz, W., & Krbetschek, M. R. (1999a). Radioluminescence dating: a new tool for Quaternary geology and archaeology. Naturwissenschaften, 86(9), 441-444.

[91] Trautmann, T., Krbetschek, M. R., Dietrich, A., & Stolz, W. (1999). Feldspar radioluminescence: a new dating method and its physical background. Journal of Luminescence, 85(1), 45-58.

[92] Tsukamoto, S., Denby, P. M., Murray, A. S., & Bøtter-Jensen, L. (2006). Time-resolved luminescence from feldspars: new insight into fading. Radiation Measurements, 41(7), 790-795.

[93] Visocekas, R. (1985). Tunnelling radiative recombination in labradorite: its association with anomalous fading of thermoluminescence. Nuclear Tracks and Radiation Measurements (1982), 10(4-6), 521-529.

[94] Visocekas, R. (1979). Miscellaneous Aspects of Artificial Tl of Calcite: Emission Spectra, Athermal Detrapping and Anomalous Fading in Séminaire de recherches consacrés à la datation par thermoluminescence, Oxford, 1978. Pact. Revue du Groupe Européen d'Etudes pour les Techniques Physiques, Chimiques et Mathématiques Appliquées à l'Archéologie Rixensart, (3), 258-265.

[95] Wallinga, J. (2002). Optically stimulated luminescence dating of fluvial deposits: a review. Boreas, 31(4), 303-322.

[96] White, W. B., Matsumara, M., Linnehan, D. G., Furukawa, T., Chandrasekhar, B. K.(1986). Absorption and luminescence of Fe^{3+} in single-crystal orthoclase. Am. Mineral. 71 1415–19.

[97] Wintle, A. G. (1994). Infrared-stimulated luminescence dating of sediments. Radiation Measurements, 23(2-3), 607-612.Wintle, A. G. (2008). Luminescence dating: where it has been and where it is going. Boreas, 37(4), 471-482.

[98] Wintle, A. G. (2008). Fifty years of luminescence dating. Archaeometry, 50(2), 276-312.

[99] Wintle, A. G. (1973). Anomalous fading of thermo-luminescence in mineral samples. Nature, 245(5421), 143-144.

[100] Zink, A. J. C., & Visocekas, R. (1997). Datability of sanidine feldspars using the near-infrared TL emission. Radiation Measurements, 27(2), 251-261.

Chapter 2

Instrumentation and Samples

Luminescence is a powerful tool to study defects in wide band-gap materials. It provides insights into the participating energy levels, defect-host interactions, and charge/energy transfer processes. However, the key to a successful characterization is availability of a state-of-the-art instrumentation. In particular, it is necessary to have a sensitive, high resolution, multi-probe measurement system to gain comprehensive understanding of the luminescence processes.

The main experimental work during my Ph.D. research was carried out using two important luminescence measurement facilities at DTU Nutech, viz., Risø station for CryOgenic LUminescence Research (COLUR), and a high sensitivity spectrometer attached to the Risø TL/OSL reader. These facilities were developed during my Ph.D. I participated in the commissioning and testing of COLUR, and used it actively to understand luminescence processes in natural and artificial dosimeter systems such as feldspar and YPO_4: Ce, Sm. I also worked on the optical interface design of the Risø Spectrometer using a Monte-Carlo optical simulation program called Zemax. This modelling helped to optimize the coupling of the optical fiber to the sample. I mainly used the Risø spectrometer to perform beta dose dependent spectral investigations.

The two experimental facilities are described below.

2.1 Risø station for CryOgenic LUminescence Research (COLUR)

COLUR was developed for studying luminescence properties of wide bandgap dosimetric materials with focus on low temperature excitation and emission spectroscopy, and luminescence decay measurements.

COLUR consists of a Horiba Spectrofluorometer (Fluorolog–3) whose sample chamber was modified to include cryogenic sample cooling (7-295 K), and additional excitation and detection attachments to do multi-probe experiments. These modifications were done at DTU Nutech in collaboration with Dr. Nigel Poolton in the spring 2015. The following sections describe the COLUR set up- a brief summary of the Fluorolog-3 (Section 2.1.1) and the modified sample chamber (Section 2.1.2).

2.1.1 FluoroLog-3

The Horiba Fluorolog-3 spectrofluorometer is a modular system which offers flexibility to add a range of accessories as per the user's requirements. In general, this spectrofluorometer is used for steady state and time-resolved luminescence measurements of samples (e.g. solid, powder, liquid, thin films etc.) in the 200 nm to 1050 nm spectral range. Figure 2.1 shows a picture of Fluorolog-3 at DTU Nutech before modification. Broadly, it consists of two broadband excitation sources (a continuous wave and a pulsed Xe lamp), excitation monochromator, a PMT detector coupled to an emission monochromator, and a cooled CCD detector coupled to a spectrograph. Various pulsed laser/LED sources as well as the pulsed Xe lamp can be used in conjunction with the PMT detector to do wavelength resolved luminescence decay measurements on nanosecond to millisecond time scales, respectively.The different components of this system are described below:

1. Excitation source: It consists of dual lamp housing which contains a continuous wave (CW) 450W, Xenon source and a Xenon flash tube. A swing mirror selects either the CW or the pulsed sources.

2. Excitation monochromator: This module is equipped with a Czerny-Turner double grating spectrometer (Shafer et al., 1964) with motorized entrance and exit slit. It has ruled blazed gratings with 1200 lines/mm(l/mm) with a 330 nm blaze wavelength. The advantage of a double grating system is that it provide a high stray light rejection, a good spectral resolution, and a high light throughput.

3. Emission spectrometer: It is also a Czerny-Turner single grating spectrometer with motorized entrance and exit slit (like in the excitation spectrometer) but with the 1200 l/mm grating at 500 nm blaze wavelength.

4. Detection system (PMT): The standard Hamamatsu R-928P PMT detector is coupled to the emission monochromator for high sensitivity photon counting. The detection can be monitored from 200-1000 nm. However, spectral correction (provided by Horiba) is only available in the range of 290– 850 nm. Outside this range there are huge, and thus unreliable, corrections because of the detector's low quantum efficiency.

5. Imaging spectrometer: It consists of iHR320 spectrograph (f/4.1) with a kinematic turret containing 3 gratings (i) 300 lines/mm with blaze wavelength at 500 nm, (ii) 1200 lines/mm with blaze wavelength at 500 nm and (iii) 1200 lines/mm with blaze wavelength at 750 nm. The detector attached with this spectrometer is a liquid-nitrogen-cooled CCD chip (Symphony II). This system is more sensitive in the red and near IR range compared to the PMT detector.

6. Phosphorescence attachment: This uses the pulsed Xe lamp source for excitation and the PMT system for detection, in combination with a multi-channel analyser. Time resolved measurements can be done on the microsecond to millisecond time scale.

7. Time-Correlated Single Photon Counting (TCSPC) attachment: The TCSPC attachment is based on photon arrival time stamping with respect to an excitation light pulse. It is used to measure fluorescence decay on hundreds of picosecond to nanosecond time scales. The TCSPC attachment is based on the use of the standard R928 PMT detector: It includes a single photon counting controller (FluoroHub), a

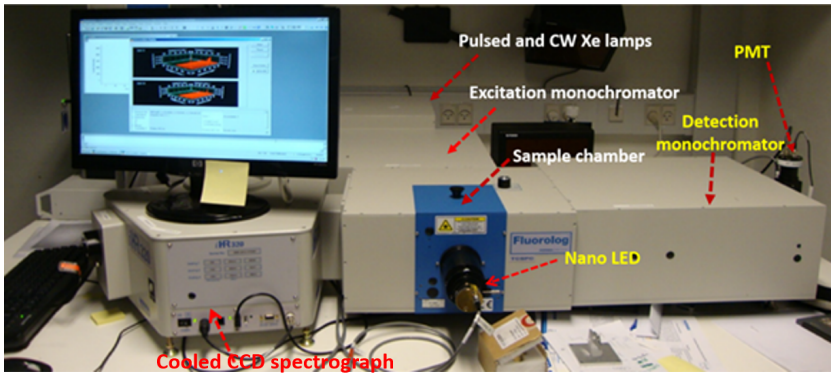

Figure 2.1: A picture of Horiba Fluorolog-3 spectrofluorometer at DTU Nutech.

data acquisition system (DataStation Hub) and various pulsed excitation sources (e.g., NanoLED and spectral LED's). I used nanoLED's with central wavelengths of 374 nm and 824 nm with pulse width of $\sim$ 1.1 ns and $<$ 200 ps, respectively, and a spectral LED of wavelength 561 nm (FWHM 21 nm).

8.Software: A Windows based FluorEssence v3.5 provides control of all the hardware and data-acquisition. The Origin 8 software package is integrated for the data analysis. DataStation and DAS6 softwares were used for acquiring and analyzing TCSPC data, respectively.

2.1.2 Modified sample chamber with multi-excitation and detection facilities

Figure 2.2(a) shows the Fluorolog-3 modified with the new sample chamber. It includes a low temperature facility with multiple excitation and detection options. The right side shows the close view of the new sample chamber seen from the top. Figure 2.2(b) shows the schematic of the configuration of the new sample chamber; it is coupled with the existing excitation and detection axes of the Fluorolog-3, and includes additional attachments such as an X-ray tube, PMT and fiber coupled lasers.

The sample chamber can be evacuated down to 10^{-5} mbar using a turbo pump. The sample is in thermal contact with a cold finger whose temperature can be varied from 295 K to 7 K. Cooling is achieved using a closed loop helium flow cryostat. The excitation sources such as X-ray, lasers, NanoLEDs and PMT are introduced from the top shown in Figure

2.2(b). The modified sample chamber sits on two rails and can be slided in and out of the Fluorolog-3.

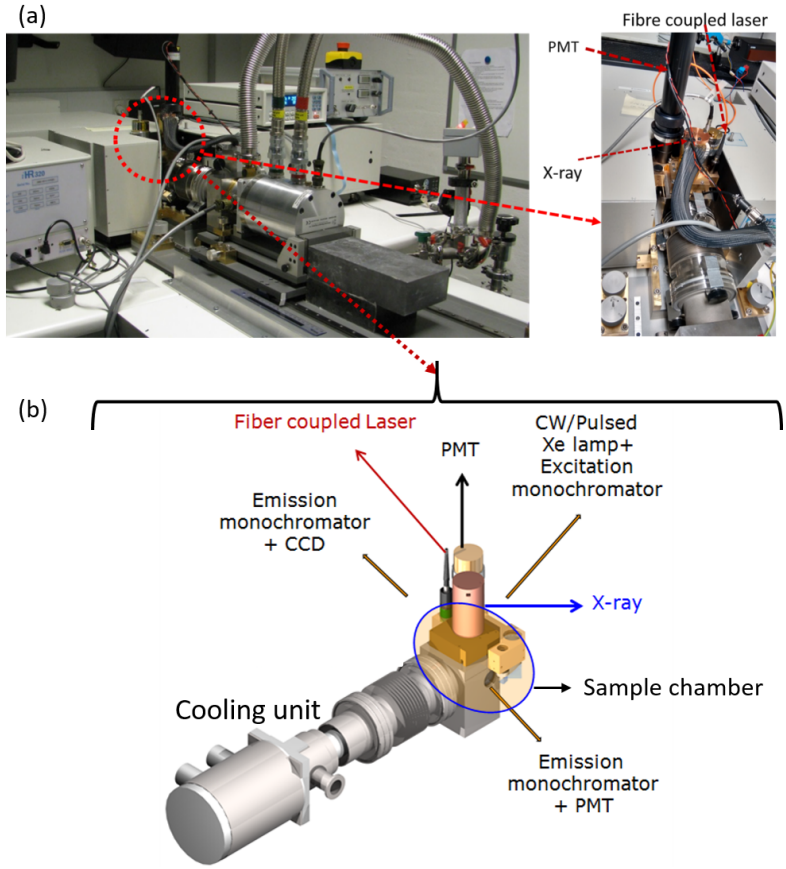

Figure 2.2: (a) Risø station for CryOgenic LUminescence Research (COLUR) (b) A schematic of the new sample chamber(modified from Risø internal report).

Some important aspects of the new modifications are described below:

1. Temperature control: The compact closed cycle cryostat achieves cooling via continuous compression/expansion cycles of a small volume of recycling helium gas. The measured cooling temperature with time is presented in the Figure 2.3; it takes about 90 minutes to cool from 295 K to 7 K. The proportional integral-derivative (PID) temperature control is provided through a Lakeshore (model 335) control unit. The sample

grains/powder can be directly mounted on a copper-based sample holder (a cold finger) with the help of carbon tape.

2. X-ray irradiation: A miniature Moxtek X-ray source of 40 kV anode voltage, and 95.7 mA anode current is used. The chamber and the tube are shielded to avoid radiation leakage. A special interlock was developed such that the X-ray tube can only operate under low pressure (chamber pressure of ∼10-4 mbar); this is to ensure that it is not possible to turn on the X-rays when it is not connected to the chamber and when the chamber is not completely closed. This attachment offers the possibility to irradiate the samples for subsequent OSL or PL measurements. It also enables measurement of X-ray excited luminescence (XEOL) spectra from a sample.

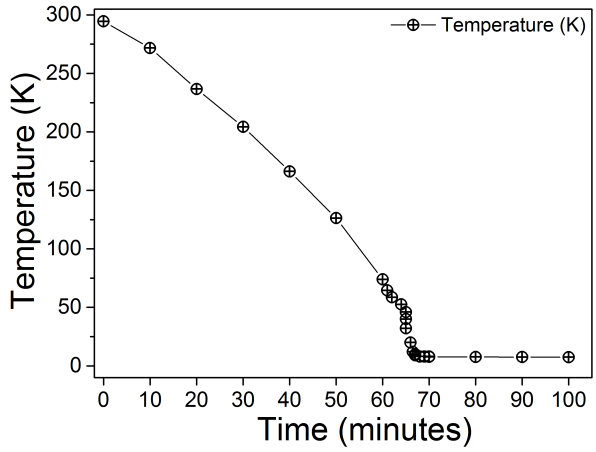

Figure 2.3: : Characteristics of the closed loop He cooling in COLUR

3. External PMT/or NanoLED port: This port can be used either for an external PMT or for the Horiba NanoLEDs for the TCSPC measurements. We used a bialkali EMI 9235QA PMT for integrated wavelength measurements using a detection filter. The external PMT attachment with cryogenic unit can be operated in parallel with the Fluorolog spectrometer allowing possibilities of dual detection. For example, one can measure the emission spectrum of an irradiated feldspar using emission spectrometer, while simultaneously measuring the OSL decay curve using a BG39 filter in front of the PMT.

4. External laser source: It is possible to connect any external light source through the SMA fiber optics to the sample tip. I used five different lasers depending on the experiment. These lasers were with the central wavelengths: 405, 532, 657, 842 and 885nm, operating at 200, 300, 40, 90 and 500 mW optical power, respectively. Of these, the lasers at 657 nm and 842 nm can also be operated in pulsed mode for the luminescence decay measurements using the TCSPC attachment of the Flourolog-3. Some examples of the laser characteristics are shown in Figure 2.4. Figure 2.4(a) shows the emission spectrum of the 657 nm laser, whereas Figure 2.4(b) shows its measured pulse decay time. The switch off time was evaluated to be 2.4 ns between 90% to 10% of the maximum optical power. Figure 2.4(c) shows the laser spectrum of 842 nm. This laser has a multimode emission pattern (other emission at 844 nm) at the nominal power 90 mW, but the spectrum presented here was measured at 50 mW power. Figure 2.4(d) shows the laser switch off time (18 ns) between 90% to 10% emission power. These lasers can be modulated up to 155 MHz.

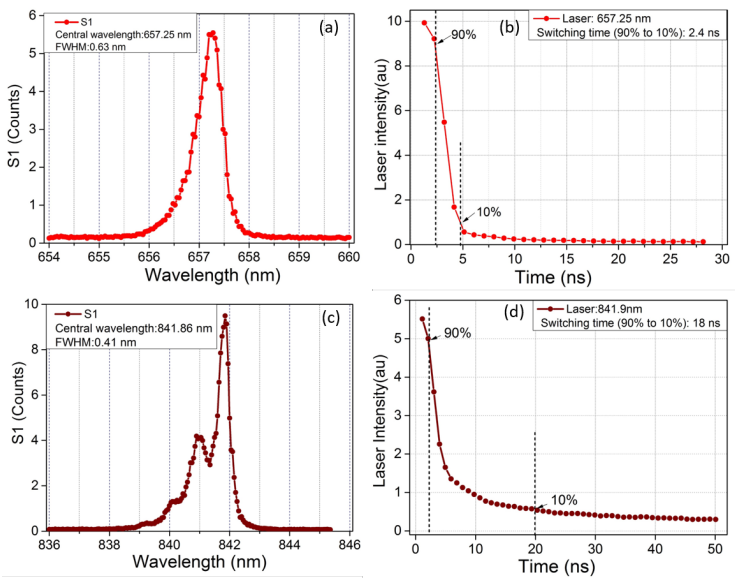

Figure 2.4: (a) 657 nm laser spectrum, (b) evaluation of switch off time of 657 nm laser, (c) 842 nm laser spectrum, (d) evaluation of switch off time of 842 nm laser.

2.2 Alignment for multi-excitation and multi-emission detection

There are several optical directions involved in the modified sample chamber Figure 2.2(b). For reliable and high sensitivity measurements, these axes need to be aligned appropriately to achieve high excitation power and luminescence throughput. We can define the Xe light direction as the X-axis, the X-ray irradiation direction as the Z-axis, and the PMT and the CCD detection sides of Fluorolog-3 as the +Y and -Y-axes, respectively. The X-ray and the external laser/PMT ports are fixed with respect to the sample chamber. The system is designed such that the Xe lamp, PMT/CCD detection and X-ray irradiation coincide at the sample position; however, the sample chamber has to be adjusted in the XYZ directions to achieve this alignment.

Figure 2.5(a) shows the excitation and emission alignment in the X-Y plane. A piece of white paper (analogue of sample) with concentric circles is mounted on the sample holder tip. First, the red light is selected from the Xe lamp using the excitation monochromator; thus, the footprint of the Xe light can be seen on the white paper. Then, the PMT detector of Fluorolog-3 is dismounted and a white light source is shined through this port (the same was done using the CCD port of the imaging spectrometer, but the picture is not shown here). The emission monochromator in front of the PMT is adjusted to select the green light from the white light spectrum, and this green light makes a second footprint on the white paper. Using the X-Y adjustment knobs, the two footprints are matched together (Figure 2.5(a)). The laser port uses a fiber SMA connector from the top of the chamber; the beam can be steered with a 45° mirror (up/down and rotation allows X-Y-Z adjustment with respect to the sample chamber) to match the footprints of the detection and excitation described above. Figure 2.5(b) shows the 532 nm laser spot after proper alignment.

The footprint of the X-ray is always at the cold finger and can be measured using the Gafchromic (GAF) film. The colour of the film changes after X- ray irradiation (Figure 2.5(c)). Figure 2.5(d) shows the sample holder with YPO_4: Ce, Sm using the red laser and Figure 2.5(e) shows the R28 (K-Feldspar) sample using a green laser; these demonstrate a perfect alignment of the lasers at the sample position.

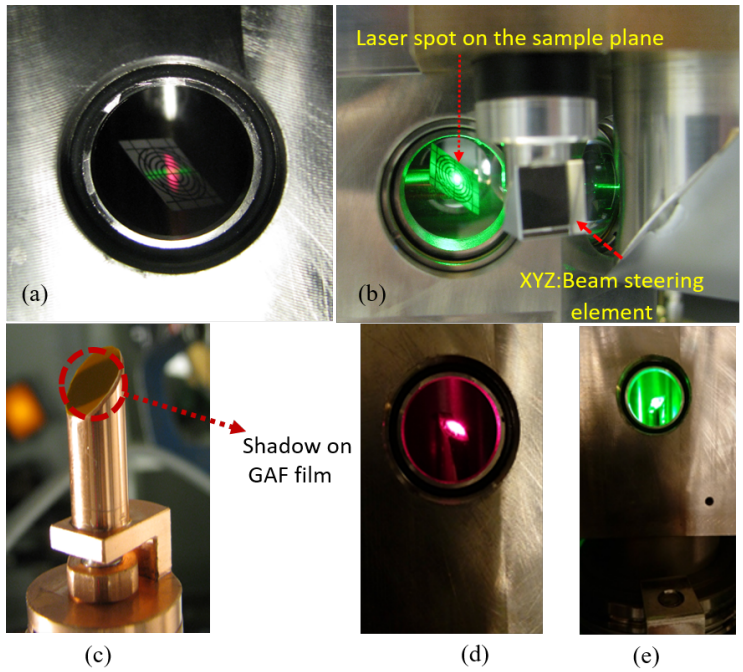

Figure 2.5: (a) Optical alignment of the sample in the X-Y plane (excitation and detection side of emission). (b) 532 nm laser beam at the same spot. (c) GAF film mounted on the sample holder to confirm the X-ray alignment in the Z direction. The coloration on the GAF film occurs in response to the X-ray irradiation. (d) YPO_4: Ce, Sm sample mounted on the cold finger and illuminated under 657 nm laser irradiation. (e) R28 (K-Feldspar) sample mounted on cold finger and illuminated under 532 nm laser.

Table 2.1: A summary of experiments and some representative data measured using COLUR

No	Experiments at room temperature or cryogenic temperatures	Materials	Representative figure
1.	Excitation spectrum	Feldspar YPO_4:Ce,Sm	Chapter 3: Figure 3.2, Chapter 5: Figure 5.1,5.2 , Chapter 6:Figure 5.1(b) etc.
2.	Emission spectrum		Chapter 3: Figure 3.2,3.4,Chapter 4: Figure: 4.2-4.8,Chapter 5: Figure 5.1-5.3,Chapter 6: Figure 6.1,6.2, Chapter 7: Figure 7.1-7.3 etc
3.	XEOL		Chapter 3: Figure 3.1
4.	Fluorescence Lifetime		Chapter 4:Figure 4.9, Chapter 6:Figure 6.1,6.2, Chapter 7: Figure 7.3(f) etc.
5.	Phosphorescence lifetime		Chapter 3: Figure 3.2,3.5; Chapter:4,Figure 4.10, Chapter 5: Figure 5.8 etc.
6.	Phosphorescence emission		Chapter 3: Figure 3.3
7.	IRSL excitation spectrum		Chapter 4: Figure 4.1, Chapter 7: Figure 7.2(a), 7.3(a)etc.
8.	Dose dependent IRPL		Chapter 7: Figure 7.2(b),7.3(d) etc.
9.	3D excitation and emission		Chapter 7:Figure 7.3(b)
10.	Tunnelling OSL using external PMT	YPO_4:Ce,Sm	Chapter 6: Figure 6.3(a)

2.3 Risø TL/OSL spectrometer

The Risø TL/OSL reader is well known in the optical dating community and the facilities are documented in various scientific articles (Bøtter-Jensen et al., 2010; Lapp et al., 2009, 2012). Figure 2.6(a):Left; shows the Risø TL/OSL reader with the spectrometer attachment (also see Prasad et al., 2016). I used the Risø spectrometer to measure the radioluminescence (RL) spectra, IRSL emission spectra and the IRPL emission spectra as a function of beta dose from different feldspar samples.

The set-up uses an Andor Shamrock SR193 Czerny-Turner spectrograph Figure 2.6(a):Right;for wavelength dispersion. We used a 150 or 300 lines/mm grating, which offers the spectral detection window of $\sim$ 440 or 217 nm, respectively. The slit width of the spectrometer can be adjusted for the maximum signal intensity but at the cost of spectral resolution ($\sim$18 nm resolution for fully opened slit at 405 nm). The spectrometer is attached to a thermoelectrically cooled EMCCD camera (Andor iXon Ultra 888) for highest possible signal-to-noise ratio at the detection stage. It has 1024 $\times$ 1024 sensor format and 13 μm pixel size. A custom-made fused silica based fiber bundle consisting of 114 fibers is used as a light guide from the sample to the spectrograph. Each fiber has an internal diameter of 200 μm. The fiber bundle is arranged such that it has a circular form with a diameter of $\sim$ 3.1 mm and a numerical aperture of 0.22 at the sample side, while the output (spectrograph side) consists of two rows of 57 fibers corresponding to a rectangular form (15.9 $\times$ 0.4 mm) (see Figure 2.6(d)). These configurations are chosen to optimize the light collection and delivery with respect to the sample (circular form) and the spectrograph slit (rectangular form). The sample handling is done in the same way as in the conventional Risø TL-OSL reader.

The optical interface between the Risø TL/OSL reader and light guiding fiber optics was an important element. I worked on the simulation of the optical interface using Zemax. The coupling to the fiber was optimized with respect to efficiency (Pfiber/Psample) where Pfiber is the power entering the fiber and Psample is the power emitted from the sample over the entire spectral range of interest $\sim$ 330-1000 nm. The optical interface was optimized for 8 mm sample diameter, which is realistic for most of the measurements using a Risø sample cup with diameter of around 10 mm (see Figure 2.6(b) and (c)).

In order to use the spectrometer it is important to both calibrate the measured spectra for wavelength, as well as the intensity (efficiency).

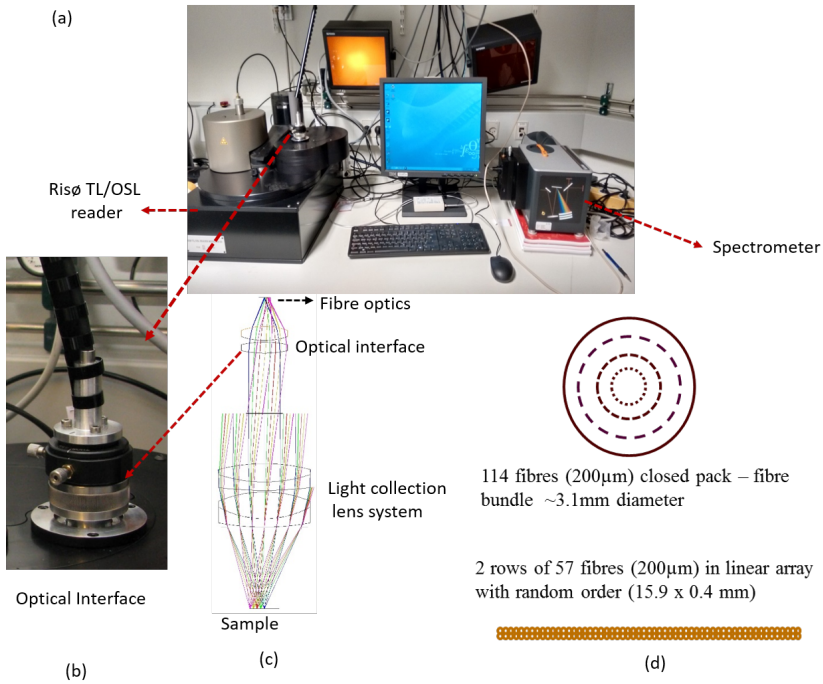

Figure 2.6: (a) Risø TL/OSL reader with Andor spectrometer attached (b) Optical interface (c) Ray diagram of luminescence collection from the sample to the fiber optics using different lenses (d) Geometrical configuration of the fiber bundle on the sample and the spectrometer side.

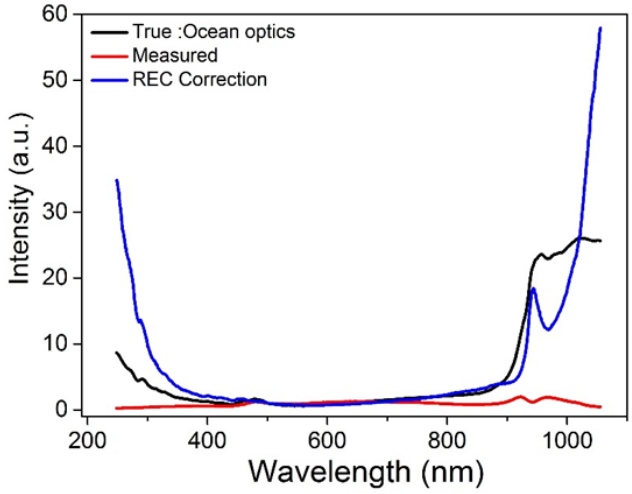

Figure 2.7: Relative efficiency curve for Risø TL/OSL spectrometer and grating 300 l/mm

Wavelength calibration was carried out using the Ocean Optics Mercury Argon Calibration source. We used 435.8 nm and 763.5 nm peaks after focussing the dispersed light spectrum on the CCD chip. Since the spectrometer does not have the same efficiency over the entire spectral range, it is also important to correct for this effect after the wavelength calibration. The overall efficiency of the system depends on the lenses, the fibres, grating, mirrors, and quantum efficiency of the CCD, all of which are wavelength dependent. In order to make an efficiency correction we illuminated the sample plate with a light source with a known and stable spectral output. First, we measured the spectra from the mercury-tungsten lamp using 300 l/nm grating, and then it was divided by the known spectra of mercury-tungsten spectrum provided by ocean optics to get the efficiency curve (Relative efficiency correction(REC); Figure 2.7). This ratio is later used for correcting the unknown spectra measured from the samples. It can be seen that the reliable correction using this system range is from about 300 to 900 nm; outside this range, the correction factors are very large (Figure 2.7, Blue curve).

I mainly used the Risø spectrometer for measuring beta dose dependent IRSL and IRPL (infra-red photoluminescence) spectra. The spectra were measured using the 885nm (1.4 eV) laser. A BG39 bandpass (transmission 330-680 nm) filter was used for IRSL, while a 925 nm sharp

cut-off long pass detection filter (OD: 4; transmission: 925-1075 nm) was used for IRPL. The laser light was delivered to the sample using the fiber optics.

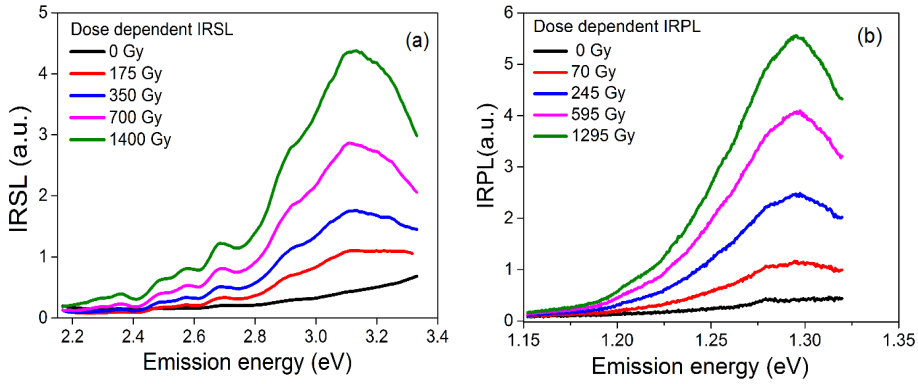

Figure 2.8: Beta dose dependent (a) IRSL spectrum (b) IRPL spectrum of a sedimentary K-feldspar (R47).

As an example of data obtained from the Risø spectrometer, Figure 2.8(a) shows the dose dependent IRSL spectrum for the sedimentary K feldspar (R47); the anti Stokes ~ 3.1 eV (400 nm) emission observed here is commonly used in IRSL dating (see e.g. Baril and Huntley, 2003).

Figure 2.8(b) shows the dose dependent IRPL spectra from the same sample (R47); these are steady state, Stokes shifted spectra, which I discovered during my Ph.D. research; the details of this new signal (IRPL) are discussed in detail in Chapter 7.

The main experiments undertaken using the Risø TL/OSL spectrometer attachment are summarised in Table 2.2.

2.4 Samples

The samples used in this study are variety of feldspar mineral specimens and sedimentary feldspars summarized in Table 2.3, and their code is used in the following chapters, and a feldspar analogue system YPO_4: Ce (0.5%), Sm (0.5%). The K, Na, Ca contents of these samples were measured using the Risø XRF attachment. The Mn and Fe contents were measured in some of these samples using inductively coupled plasma mass spectrometry (ICP-MS) for further studies reported in chapter 4 and 5.

Table 2.2: Main experiments carried out using the Risø spectrometer using feldspar.

#	Experiments	Representative figures
1.	Radioluminescence (RL)	Chapter 3, Figure 3.1
2.	Dose dependent IRSL	Chapter 2, Figure 2.8
3.	IRSL and IRPL comparison	Chapter 7, Figure 7.4
4.	Dose dependent IRPL	Chapter 7, Figure 7.2b,7.3d,7.6a
5.	Development of IRPL dating protocol	Chapter 7, Figure 7.6, 7.7

Table 2.3: List of samples, their bulk composition as determined by X-Ray fluorescence (XRF). S represents feldspars of sedimentary origin, and M represents museum single crystal samples. Fe and Mn concentration were measured using IC-PMS.u/k:Unknown

Sample Code	Sample Name	Type of Feldspar	Provenance	K	Na	Ca	Fe (ng/g)	Mn ng/g	Fe/Mn
R41	Orthoclase, Brazil	M	Brazil	0.97	0.01	0.01	-	-	-
R28	R28	M	Switzerland	0.95	0.05	0	-	-	-
R42	E38133	S	China	0.91	0.08	0.01	1185	20.5	58
R43	E38131	S	China	0.91	0.08	0.01	943.2	17.4	54
R44	K-feldspar (Spain)	M	Spain	0.91	0.08	0.01	753.4	19.4	39
R45	Amazonite, Norway	M	Norway	0.87	0.12	0.01	-	-	-
R46	Cleavelendite Iveland, Eveje Norway	M	Norway	0.86	0.13	0.01	-	-	-
R47	963601 FK	S	China	0.85	0.12	0.03	207.3	3.3	63
R48	Amazonite, Russia	M	Russia	0.83	0.16	0.02	-	-	-
R49	D38163	S	China	0.83	0.16	0.02	691.9	9.4	74
R50	Microcline	M	u/k	0.8	0.18	0.01	1597.4	28.3	56
R51	Cleavelendite	M	Norway	0.78	0.21	0.01	-	-	-
R52	Graphic Amazonite	M	Norway	0.77	0.22	0.01	-	-	-
R53	Moon stone India	M	India	0.76	0.22	0.02	-	-	-
R54	Orthoclase, Eveje Norway	M	Norway	0.75	0.23	0.02	-	-	-
R55	Oligoclase (Albite)	M	u/k	0.74	0.24	0.02	-	-	-
R56	Sanidine-1	M	u/k	0.52	0.46	0.02	2124.5	48.1	44
R57	Sanidine-2	M	u/k	0.43	0.53	0.04	1537.3	9.7	158
R58	Oligoclase-1	M	u/k	0.27	0.63	0.1	1607.7	22.3	72
R59	Sunstone, India	M	India	0.04	0.89	0.07	-	-	-
R60	Labradorite	M	u/k	0.08	0.79	0.13	-	-	-
R61	Plagioclase, Iveland S Norway	M	Norway	0.06	0.69	0.25	-	-	-
R62	Plagioclase (Bytownite)	M	UK	0.02	0.31	0.67	-	-	-
R63	LUM2524	S	Iceland	0.03	0.29	0.69	36790.7	538.1	68
R64	LUM2518	S	Iceland	0.01	0.15	0.85	11263.7	155.9	72

Bibliography

[1] Baril, M.R., Huntley, D. J. (2003b). Infrared stimulated luminescence and phosphorescence spectra of irradiated feldspars. J. Phys.: Condens. Matter 15, 8029–8048.

[2] Bøtter-Jensen, L., Thomsen, K.J., Jain, M. (2010). Review of optically stimulated luminescence (OSL) instrumental developments for retrospective dosimetry. Radiat. Meas. 45, 253-257.

[3] Henderson, B., & Imbusch, G. F. (2006). Optical spectroscopy of inorganic solids (Vol. 44). Oxford University Press.Chicago

[4] Lapp, T., Kook, M., Murray, A. S., Thomsen, K. J., Buylaert, J. P., Jain, M. (2015). A new luminescence detection and stimulation head for the Risø TL/OSL reader. Radiation Measurements, 81, 178–184

[5] Lapp, T., Jain, M., Thomsen, K. J., Murray, A. S., Buylaert, J. P. (2012). New luminescence measurement facilities in retrospective dosimetry. Radiation Measurements. 47, 9, 803–808

[6] Pelant, I., & Valenta, J. (2012). Luminescence spectroscopy of semiconductors. Oxford University Press.

[7] Proposed conceptual report: Upgrade of Risø Horiba Fluorolog spectrometer for Low Temperature and X-ray Excited luminescence studies (2014). By Dr. Nigel Poolton, Spectral Imaging (UK). (Internal report)

[8] Shafer, A. B., Megill, L. R., & Droppleman, L. (1964). Optimization of the Czerny–Turner spectrometer. JOSA, 54(7), 879-887.

[9] Technical report: Optical interface for high sensitivity, single photon spectrometer (2016) By Amit Kumar Prasad, Student number 136240, DTU Nutech, Roskilde-4000, Denmark (Internal report)

[10] User's manual: Fluorolog 3 spectrofluorometer and accessories (2008) by Horiba Jobin Yvon Inc.

[11] Users Manual Model 335 Temperature Controller (2014) by Lake Shore Cryotronics, Inc.

[12] User's Manual VCM-D1 X-ray Shutter Driver (2013) by Vincent Associates, a Division of VA, Inc.

Chapter 3

Probing luminescence centers in Na rich feldspar

A. K. Prasad[1], T. Lapp[1], M. Kook[1], M. Jain[1]

[1] *Center for Nuclear Technologies, Technical University of Denmark, DTU Risø Campus, Roskilde 4000, Denmark.*

Published in: Radiation measurements, Volume 90, July 2016.

Abstract: In contrast to the detailed investigations on the dosimetric electron trap in feldspar only little has been done to understand the luminescence centers. We use a comparison of multiple spectroscopic techniques, site selective photoluminescence spectroscopy and time resolved measurements to further our understanding of the luminescence mechanisms and recombination sites, in a sample of Na rich plagioclase feldspar (oligoclase). Both the UV and violet-blue emissions show resonant excitations arising from a distribution of energy levels. We propose, contrary to the general understanding, that the green emission may not arise from Mn^{2+} in our sample and that photoionisation of this centre

may be possible by excitation to the band tail states. The deep red emission is tied to the Fe^{3+}, and the exponential rise in the UV excitation efficiency of this centre is discussed in the context of the band-tail model.

Keywords: Na-feldspar, X-Ray excited optical luminescence, radioluminescence, photoluminescence, band-tail model

3.1 Introduction

The photoemissions from feldspars are widely used in retrospective dosimetry and optical dating of geological and archaeological events (Huntley et al., 1985; Jain et al., 2014; Krbetschek et al., 1997). Feldspars are ubiquitous in nature, and the dosimetric signal measured as infra-red stimulated luminescence (IRSL) shows growth up to 1 kGy dose range, allowing reconstruction of geological history up to about 0.5 Ma. However, this signal suffers from anomalous, athermal fading. A large body of work exists on the dosimetric, electron trapping centre which gives rise to this IRSL signal (Hutt et al., 1988; Poolton et al., 1989; Jain and Ankjærgaard, 2011; Andersen et al., 2012; Kars et al., 2013, etc.); these studies include both the tunnelling behaviour and the mapping of the energy level within the band gap. In contrast, only little has been done to characterise the recombination centers. Based on spectral characteristics of feldspars (Krbetschek et al., 1997), it is inferred that the UV emission arises from an intrinsic defect (Guinea et. al, 1996), the blue emission, common to most feldspars, from a hole-bearing oxygen atom adjacent to two Al atoms ($Al - O^- - Al$) (Finch and Klein et al., 1999), the green-orange emission, characteristic of some Na-feldspars, from Mn^{2+} luminescence centre occupying Ca sites (Geake et al., 1977), and the deep red emission band from tetrahedral Fe^{3+} ($^4T_1 \rightarrow {}^6A_1$ transition) substituting for Al^{3+} (Geake et al., 1977; Telfer et al., 1975; White et al., 1986). A more comprehensive characterisation of the recombination centres is lacking. For example, there is little understanding of the distribution as well as the positions of the energy levels of these defects within the band gap. Similarly, there is little information on the characteristic fluorescence/phosphorescence lifetimes of these emissions.

The objective of this study is to further understand the luminescence transitions within the recombination centres in feldspars, and explore their energy structure and distribution within the bandgap. A special

focus is given on the green and deep red emission. We use a combination of probing methods: X-rays in keV regime (X-ray excited optical luminescence: XEOL), Sr^{90}/Y^{90} beta particles (radioluminescence: RL) and UV-VIS-IR photons (photoluminescence: PL). These beta and X-ray excitations directly ionize the host lattice because the incident energy is much higher than the band gap of the feldspars $\sim 7.7\,\text{eV}$ (Poolton et al., 2006) leading to electron-hole recombination at the luminescence centers. In contrast, the optical excitation (PL; 1.9 eV - 4.86 eV) allows the possibility of probing the energy structure of these centers and possibly their disposition within the band gap using site selective spectroscopy. We also report on the luminescence lifetimes on microsecond and millisecond time scales characteristic of these centres.

3.2 Instrumentation and sample

We measured a set of feldspar museum specimens reported previously by Ankjærgaard et al. (2009) and Morthekai et al. (2013) using RL and PL. Of these a representative oligoclase sample (Oligoclase 1 of Morthekai et al., 2013) was chosen for detailed studies presented here as this sample had relatively higher optical sensitivity compared to the other samples, and showed all the typical bands reported for feldspars (Krbetschek et al., 1997). The main cationic constituents of the sample are (in molar %): Na-73.7, Ca-18.9 and K-7.4; their concentrations were measured using inductively coupled plasma mass spectrometry (ICP-MS; Morthekai et al., 2013). The grain size used in the present studies was in the range of 90–180 µm.

To measure the RL, the sample was mounted with a silicon oil into the steel cup and placed in the Risø TL/OSL Reader (Model DA 20) equipped with a Sr^{90}/Y^{90} beta source (dose rate 0.1 Gy/s). The signal was collected through a fiber bundle; the circular (3 mm ϕ) end of the bundle looked at the sample under the beta source, while the other end arranged in an array of two rows was coupled to the Shamrock 193i spectrograph which dispersed the spectra on a high sensitivity EMCCD (iXon Ultra 888). The RL spectra were recorded from 250 nm to 1050 nm by setting the 300 lines/mm grating in four overlapping positions. The RL spectra were corrected for the spectral functions of grating, optical fibre and EMCCD.

The photoluminescence spectra were measured using Horiba Fluo-

rolog 3 spectrofluorometer. A 450 W Xenon CW lamp was used for excitation within a wavelength range of approximately 255 nm - 600 nm, with required wavelengths selected using a double grating Cherny-Turner excitation monochromator. Emission spectra in the range of 290 nm - 600 nm were measured with a double grating Cherny-Turner spectrometer equipped with a photomultiplier tube (PMT). Spectra from 620 nm to 1000 nm were measured with Jobin-Yvon, HR-320 spectrometer (300 lines/mm grating) coupled to a liquid nitrogen cooled CCD detector, because of better efficiency of the CCD compared to PMT in the red-IR region. All spectra were corrected for the instrument response and photon flux. Appropriate long-pass filters were placed between the sample and the emission monochromator to remove second order diffraction of the primary excitation light. The PL phosphorescence decay was measured with the pulsed Xe-lamp placed in the same housing as the CW-lamp. The required wavelength of the excitation pulses was selected with the excitation monochromator and emission was recorded with the emission monochromator. The integration time of the emission collection was 100 ms and the initial delay of the system was 0.05 ms; all the measurements used flash counts of 100 to improve counting statistics.

XEOL was measured using a 40 kV X-ray tube installed on Horiba Fluorolog-3 spectrofluorometer. The X-ray tube was operated at 39.7 kV anode voltage and 95.7 mA anode current, and sample chamber pressure of $2.3 \times 10^{-}4$ mB (vacuum was used because of interlock constraints). All low temperature luminescence measurements were accomplished in the same system using variable temperature (7-300 K) closed loop He cryostat operated with a sample chamber pressure at $2.4 \times 10^{-}5$ mB, integrated into the Horiba emission/excitation spectrofluorometer. The proportional integral-derivative (PID) temperature control is provided through a Lakeshore (model 335) control unit. The sample grains were directly mounted on a copper-based sample holder (a cold finger) with the help of carbon tape.

3.3 Comparison of the XEOL, PL and RL spectra

Figure 3.1 shows comparison of normalised XEOL, PL and RL spectra of our oligoclase sample. Four broad emission peaks can be observed at around 1.70, 2.2, 3.1 and 3.8 eV.

The XEOL and the RL data are broadly similar, suggesting the same mechanism for both these cases; this is not surprising since both the 40 kV X-rays and the high-energy beta particles (mean energy 600 keV) have energy higher than the band gap and access the entire sample volume. However, there is a hump at about 2.5 eV in the RL spectra which is not present in XEOL; it needs to be confirmed if this hump is real or it is a measurement artefact.

In contrast to the RL/XEOL spectra, the relative intensity of the 2.2 eV peak is strongly subdued in the PL spectra, suggesting that the optical cross-section of the green emission centre is small compared to the other centers; this, however, is not an issue in RL and XEOL as the electron relaxation occurs from the conduction band in the latter mechanisms. The spectral bands observed in our work are in good agreement with the previous studies (Krbetschek et al., 1997).

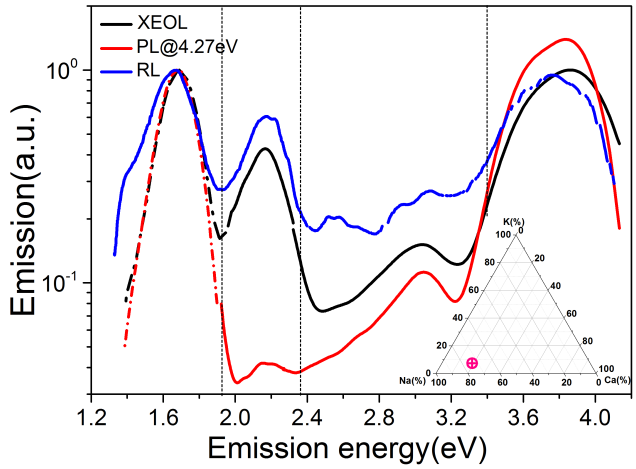

Figure 3.1: A comparison of the XEOL (black), PL (Red) and RL (blue) spectra. In the case of XEOL and PL, the solid curves are the data collected through the PMT channel, whereas the dotted curves are collected using the CCD channel. A 610 nm long pass filter was used to avoid excitation scattered light for the collection of CCD data

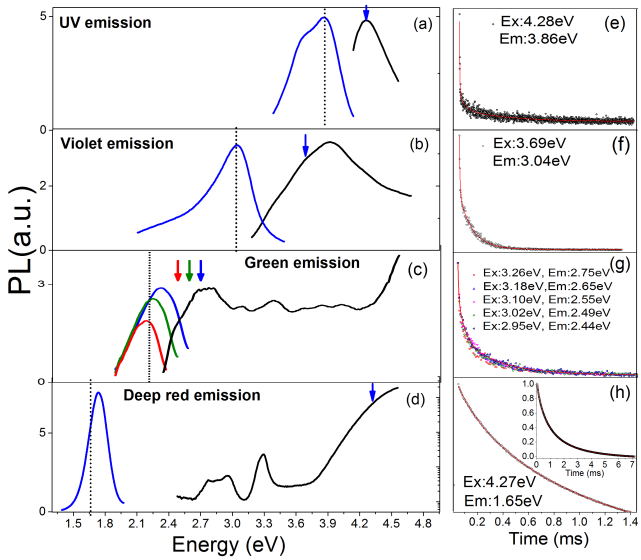

Figure 3.2: Site selective excitation and emission spectra, and phosphorescence decay data of Na feldspar. a-d: the black curves are the excitation spectrum while the coloured curves are emission spectra. The excitation spectrum in (d) is plotted on the log intensity scale while all the others are on the linear scale with arbitrary units. The emission spectra are obtained with the excitation energy marked by the arrow. The excitation spectra are obtained by fixing the emission in the narrow window shown as the dotted vertical line. (e) to (h) phosphorescence decay curves corresponding to each emission plotted on the left figures. The excitation and emission energies used in time-resolved measurements are mentioned in the legends.

3.4 Site selective photoluminescence spectra and luminescence lifetimes

PL excitation and emission spectra were measured to get further information about the energy structure of the defects giving rise to the above mentioned emission bands. The results are presented in Figure 3.2(a)...(d) and discussed below:

UV emission: The black curve in Figure 3.2(a) shows excitation spectrum for the emission at 3.86 eV. There is a broad, well defined excitation peak at 4.27 eV with a FWHM of $\sim$ 0.4 eV. The blue curve shows the corresponding emission spectrum excited at 4.27 eV consisting of two overlapping peaks at 3.86 eV and 3.67 eV. Figure 3.2(e) shows the phosphorescence decay of the emission at 3.86 eV excited at 4.28 eV.

We attempted fitting these data with a linear combination of discrete exponentials, a stretched exponential, or a Becquerel function; of these only the discrete exponentials function gave satisfactory fit to all the phosphorescence data presented in this study.

The UV phosphorescence decay curve was best fitted with three exponentials with characteristic lifetimes 0.0023 ms, 0.046 ms and 0.36 ms. The shortest lifetime may not be resolved accurately as the maximum data resolution in our system is 1 µs

Violet-blue emission: The excitation spectrum (black curve) for the 3.04 eV emission is plotted in Figure 3.2(b); the spectrum appears as a broad asymmetric peak with a FWHM of $\sim$ 1 eV. It is likely that this peak consists of several overlapping peaks. The emission spectrum (the blue curve) was obtained using excitation at 3.69 eV; it is broad and asymmetric, and peaks at 3.06 eV. The phosphorescence decay (excitation at 3.69 eV and emission at 3.04 eV), slightly slower compared to the UV emission, was best fitted to a sum of 3 exponentials (Figure 3.2(f)) with decay times 0.0043 ms, 0.095 ms and 0.21 ms.

Green emission: Figure 3.2(c) shows the excitation spectrum (black curve) for the emission at 2.21 eV. The excitation spectrum is largely flat with minor peak structures. There is a sharp decrease in excitation efficiency below 2.7 eV and an increase above 4.2 eV; no discrete resonance peaks are observed as in contrast to the other emissions.

Interestingly, the emission peak (blue, green and red curves in Figure 3.2(c), shows a shift to the red side with a decrease in the excitation energy (discussed in detail in the next section). The phosphorescence decay curves were measured using the excitation energies corresponding to emission peaks, for e.g. excitation at 3.26 eV for emission at 2.75 eV, and excitation at 2.95 eV for emission at 2.44 eV and so on (Figure 3.2(g). It was observed that the different emissions have similar characteristic decay. The fitting analysis for the excitation-emission combination 2.95 eV and 2.44 eV, respectively gave lifetimes of 0.0087 ms, 0.10 ms and 0.66 ms.

Deep red emission: The excitation spectrum (black curve) for the emission at 1.65 eV is plotted in Figure 3.2(d) (with the logarithmic scale for the excitation intensity). There is an exponential rise in the excitation curve between 3.85 - 4.86 eV, and resonance peaks are observed at 3.28, 2.95 and 2.75 eV. The emission spectrum (blue curve) was measured with the 4.27 eV excitation using the CCD channel, and shows a symmetric

peak centered at 1.7 eV. The phosphorescence decay for this emission was also measured with 4.27 eV excitation (Figure 3.2(h)) and contained three exponential components with the lifetimes of 0.14, 0.67 and 2.3 ms. In order to investigate the relationship between the decay kinetics and the emission, we compared the shapes of the fluorescence emission spectrum and the phosphorescence emission spectra obtained after various delays with respect to the excitation pulse. It is observed that the fluorescence and phosphorescence spectra are broadly similar; however, a closer examination shows that there a slight but systematic blue shift in the phosphorescence emission with greater delay (Figure 3.3).

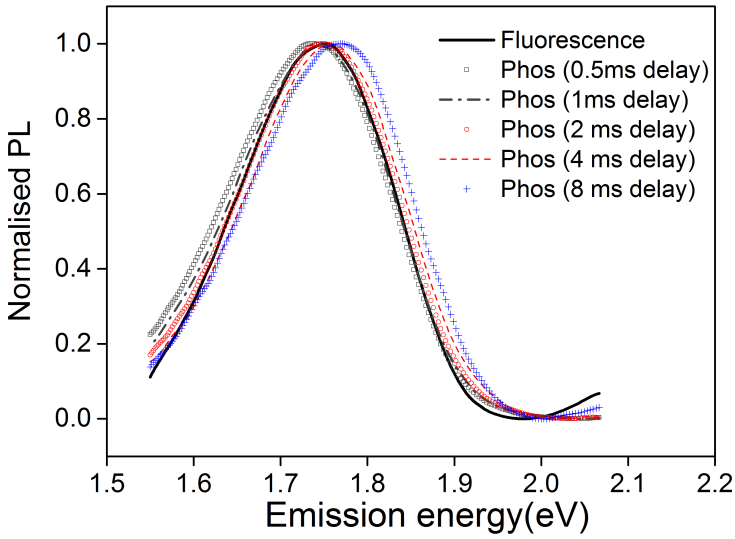

Figure 3.3: Comparison of fluorescence and phosphorescence spectra of the deep-red emission using 4.27 eV excitation. The black curve shows fluorescence spectra measured with continuous wave (CW) Xe-lamp excitation. The other curves represent phosphorescence emission spectra measured after a delay of 0.5, 1, 2, 4 and 8 ms with respect to excitation pulse. There is a systematic shift of the peak emission with delay as can be clearly observed on the higher energy limb. We used excitation and emission slit widths of 10 nm for phosphorescence measurement, in comparison to 2 nm for fluorescence measurement, to obtain a high signal-to-noise ratio.

3.5 Dependence of emission peak on the excitation energy in the green emission

Based on the result in Figure 3.2(c) , we explored in detail the dependence of the emission spectra on the excitation energy. We observed that there is a systematic shift in emission maxima from 2.13 to 2.49 eV with a concomitant increase in intensity, as the excitation energy is tuned from 2.38 to 2.88 eV (Figure 3.4). Within the range of these data there is an almost linear correlation between the emission and the excitation peak energy (Figure 3.4(a) inset). The normalized (by emission maxima) spectra in Figure 3.4(b) show that the peaks become systematically narrower (FWHM) as they shift to a lower energy.

We further explored the behaviour of the green emission with changes in sample temperature. The same measurements as those presented in Figure 3.4 were repeated at 7 K, 100 K and 295 K using the cryogenic attachment. Normalised spectra for each temperature for three different excitation energies (at 2.81, 2.63 and 2.43 eV denoted by arrows with the same colour) are shown in Figure 3.5(a). The shapes of the 295 K (solid curve), 100 K (plus) and 7 K (circle) are broadly similar with minor deviations at the low energy end. This deviation is particularly conspicuous for the 2.43 eV excitation, where a small hump at $\sim$ 1.93 eV is observed in the 295 K and 100 K data.

A strong thermal quenching was observed in the green emission; this effect can be observed in the integrated counts (area under the emission peak) obtained after each excitation energy at different temperatures (Figure 3.5(a), inset). There is a reduction in emission intensity by a factor of two due to increase in the sample temperature from 100 to 295 K, and a relatively minor decrease from 7 K to 100 K. Similarly, as observed in Figure 3.4(a), there is an increase in emission intensity, and emission energy with excitation energy at each temperature. It is observed that the emission intensity increases exponentially with excitation energy, with a slope of 3.08 eV^{-1} at 7 K and 100 K, and 3.04 eV^{-1} at295 K (Figure 3.5(a), inset). We also compared the phosphorescence decay at 295 K and 7 K. There is a significant increase in the overall decay rate at room temperature compared to 7 K, as demonstrated for the 2.69 and 2.81 eV excitations (Figure 3.5(b)).

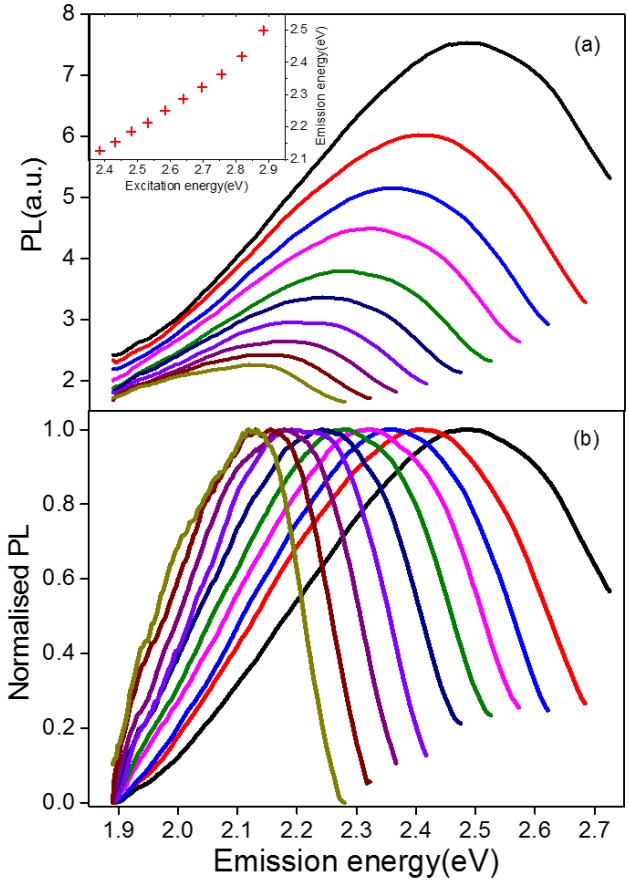

Figure 3.4: The dependence of the emission peak energy of the green band on the excitation energy. (a) Excitation dependent emission spectra. The excitations were done at approximately every 0.05 eV between 2.38 eV (corresponding emission curve in black) and 2.88 eV (corresponding emission curve in yellow). The inset shows the emission peak energy vs. the excitation energy. (b) Normalized curves of the data in (a).

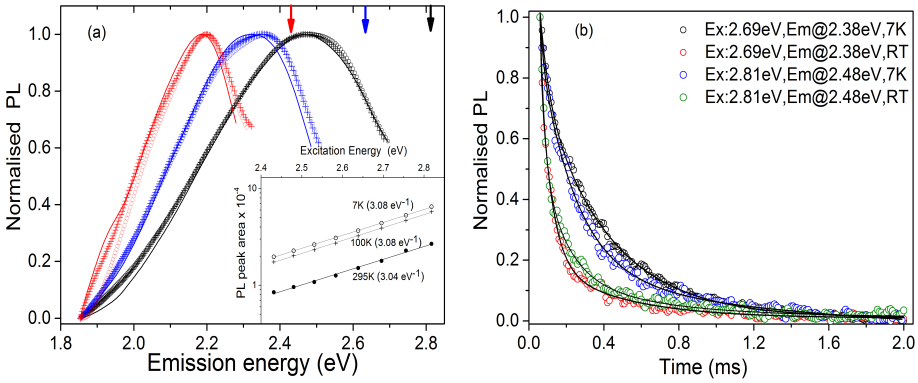

Figure 3.5: (a) The emission spectra at 7 K, 100 K and room temperature (RT) represented by open circle, plus and solid line, respectively. These emission spectra are obtained using excitation with 2.81 eV (black), 2.63 eV (blue) and 2.43 eV (red) light, indicated by the same coloured downward facing arrows. The inset shows area under the emission peak for different excitations at 7 K, 100 K and 295 K sample temperatures; note that the y axis is on a logarithmic scale. (b) Phosphorescence decay data shown for the excitation, emission and temperature conditions as mentioned in the legend.

3.6 Summary and Discussion

RL and XEOL for the excitation energies described in this study, arise from electron-hole recombination through the delocalised bands (similar to OSL and TL), whereas PL occurs thorough selective excitation of a centre. A general similarity between the RL, XEOL, and PL spectra Figure 3.1 demonstrates that the same recombination sites must participate in both the delocalised (RL, XEOL) and localised mechanisms (PL); hence the results presented here are also relevant for dosimetric signals produced through delocalised transitions such as TL and OSL emissions. Based on the PL emission/excitation characteristics we conclude that both the UV and violet-blue emissions arise from deep localised defects within the bandgap, our present data however does not allow determination of the exact energy level. Nonetheless, the broad asymmetric bands suggest that there is distribution of energy levels either in the excited or the ground state or both. The FWHM of excitation spectra for the UV and violet-blue emission was $\sim$ 0.4 eV and 1 eV, respectively, indicating the width of the corresponding energy level distributions. The phosphorescence decay ranges from few µs to hundreds of µs, with an

overall faster decay for the UV compared to the violet-blue emission. In comparison to the UV emission, the much wider excitation and emission peaks and the slower decay kinetics of the violet-blue emission are likely related to the distribution of these defects in the lattice. For example, it is possible that violet-blue emission may involve defect clusters, which lead to a flatter wider emission peak and slower decay because of charge transfer across defects.

The green emission is much stronger in XEOL and RL compared to PL suggesting that direct photo-excitation within our data range is relatively inefficient. The green-orange/red emission has typically been ascribed to Mn^{2+} in the literature (e.g., Krbetschek et al., 1997) due to the spin and parity forbidden $^4T_1 \rightarrow {}^6A_1$ transition. This emission in the host lattice typically occurs with a lifetime of the order of tens of milliseconds within the 3d shell, where the electrons are strongly coupled to lattice vibration and affected by crystal field strength and site symmetry (e.g. Shi et al., 2010). In our phosphorescence data, we observe the dominant lifetimes of the order of hundreds of microseconds to less than a fraction of a millisecond, which is not consistent with the interpretation that the green emission is arising from discrete Mn^{2+} defects. We, therefore, interpret that another unknown defect, rather than Mn^{2+} is responsible for the green emission in our sample.

The relatively flat excitation spectrum for the green emission indicates a distribution of excitation energies (continuous overlapping emissions); such a distribution could arise from the regions of clustered impurity, or because of the role of the band tail states. The interpretation of a distribution of states is supported by a strong dependence of emission energy and intensity on the excitation energy. A higher excitation gives rise to wider range of emission energies in comparison to the excitation to the lower energy band tail states; more specifically, the high energy emissions are systematically eliminated as we decrease the excitation energy (Figure 3.4(a)). Measurements at cryogenic temperatures neither give higher resolution peaks, nor show a shift in the emission peak which is characteristic of the increasing crystal field effect on Mn^{2+}. Instead the shape of the emission spectra at 7 K and 100 K is broadly similar to that at the room temperature, supporting that these emissions arise from a distribution of states. The main effect of cooling is observed to be an increase in emission intensity with a simultaneous increase in the phosphorescence lifetime; this suggests that at higher temperatures re-

laxation may be occurring via lattice phonons, supporting a Mott–Seitz type (e.g. Pagonis et al., 2010) thermal quenching mechanism.

The excitation efficiency data may give insights into the energy of the defect centre responsible for the green emission. The excitation spectrum for the green emission shows a rise at 4.2 eV; however, this rise is not reliable because of the change in emission peak positions as a function of excitation energy. In fact there is a rapid increase of violet-blue and deep red emission for excitation energies >3 eV, which makes it impossible to distinguish the characteristic green emission above this energy; thus we cannot conclusively map this defect with respect to the conduction band edge.

However, the exponential rise in the emission intensity with excitation energy, at the rate of $3.08\,\mathrm{eV}^{-1}$ is insightful (Figure 3.5(a) inset); the inverse is almost identical to the Urbach energy of 0.32 eV estimated from a sodium feldspar sample by Poolton et al. (2009). Because of this remarkable similarity with our result, we interpret that the increase in excitation efficiency at higher energies results from the exponential increase in the density of the band tail states with an Urbach width of 0.32 eV (=1/3.08) in our sample, rather than due to possible 'local clustering' of the responsible defect. The band tail states also explain the widening of the emission spectra with excitation energy.

The excitation spectra for deep red emission (1.65 eV) have many resonant features which can be tied to the known transitions in Fe^{3+} (Poolton et al., 1996). The prominent phosphorescence decay is observed to be on the millisecond time scales confirming the spin forbidden nature $^4T_1 \rightarrow {}^6A_1$ transition. Furthermore, the similarity of the fluorescence and phosphorescence spectra confirm that the emission is due to the forbidden transition of Fe^{3+}; a slight systematic shift in the peak energy of the phosphorescence spectra with delay time with respect to the excitation pulse, suggests slightly different electronic environment of Fe^{3+} leading to a slightly different lifetime as well as emission energies. This interpretation explains the fact that multiple exponentials are required approximate the phosphorescence decay of the red emission. We also observed that the excitation spectra have a continuum in the form of an exponential rise from 3.6 to 4.86 eV. This exponential rise is either related to the fine splitting and overlapping distribution of the higher excitation states of Fe^{3+} due to clustered impurities or, as in the case of green emission, it could be due to the access to the band tail states with an exponential

distribution of the density of states. The characteristic energy for the exponential rise is estimated to be $\sim 0.23\,\mathrm{eV}$ (inverse of the exponential constant of $4.3\,\mathrm{eV}^{-1}$ obtained for data from 3.8 to 4.2 eV), which is similar to that derived for the green emission ($= 0.32\,\mathrm{eV}$). The difference in the exponential constants for the two emissions could be reconciled with the fact that the distribution of band-tail states may differ slightly in the vicinity of different impurities occupying different positions in the lattice. Clustered impurities, for example, possible due to high concentration of Fe^{3+}, may significantly affect the band tail states by altering the local lattice structure. Equally, impurity clusters could lead to the formation of charge transfer bands within the forbidden gap (sub-bands), which could give rise to a similar exponential trend. Further research is required to differentiate between the two models; however, given the similarity of the exponential constants for the green and the red emission we currently favour the band tail model.

3.7 Conclusion

We help further constrain the luminescence model of feldspars based on multiple spectroscopic techniques and time resolved measurements. Our data suggest that the different emissions (UV, violet-blue, green, deep red) arise from the different sites, and that there occurs a distribution of energy levels for each emission. We conclude that the green emission is likely not related to Mn^{2+} in our samples, whereas the deep red emission is related to the Fe^{3+}. We interpret that the exponential increase in the excitation efficiency of the green and red emission centres is due to direct transition to the band tail states.

3.8 Acknowledgement

We thank the two anonymous referees for their critical input. Dr. N. R. J. Poolton is thanked for discussions during the early phase of this work.

Bibliography

[1] Andersen, M. T., Jain, M., Tidemand-Lichtenberg, P. (2012). Red-IR stimulated luminescence in K-feldspar: Single or multiple trap origin? Journal of Applied Physics, 112(4), 043507.

[2] Ankjærgaard, C., Jain, M., Kalchgruber, R., Lapp, T., Klein, D., McKeever, S. W. S, Murray, A. S.,& Morthekai, P. (2009). Further investigations into pulsed optically stimulated luminescence from feldspars using blue and green light. Radiation Measurements, 44(5), 576-581.

[3] Finch, A. A., & Klein, J. (1999). The causes and petrological significance of cathodoluminescence emissions from alkali feldspars. Contributions to Mineralogy and Petrology, 135(2-3), 234-243.

[4] Garcia-Guinea, J., Townsend, P. D., Sanchez-Munoz, L., & Rojo, J. M. (1999). Ultraviolet-blue ionic luminescence of alkali feldspars from bulk and interfaces. Physics and chemistry of minerals, 26(8), 658-667.

[5] Geake, J. E., Walker, G., Telfer, D. J., & Mills, A. A. (1977). The cause and significance of luminescence in lunar plagioclase. Philosophical Transactions of the Royal Society of London A: Mathematical, Physical and Engineering Sciences, 285(1327), 403-408.

[6] Huntley, D. J., Godfrey-Smith, D. I., & Thewalt, M. L. (1985). Optical dating of sediments. Nature, 313(5998), 105-107.

[7] Hütt, G., Jaek, I., & Tchonka, J. (1988). Optical dating: K-feldspars optical response stimulation spectra. Quaternary Science Reviews, 7(3-4), 381-385.

[8] Jain, M., & Ankjærgaard, C. (2011). Towards a non-fading signal in feldspar: insight into charge transport and tunnelling from time-resolved optically stimulated luminescence. Radiation Measurements, 46(3), 292-309.

[9] Jain, M. (2015). Feldspar, Infrared-Stimulated Luminescence. Encyclopedia of Scientific Dating Methods, 279-284.

[10] Jain, M., Sohbati, R., Guralnik, B., Murray, A. S., Kook, M., Lapp, T., Prasad, A.K., Thomsen, K.J. & Buylaert, J. P. (2015). Kinetics of infrared stimulated luminescence from feldspars. Radiation Measurements, 81, 242-250.

[11] Kars, R. H., Poolton, N. R., Jain, M., Ankjærgaard, C., Dorenbos, P., & Wallinga, J. (2013). On the trap depth of the IR-sensitive trap in Na-and K-feldspar. Radiation Measurements, 59, 103-113.

[12] Krbetschek, M. R., Götze, J., Dietrich, A., & Trautmann, T. (1997). Spectral information from minerals relevant for luminescence dating. Radiation Measurements, 27(5), 695-748.

[13] Morthekai, P., Jain, M., Gach, G., Elema, D. R., & Prip, H. (2013). Dependence of (anomalous) fading of infra-red stimulated luminescence on trap occupancy in feldspars. Journal of Luminescence, 143, 704-709.

[14] Pagonis, V., Ankjærgaard, C., Murray, A. S., Jain, M., Chen, R., Lawless, J., & Greilich, S. (2010). Modelling the thermal quenching mechanism in quartz based on time-resolved optically stimulated luminescence. Journal of luminescence, 130(5), 902-909.

[15] Poolton, N. R. J., & Bailiff, I. K. (1989). The use of LEDs as an excitation source for photoluminescence dating of sediments. Ancient TL, 7(1), 18-20.

[16] Poolton, N. R. J., Bøtter-Jensen, L., & Johnsen, O. (1996). On the relationship between luminescence excitation spectra and feldspar mineralogy. Radiation measurements, 26(1), 93-101.

[17] Poolton, N. R. J., Mauz, B., Lang, A., Jain, M., & Malins, A. E. R. (2006). Optical excitation processes in the near band-edge region of KAlSi3O8 and NaAlSi3O8 feldspar. Radiation measurements, 41(5), 542-548.

[18] Poolton, N. R. J., Kars, R. H., Wallinga, J., & Bos, A. J. J. (2009). Direct evidence for the participation of band-tails and excited-state tunnelling in the luminescence of irradiated feldspars. Journal of Physics: Condensed Matter, 21(48), 485505.

[19] Shi, L., Huang, Y., & Seo, H. J. (2010). Emission red shift and unusual band narrowing of Mn^{2+} in NaCaPO4 phosphor. The Journal of Physical Chemistry A, 114(26), 6927-6934.

[20] Sohbati, R., Murray, A., Jain, M., Thomsen, K., Hong, S. C., Yi, K., & Choi, J. H. (2013). Na-rich feldspar as a luminescence dosimeter in infrared stimulated luminescence (IRSL) dating. Radiation Measurements, 51, 67-82.

[21] Telfer, D. J., & Walker, G. (1975). Optical detection of Fe3+ in lunar plagioclase. Nature, 258(5537), 694-695.

[22] White, W. B., Matsumara, M., Linnehan, D. G., Furukawa, T., Chandrasekhar, B. K. (1986). Absorption and luminescence of Fe^{3+} in single-crystal orthoclase. Am. Mineral. 71 (14) 15–19.

Chapter 4

Strong excitation-energy dependent PL emission in a wide bandgap aluminosilicate (feldspar): role of the sub-conduction band tail states

A. K. Prasad[1] & M. Jain[1]

[1] *Center for Nuclear Technologies, Technical University of Denmark, DTU Risø Campus, Roskilde 4000, Denmark*

Under review

Abstract: The phenomenon of excitation-energy-dependent emission is well known from photoluminescence (PL) studies of polar solvents and carbon-based nanoparticles. In case of polar solvents, this effect (commonly known as the 'red edge effect') is understood to arise from solute-solvent interactions, whereas, in case of quantum dots, the origin is still

heavily debated. Understanding the red edge effect has important bearings on the potential applications of these materials. To our knowledge, excitation-energy-dependent emission has never been reported from large crystalline materials, except for a very recent article by our group (Prasad et al., 2016). Prasad et al.(2016) reported this effect in the orange-green emission from a Na-feldspar (a ubiquitous aluminosilicate), and argued that it possibly arises from the band tail states or a charge transfer band.

In this study, we make a thorough investigation of the excitation-energy-dependent emission in six different feldspar samples. Based on low temperature PL investigations and time-resolved fluorescence and phosphorescence studies, we conclude that this effect is universal in feldspar, irrespective of mineralogy, and that it arises from photoionisation of a deep lying defect and its subsequent interaction with the sub-conduction band tail states. This effect can be used to determine the width of the band tail states. We also infer that the orange-green emission does not arise from Mn^{2+} as is commonly believed. Although, the exact origin of the red edge effect requires further investigations, it may be suggested that it is possibly related to surface defects in feldspar.

This article presents a novel, alternative model on the origin of red edge effect, which may have future implications for designing tunable light sources using feldspar and understanding this effect in other crystalline materials.

4.1 Introduction

It is well known that fluorescence spectra in viscous polar solvents show a red shift when excitation energy is lowered towards 'the red edge' of the absorption spectrum (See a detailed review by Demchenko, 2002). This effect known as the red edge effect, is related to the dielectric relaxation of the medium. The red edge effect apparently violates the Kasha's rule (Kasha, 1950; Yanagi & Kataura, 2010) i.e. the emission energy is independent of the excitation energy and always occurs from the lowest electronic/vibrational excited state. However, it is now well established that the red edge effect occurs from an ensemble of excited molecules with a distribution of interaction energies with the solvent, thus giving rise to a spectrum of emission energies (Galley & Purkey, 1970). Over the last four decades since its initial observation (e.g. Galley & Purkey, 1970), this mechanism has been observed in a variety of fluorophores in differ-

ent solvents ranging from high viscosity solutions, glasses and polymer matrices, characterized by frozen or very slow structural dynamics.

Observations of the same effect, i.e. a red shift in the emission with a decrease in the excitation energy, has also been made from graphene quantum dots and other graphene oxide derivatives. A detailed review on this aspect has been given by Gan et al. (2016); these authors note that despite a decade of research, this is still a perplexing phenomenon whose origins are actively debated. Understanding this effect has important implications for use of quantum dots in designing sensors and light sources. Various explanations of this effect include size variations, surface defects, and solution interactions. A solution-induced red edge effect has, for example, been observed in carbon nanodots (Sharma et al., 2016) and Graphene Oxide (Cushing et al., 2013); in the latter case it was described as a giant 'red edge effect', since it spanned about 200 nm. However, there are many examples such as carbon quantum dot solid films, where the 'solution' explanation cannot be applied (Hao et al., 2014; Gan et al. 2016).

Despite the fact that the red edge effect has perplexed and occupied researchers in the materials discussed above, e.g. viscous polar solvents and quantum dots, it has to our knowledge never been reported from wide band-gap crystals. Recently, our group (Prasad et al., 2016) observed this effect in the orange-green photoluminescence spectra from a sample of Na-feldspar. Based on the exponential distribution of the intensity of the PL emission as a function of excitation energy, we attributed this effect to the presence of band tail states or a charge transfer band arising from defect clusters; however, these suggestions have not been confirmed yet. Understanding the origin of the red edge effect in feldspar is particularly important because it is the most common mineral on Earth's crust ($\sim$60%) and other planetary bodies, and is widely used in optical dating, where different emissions are used to derive chronologies of the past climatic and archaeological events (e.g. Roberts & Lian, 2015; Rhodes, 2011; Duller, 1997). Furthermore, the red edge effect, if universal in feldspar or feldspar-like materials, raises the possibility of devising tunable light sources, which is highly-attractive given their widespread availability in nature.

The motivation of this study is to explore the universality of the red edge effect in feldspar, and to understand its origin. It is hoped that this study benefits the application of feldspar in geochronology and gives

new physical insights into the mechanism of excitation-energy-dependent emission phenomenon. We use the term 'red-edge effect', interchangeably with excitation-energy-dependent emission, as a simple descriptive term for the phenomenon; however, note that no solvents are used in our study. Given the size of the red shift described in the following sections, we use the prefix 'Giant' at places, similar to Cushing et al. (2013).

4.2 Feldspar and the Band Tail States

Feldspar is a commonly occurring wide band-gap aluminosilicate ($E_g \sim 7.7\,eV$; Malins et al., 2004), the composition of which can be represented in terms of the ternary system: Orthoclase ($KAlSi_3O_8$), Albite ($NaAlSi_3O_8$) and Anorthite ($CaAl_2Si_2O_8$).

Feldspar is widely used in optical dating, a rapidly developing application in geo-photonics. The use of feldspar as a geochronometer kick started with the discovery of IR stimulated luminescence (IRSL) signal in feldspar (Hutt et al., 1988); today this signal is widely used to date past geological and archaeological events up to last 0.5 Ma (Buylaert et al., 2012; Arnold et al., 2015). This signal arises from resonant excitation, using infra-red light ($\sim$ 870 nm), of electrons in the dosimetric trap, followed by an eventual radiative recombination with a trapped hole elsewhere in the lattice. The concentration of such trapped electrons in feldspar, buried in sediments or rocks, increases with time due to the effect of the surrounding ionising radiation; thus, the intensity of IRSL signal can eventually be calibrated in terms of sample's age (for details of the technique see Duller, 1997, Roberts & Lian, 2015).

Low-mobility conduction band tail states play an important role in charge transfer in feldspar. These states arise due to variation in bonding angles, strain, thermal effects and disorder in the material (Poolton et al., 2002; Smith, 1970). Poolton et al., (2009) demonstrated that IRSL is generated by transport of photo-excited electrons ($\sim$1.45 eV) via diffusion in the band tail states, or by tunnelling from the excited state of the IR trap. Jain and Ankjaergaard (2011) investigated charge transport in the band tail states using time-resolved luminescence. They identified two dominant routes within the band tail states depending on the energy state of the detrapped electron: a) phonon (0.05-0.06 eV) assisted diffusion, and b) quantum mechanical tunnelling. Based on these observations they presented a comprehensive model of the luminescence generating

process in feldspar.

The density of states (DOS) of the band tail states has an exponential dependence on energy (e.g. see Sritrakool et al., 1986).

$$\rho(E) \propto \exp\left(-E^n/E_B\right) \tag{4.1}$$

Where E is the energy of the state measured away from the band edge and for n=1 (the Urbach tail; Urbach, 1953), E_B is a constant (commonly referred to as the band tail width) at which the density falls by e^{-1} of that at the band edge.

There have been few attempts to map the band tail states in feldspar. Poolton et al. (2009) measured the band tails states using excitation spectroscopy after irradiating the sample with X-rays at cryogenic temperature. They estimated a band tail width of 0.4 eV in typical Na and K-feldspars. They concluded that these values are comparable to estimates derived using photo-transferred OSL near band-edge excitation from a synchrotron. Jain and Ankjaergaard (2011) discussed that the presence of band tail states affects the thermal lifetime of the IR trap in feldspar. Li and Li (2013) developed a mathematical model for analysis of isothermal decay of IRSL signal that includes detrapping to the band tail states following Equation (4.1). Based on the analysis of isothermal depletion of IRSL and post IR-IRSL, they estimated the band tail width to be $\sim$ 0.3-0.4 eV. It is worth noting that the approach of Li and Li (2013) is indirect and incomplete, as it neither includes the role of the excited state of the IR trap nor the spatial distribution of the hole centers; both these factors are important for thermal detrapping (Huntley, 2006; Jain and Ankjærgaard, 2011; Jain et al., 2015a). Morthekai et al. (2012) analysed time-resolved IRSL data using a variable range hopping mechanism within the band tail states, and concluded that hopping length decreases with stimulation temperature.

The band tail width (E_B) is an important parameter since it constrains the thermal lifetime of IR trap. It is particularly important for applications in thermochronometry using feldspar (e.g. Guralnik et al., 2015; King et al., 2016a,b etc), where it is important to know the exact characteristics and role of the band tail states in the thermal detrapping process. However, to date there is no routine and reliable method of mapping band tail states in feldspar. This article is an attempt towards fulfilling this gap.

4.3 Samples and experimental details

Six museum and sedimentary feldspar samples (alkali and plagioclase feldspars) were used in this study. The concentrations of K, Na and Ca were estimated using X-ray fluorescence spectroscopy (XRF) attachment in the Risø TL/OSL reader, and the Mn concentration was measured using the ICP-MS (see Table 4.1). The grain size used in the present studies was in the range of 90–180 μm, whereas R28 was a single crystal 2×2×2 mm size. R28 has been previously used by Poolton et al. (1995, 2009), Kars et al. (2013) and Anderson et al. (2012). Poolton et al. (2009) used this sample for measurement of band tail states; hence, it serves as a reference sample for our study. Sample R58 is the same as that measured by Prasad et al., (2016); note that the K, Na, Ca concentrations presented here using the XRF are slightly different from those measured using the ICP-MS in their paper. This could represent a sub-sample variability in the major cation concentrations.

Table 4.1: List of samples, their bulk composition as determined by XRF and Mn content evaluated using ICP-MS. S represents feldspars of sedimentary origin, and M represents museum single crystal samples.

Sample Code	Type of Feldspar	Provenance	K	Na	Ca	Mn (ng/g)
R28	M	Switzerland	0.95	0.05	0	not measured
R47	S	China	0.85	0.12	0.03	3.31
R57	M	u/k	0.43	0.53	0.04	48.11
R58	M	u/k	0.27	0.63	0.1	22.3
R64	S	Iceland	0.01	0.15	0.85	155.9
R65	NIST	u/k	0.27	0.73	0	17.47

The excitation-energy-dependent emission measurements at room temperature and 7 K were carried out using Risø station for CryOgenic LUminescence Research (COLUR) at DTU Nutech. The photoluminescence spectra were measured using Horiba Fluorolog-3 spectrofluorometer. A 450 W Xenon CW lamp with a wavelength range of approximately 370–520 nm was used for excitation, with the specific wavelengths selected using a double grating Cherny-Turner excitation monochromator. Emission spectra from 385–650 nm were detected with a photomultiplier

tube. All the spectra were corrected for the instrument response and photon flux. The photoluminescence lifetime in the order of millisecond - microsecond was measured using a pulsed Xe lamp and a multi-channel analyser. The specific wavelengths of the excitation pulse were selected with an excitation monochromator, while emission wavelength was selected with the emission monochromator in front of the PMT detector. The integration time for the data collection was 100 ms, and the initial delay of the system was 0.05 ms; all the measurements used flash counts of 100 to improve counting statistics. The photoluminescence lifetime in the order of nanosecond was measured with the time -correlated single photon counting (TCSPC) system; excitation source was a nanoLED of wavelength 374 nm ($\sim 3.32\,\mathrm{eV}$) operated at 1 MHz repetition rate.

4.4 Results

To demonstrate the effect of band tail states on electron mobility, we show here temperature-dependent IRSL excitation spectrum (Figure 4.1). The data were measured on sample R28 after 2 hours of X-ray irradiation; the excitation wavelength was selected with a monochromator from the 20 W halogen lamp and the detection of the IRSL signal was achieved using a 5 mm thick U340 filter in front of the PMT. There is an increase in the IRSL signal as the temperature is raised from 7 K to 295 K due to thermal activation of detrapped electrons within the band tail states; these results confirm the results of Poolton et al. (2009). Furthermore, there is a systematic blue shift in the spectra with a decrease in temperature, which is likely due to the increased crystal field effect because of thermal contraction (Varshni, 1967).

Figure 4.2(a) shows the excitation-energy-dependent PL emission spectra from sample R47. The excitation energy was varied from 3.02 eV (410 nm) to 2.38 eV (520 nm) in the increments of 10 nm. Figure 4.2(b) shows the normalised data from Figure 4.2(a). These emission spectra show a strong red edge effect; as we decrease the excitation energy there is a decrease in the emission peak energy and the net intensity of the PL emission. Figure 4.2(c) shows log (PL intensity) as a function of the excitation energy following Prasad et al. (2016); it assumes that $\mathrm{PL(E)} \propto \mathrm{(E)}$, and n=1, in Equation 4.1. The data show two discrete linear trends with the slopes of $2.73\,\mathrm{eV}^{-1}$ in the excitation range of 2.38 to 3.32 eV and $1.54\,\mathrm{eV}^{-1}$ in the range 2.63 to 3.02 eV. The emission peak energy varies

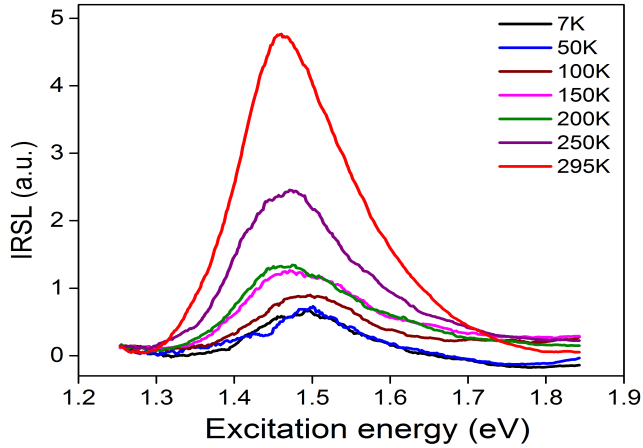

Figure 4.1: Temperature dependent IRSL stimulation spectra for R28 after 2 hours of X-ray irradiation at 7 K. The IRSL was detected via a PMT with 5 mm U340 filter, and excitation energy was varied from 1.25- 1.85 eV using a 20 W Halogen lamp

linearly with the excitation energy (Figure 4.2(d)). These data suggest that the excited levels giving rise to the PL distribution have a monotonic, exponential distribution of the density of states.

To verify if these results are universal, we investigated this phenomenon in our other samples from the alkali and plagioclase series. The results are summaries in Figure 4.3 (R57 - Na feldspar), Figure 4.4 (R 58 - Na feldspar), Figure 4.5(R64 – plagioclase feldspar), Figure 4.6 (R65 - NIST sodium feldspar) and Figure 4.7 (R28 – K feldspar). We observe that the same behaviour as the above in all the samples; the main difference is in the rate of the exponential rise of the density of states. The exponential rate for R57 is $3.18\,\mathrm{eV}^{-1}$ (Figure 4.3 (c)), R58 - $3.05\,\mathrm{eV}^{-1}$ (Figure 4.4(c)), R64 - $2.97\,\mathrm{eV}^{-1}$ (Figure 4.5(c)), R65 - $2.1\,\mathrm{eV}^{-1}$ (Figure 4.6(c)), and R28 – $3.45\,\mathrm{eV}^{-1}$ (Figure 4.7(c)). The sample R57 and R28 show a dominantly single exponential trend with a possible hint of a minor second exponential below 2.64 eV excitation energy, whereas the samples R58, R64 and R65 show a single exponential distribution of PL intensities as a function of the excitation energy. All these samples show a linear dependence of the Stokes shifted emission energy on the excitation energy, with the slopes ranging from $\sim 0.5 - 0.7$ (Figures 4.2(d) to 4.7(d)); these suggest that there is a constant increment change in the peak emission per unit change in the excitation energy.

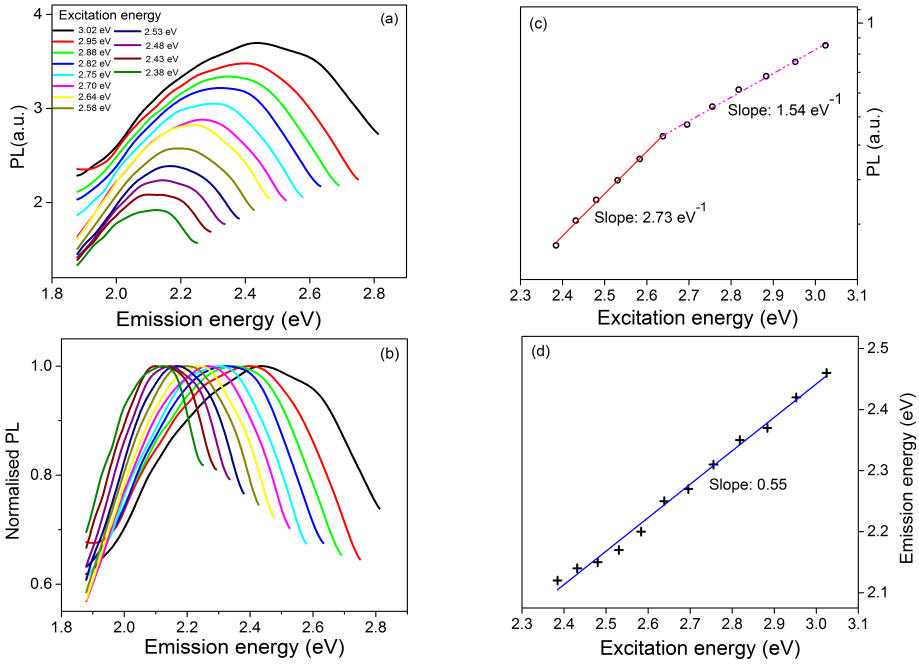

Figure 4.2: Dependence of PL emission on the excitation energy in sample R47. (a) Excitation-energy-dependent emission spectra, (b) Normalized curves (by peak intensity) of the data in (a), (c) $\log_{10}$ of the PL peak area plotted as a function of excitation energy. The slopes calculated using the natural Log of the PL data are also shown, (d) the emission peak of PL spectra plotted as a function of the corresponding excitation energy, demonstrating the red edge effect.

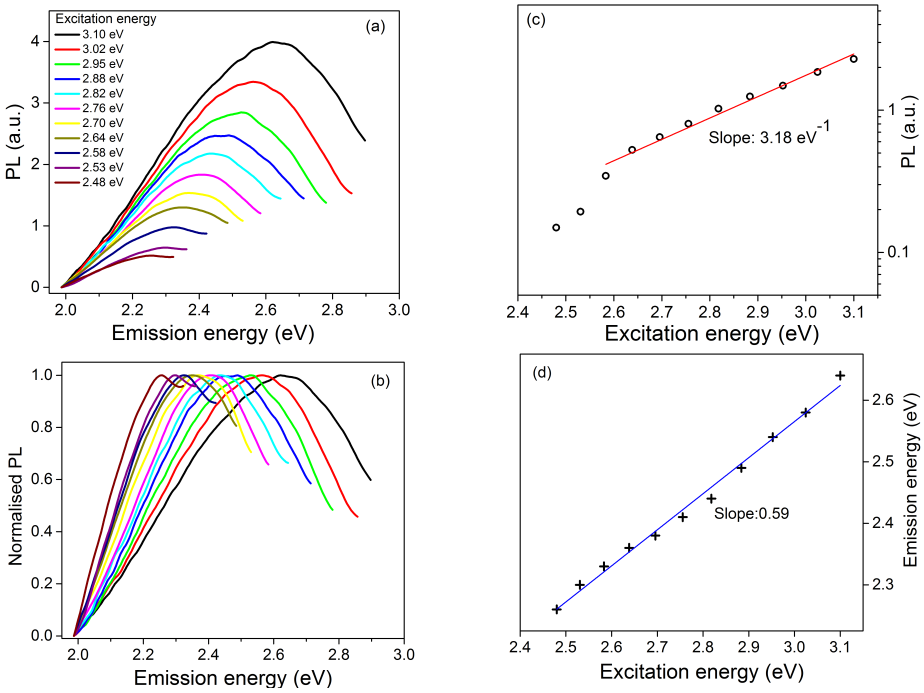

Figure 4.3: Dependence of PL emission on the excitation energy in sample R57. a) Excitation-energy-dependent emission spectra. (b) Normalized curves (by peak intensity) of the data in (a). (c) $\log_{10}$ of the PL peak area plotted as a function of excitation energy. The slopes calculated using the natural Log of the PL data are also shown, (d) The emission peak of PL spectra plotted as a function of the corresponding excitation energy, demonstrating the red edge effect.

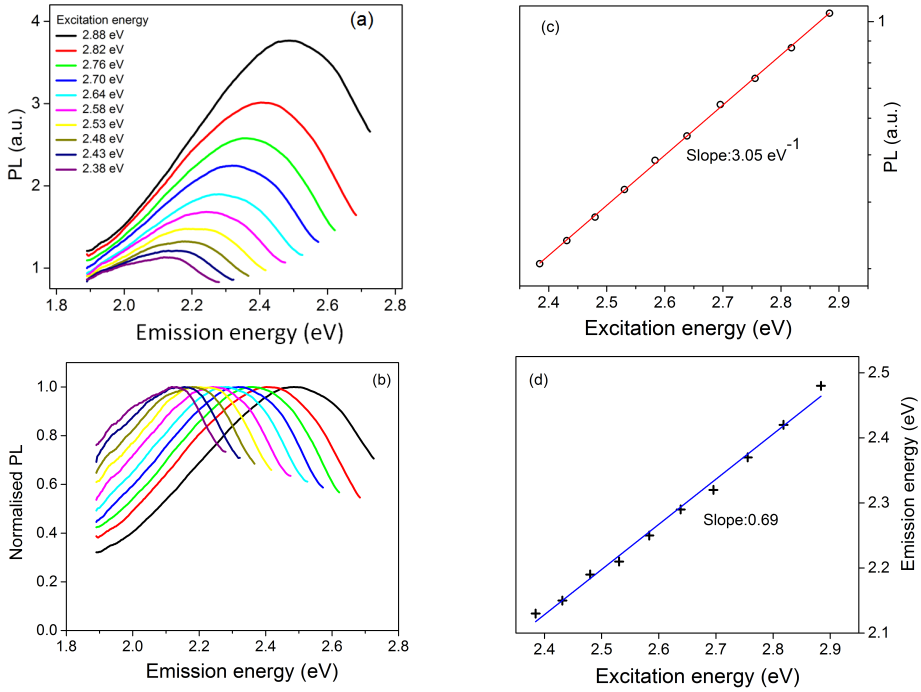

Figure 4.4: Dependence of PL emission on the excitation energy in sample R58. a) Excitation-energy-dependent emission spectra. (b) Normalized curves (by peak intensity) of the data in (a), (c) $\log_{10}$ of the PL peak area plotted as a function of excitation energy. The slopes calculated using the natural Log of the PL data are also shown. (d) the emission peak of PL spectra plotted as a function of the corresponding excitation energy, demonstrating the red edge effect.

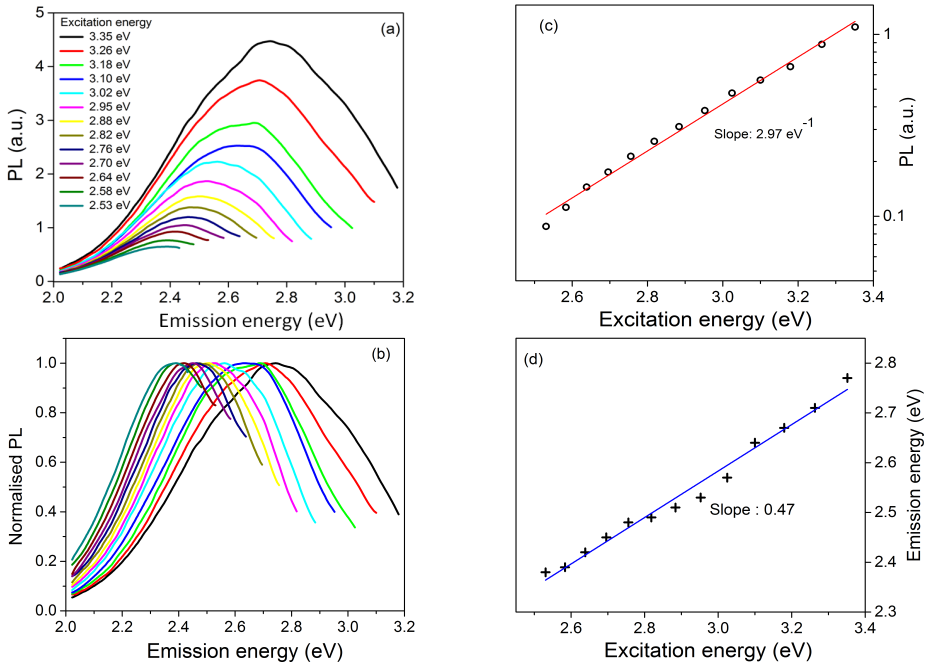

Figure 4.5: Dependence of PL emission on the excitation energy in sample R64. a) Excitation-energy- dependent emission spectra, (b) Normalized curves (by peak intensity) of the data in (a), (c) $\log_{10}$ of the PL peak area plotted as a function of excitation energy. The slopes calculated using the natural Log of the PL data are also shown, (d) the emission peak of PL spectra plotted as a function of the corresponding excitation energy, demonstrating the red edge effect.

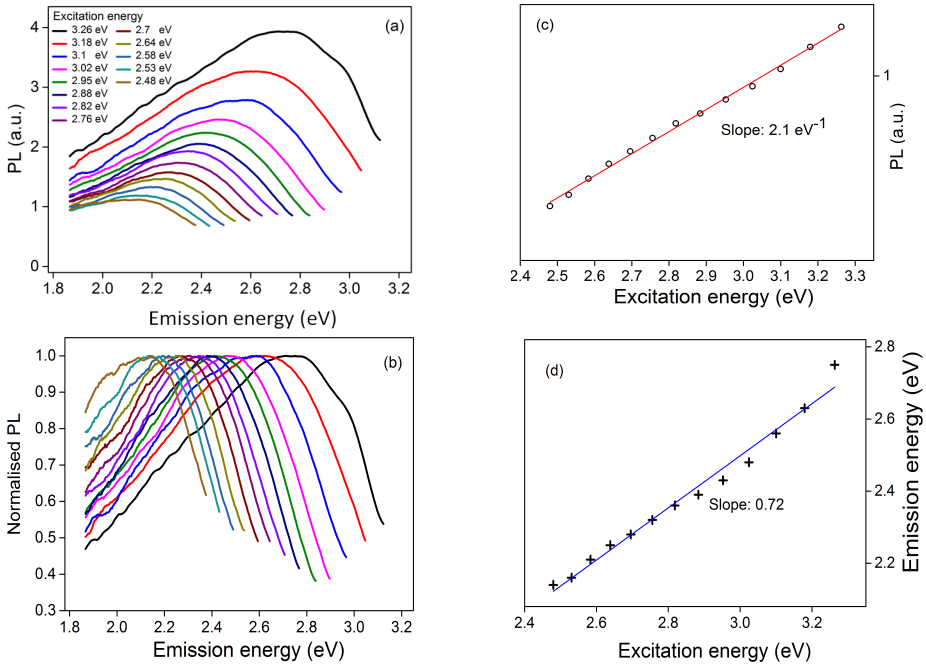

Figure 4.6: Dependence of PL emission on the excitation energy in sample R65. a) Excitation-energy- dependent emission spectra, (b) Normalized curves (by peak intensity) of the data in (a), (c) $\log_{10}$ of the PL peak area plotted as a function of excitation energy. The slopes calculated using the natural Log of the PL data are also shown, (d) the emission peak of PL spectra plotted as a function of the corresponding excitation energy, demonstrating the red edge effect.

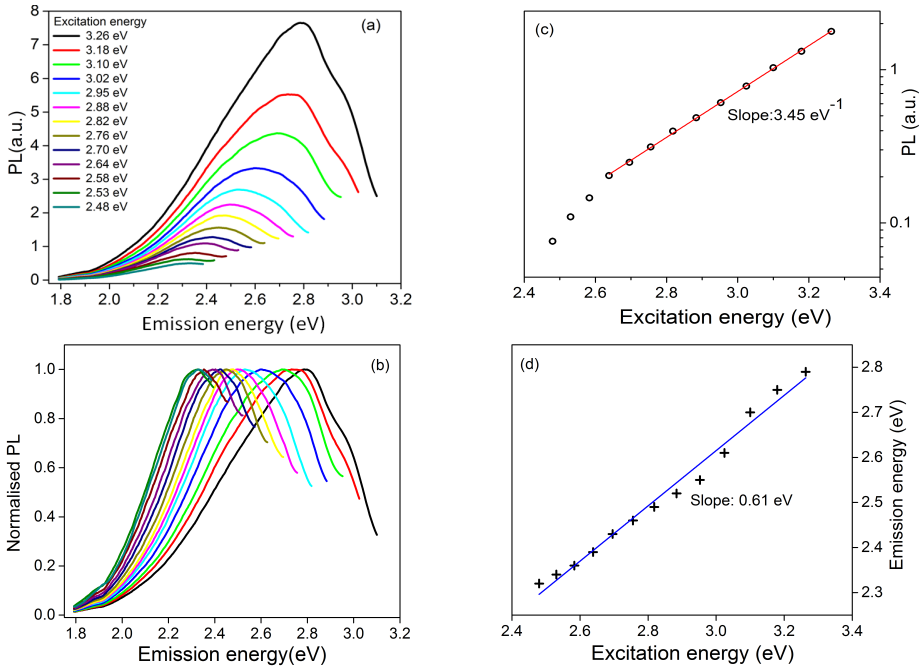

Figure 4.7: Dependence of PL emission on the excitation energy in sample R28. a) Excitation-energy- dependent emission spectra, (b) Normalized curves (by peak intensity) of the data in (a), (c) $\log_{10}$ of the PL peak area plotted as a function of excitation energy. The slopes calculated using the natural Log of the PL data are also shown, (d) the emission peak of PL spectra plotted as a function of the corresponding excitation energy, demonstrating the red edge effect.

We further investigated on the details of the red edge effect in our reference sample R28 at 7 K. There was a significant enhancement in the intensity for each emission at 7 K compared to 295 K (Figure 4.8(b)). The normalised emission spectra are shown for three different excitation energies (marked with arrows; Figure 4.8(a). There is a broadening of the emission peak on the low energy side and a tendency for a minor red shift at 7 K. The area under the PL curve for the 7 K also shows an exponential trend, however the rate is 2.19 eV^{-1} at 7 K compared to 3.46 eV^{-1} at 295 K (Figure 4.8(b)).

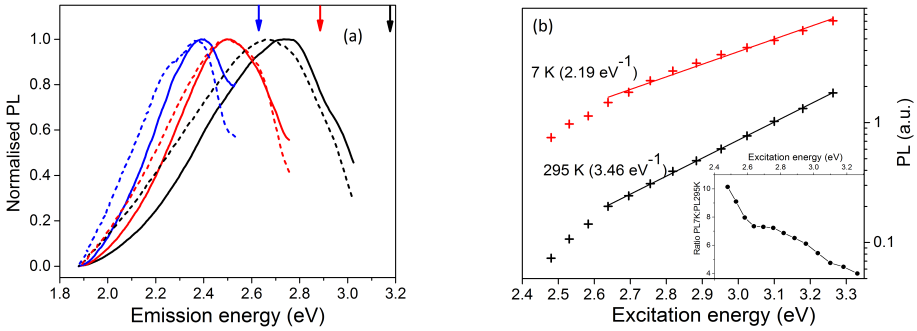

Figure 4.8: (a) The emission spectra of R28 at 7 K and 295 K represented by dashed and solid line, respectively. The emission spectra are obtained using excitation energy with 3.18 eV (black), 2.88 eV (red) and 2.64 eV (blue), indicated by the same coloured downward facing arrows. (b) comparison of the area under the emission peak for 7 Kand 295 K data; the inset shows the ratio of PL area for 7 Kand 295 K.

For sample R28, we also measured the fluorescence and phosphorescence kinetics of the PL emission using pulsed nanoLED and Xe lamp, respectively. The fluorescence decay data was measured using 3.32 eV excitation using the TCSPC facility at 295 K. The detection window was systematically varied from 440 nm to 570 nm in the step of 10 nm in different experiments. The data are shown in Figure 4.9(a) and were fitted to a sum of two exponentials (Table 4.2). Figure 4.9(b) shows the summary of the two lifetimes as a function of emission energy. Although the curves look very similar (Figure 4.9(a)), there appears to be a systematic decrease in the lifetime of the dominant slower component from 5.3 ns to 4.2 ns as the energy of the emission decreases from 2.82 to 2.18 eV. The faster lifetime remains constant at about 800 ps from 2.2 to 2.6 eV and then decreases systematically with excitation energy to a value of 500 ps at 2.8 eV.

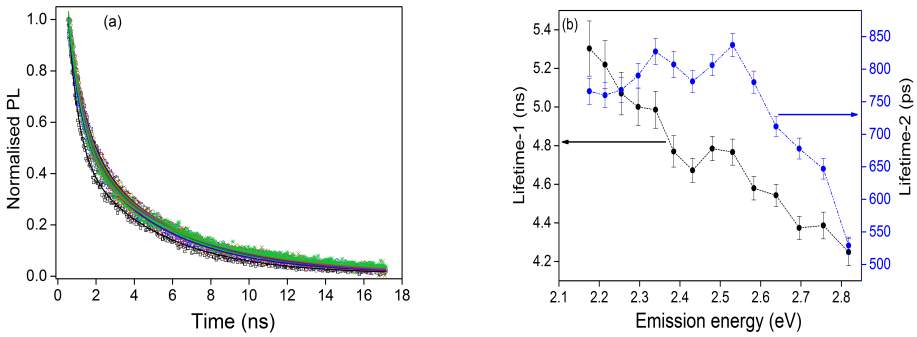

Figure 4.9: (a)Fluorescence decay at 295 K measured using 3.32 nanoLED excitation, and detection at different wavelengths scanning the PL emission peak in the increments of 10 nm. The data are analysed with a sum of two exponential functions. (b) Lifetimes derived from (a) as a function of emission energy. These data are summarised in Table 4.2.

Figure 4.10 shows the phosphorescence decay using excitation at 3.26 eV from the pulsed Xe lamp at 7 K and 295 K. The detection monitored for four different emission windows are shown in Figure 4.10 4.10(a)2.82 eV, 4.10(b)2.58 eV, 4.10(c)2.38 eV and 4.10(d)2.21 eV. The data were fitted to a linear combination of two exponential decay functions; the derived lifetimes are summarised in Table 4.2. Visual inspection, shows that the phosphorescence decay at 7 K is similar for all the emission windows, however, it varies significantly at 295 K. There is an increase in the phosphorescence decay rate with a decrease in the emission energy; the phosphorescence decay at 295 K is similar to that at 7 K for 2.82 eV emission, whereas it is much faster than 7 K data for 2.28 and 2.21 eV emission. An intermediate scenario can be seen in the 2.53 eV emission.

In the next section we explain our results through a new model for red edge effect.

4.5 Discussion

A comparative summary of all the steady state PL results is shown in Figure 4.11, and summarised in Table 4.3. It is clear that the excitation-energy-dependent emission spectra (the giant 'red edge effect') is prevalent in our feldspar samples comprising different mineralogies, therefore, it pertinent to explore the physical mechanism behind the effect. Here we first present the mechanism of the red edge effect as inferred from our

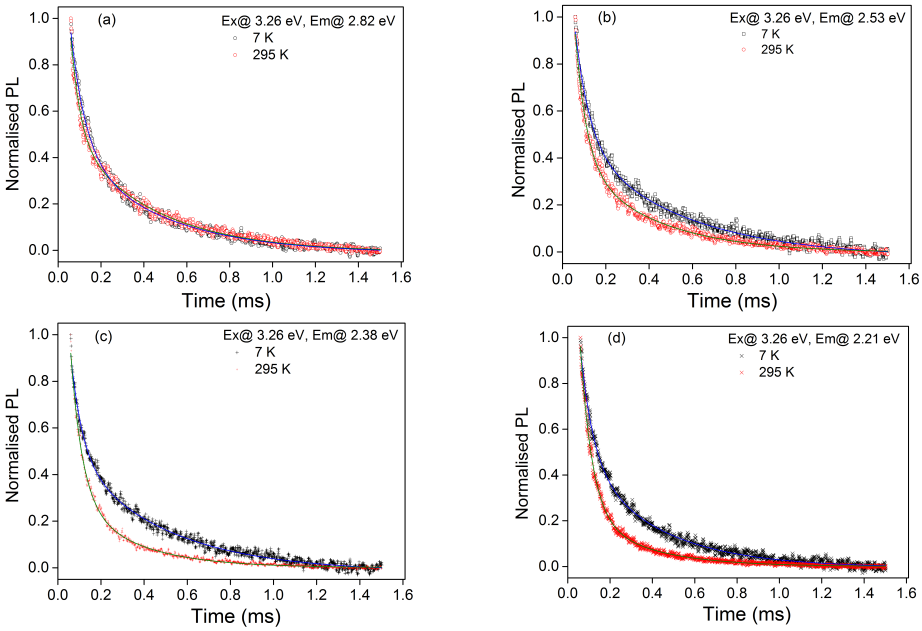

Figure 4.10: Phosphorescence decay measured using 3.26 eV excitation selected from a pulsed Xe lamp. The phosphorescence data are plotted for 7 Kand 295 K, using different emission windows (a) 2.82 eV (b) 2.53 eV (c) 2.38 eV (d) 2.21 eV. The data were fitted with sum of two exponentials and lifetimes are surmised in Table 4.2.

Table 4.2: Summary of lifetime data fitting parameters for the sample R28

Emission Energy (eV)	295 K				7 K	
	τ_1(ns)	τ_2(ps)	τ_1(ms)	$\tau_2(\mu s)$	τ_1(ms)	$\tau_2(\mu s)$
2.82	4.25 ± 0.07	529 ± 13	0.39 ± 0.01	45 ± 1	0.42 ± 0.01	71 ± 2
2.76	4.39 ± 0.07	647 ± 15				
2.70	4.37 ± 0.06	677 ± 16				
2.64	4.54 ± 0.06	711 ± 15				
2.58	4.58 ± 0.06	780 ± 17				
2.53	4.77 ± 0.06	837 ± 17	0.36 ± 0.01	52 ± 1	0.48 ± 0.02	67 ± 2
2.48	4.78 ± 0.06	806 ± 16				
2.43	4.67 ± 0.06	781 ± 17				
2.38	4.77 ± 0.08	807 ± 20	0.28 ± 0.01	54 ± 1	0.43 ± 0.01	54 ± 2
2.34	4.99 ± 0.10	827 ± 20				
2.30	5.00 ± 0.10	789 ± 19				
2.25	5.07 ± 0.11	768 ± 19				
2.21	5.22 ± 0.12	760 ± 19	0.29 ± 0.01	56 ± 1	0.36 ± 0.01	61 ± 1
2.18	5.30 ± 0.14	766 ± 20				

results, and then discuss the possible defect(s) participating in effect.

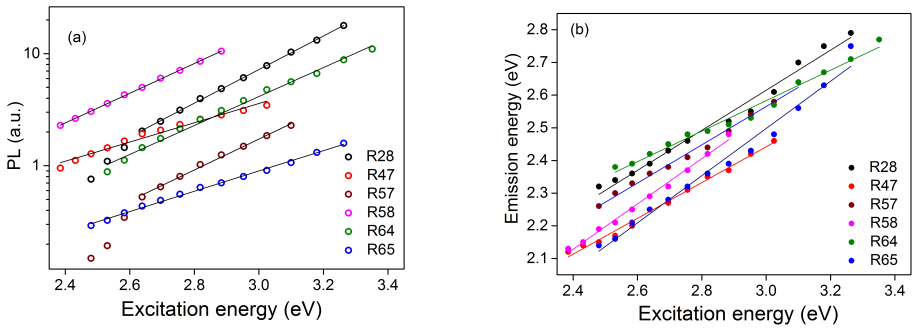

Figure 4.11: A summary of the red edge effect in all our samples. (a) Log PL area vs excitation energy, (b) PL emission peak energy vs. excitation energy.

Table 4.3: Sample dependent band tail energy

Sample	Slope Ex. vs Em.	Slope (1/eV)	Band tail energy (eV)
R28	0.61	3.45	0.29
R47	0.55	2.73 and 1.54	0.37 and 0.65
R57	0.59	3.18	0.31
R58	0.69	3.05	0.33
R64	0.47	2.97	0.34
R65	0.72	2.09	0.48

Luminescence generation mechanism The band gap of the feldspar is around 7.7 eV, and our excitation energy ranging from 2.38- 3.26 eV leads to PL emission in the well-known orange-green band. This emission has been widely studied using cathodoluminescence, radioluminescence and X-ray excited optical luminescence (e.g. Krbetschek et al., 1997; Can et al., 2011; Prasad et al., 2016). The rather broad emission peak (up to 1 eV in some samples for the highest energy excitation), as well as the magnitude of the red shift ($\sim$ 0.05 eV; see Figure 4.11) upon decreasing the excitation wavelength suggests that this emission arises from a multiplicity of radiative transition levels. These characteristics indicate

that there exists a distribution of zero-phonon energies of the defect contributing to the PL spectra (Tsang et al., 1979, Robertson, 1996, Monroe, 1985); the broad PL peak then results from inhomogeneous broadening due to slightly different host environment around this defect. Depending on the excitation threshold, only a subpopulation from the ensemble of this defect can be excited and thereafter relaxed radiatively. However, our data also show that the integrated PL intensity increases exponentially with the excitation energy in all our samples (Figures 4.2 (a and c) to 4.7 (a and c); this suggests that there exists an exponentially distributed continuum of excitation levels, which is available to the defect. Based on the data on R58 sample, Prasad et al. (2016) suggested that the exponential increase in PL intensity either maps the DOS of the sub-conduction band tail states, or it arises from a charge transfer band originating from defect clustering. In this article we have tested 5 more samples and we observe the exponential trend of PL intensity with excitation energy in all the samples. Our data from the sample R28 is particularly notable as this sample was also used by Poolton et al., (2009) for direct mapping of the band tail states employing a combination of X-ray irradiation (to fill these states) and excitation spectroscopy at 10 K. These authors derived a band tail width of 0.54 eV in R28 and concluded that this value was consistent with their independent measurement using synchrotron radiation. The slope of our exponential data for R28 at 7 K (similar to 10 K used by Poolton et al. (2009) is 2.19 eV^{-1} as shown in Figure 4.8 (b); the inverse of this value following Equation (4.1) is 0.46 eV, which is comparable to the estimate of the width of the band tail by Poolton et al. (2009). Thus, we infer that the red edge effect is indeed mapping the continuum of the band tail states in our sample, at least at the higher excitation energies; there is an exponential increase in the probability of photoionisation (and, thus, PL efficiency) because of the exponential DOS of the band tail states. The emission on the other hand occurs via hopping transport of the detrapped electrons towards the higher electronic levels of the defect embedded within the band tail states. Subsequent excited state relaxation results in photon emission corresponding to the energy difference between the excited and the ground state. The overall peak shape of the emission likely arises due to a quasi-equilibrium distribution of electron occupancy in the band tails resulting from a combination of i) the exponential DOS of the band tails, ii) the peak (Poisson or Gaussian) distribution of the zero phonon transition levels of the defect, and iii) the

temperature dependent Boltzmann's distribution. The defect levels near the band edge have been observed to result in a strong continuum of states in heavily doped semiconductors (John et al., 1987; Eliseev, 2003).

As shown in Figure 4.12, our model of the red edge effects includes the following steps: 1. Photo-ionisation of an ensemble (distribution) of defect, leading to a transition of ground state electrons to the band tail states.

2. Hopping transport leading to occupancy of higher electronic states of the defect embedded within the band tail states. The hopping length and thermal activation of hopping are dependent on the DOS, which is a function of the band tail energy; larger for lower band tail states and smaller for the higher states (Jain and Ankjærgaard, 2011; Esser, 1987).

3. Relaxation from the excited state to the ground state of the defect resulting in the orange-green emission band. The red edge effect is observed since there is a continuum of the excitation and emission energies, and the PL emission primarily occurs from states that are below the excitation energy (Figure 4.12).

This model potentially also explains the deviation from the exponential trend at low energies observed in some samples. At low energies, the low DOS of the band tails is comparable with the DOS of the excited states (Figure 4.12); thus, the excitation process will be a combination of inter-defect excitation and defect-to-band tail ionisation. Note that at these low excitation energies, only a very small sub area of the main peak is sampled, and the PL intensity is smaller than that expected from the Band tail model (linear fit to the high-energy data). A linear change in the emission peak with excitation energy (Figure 4.11(b) is possibly a result of the occupancy function, the exact details of which require further investigations.

The low temperature data confirm the model. The fact that there is no significant reduction in the peak width at low temperature also confirms an inhomogeneous broadening mechanism, i.e., the PL peak arises from a continuum of the defect's zero phonon energy levels. Furthermore, at 7 K it is observed that the low energy side of the PL peak is widened (Figure 4.8(a), suggesting that the electron occupancy is biased towards the lower energy band tail states following the Boltzmann's distribution.

Luminescence decay measurements Time resolved luminescence could give information on relaxation and transport time scales in feldspar (Jain

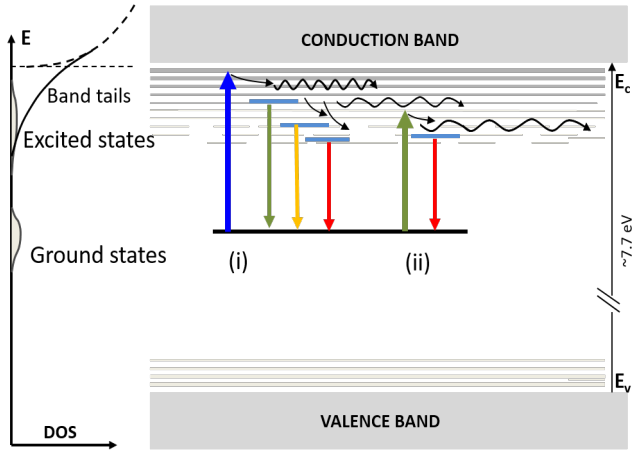

Figure 4.12: A conceptual model of the red edge effect in feldspar. E – energy, DOS-density of states, Upward arrow – optical excitation, downward arrow – radiative relaxation. Optical excitation leads to defect ionisation by transition of electrons to the band tail states. Subsequent thermalisation and hopping transport leads to the excited state of the defect, followed by relaxation and PL emission. The wiggles in the band tail states represent the hopping process. A continuum of excitations and emission energies exists in the red edge effect; cases (i) and (ii) are shown to represent relatively high and low energy cases, respectively. Importantly, a decrease in the excitation (case (ii)) leads to a simultaneous decrease in the emission energy, and any PL produced using a certain excitation energy is a subset of the PL produced from a relatively higher energy.

and Ankjærgaard, 2011). In our data, the fluorescence lifetimes are essentially invariant with the emission energy, likely representing the fundamental transition (possibly phonon mediated) from the excited to the ground state of the defect (Figure 4.9). The minor (1 ns) but systematic variation from the high to the low emission energy possibly reflects the interaction between the excited state and the band tail states. It may be argued that disordered band tail states act like a glassy matrix around the defect; thus a limited dipole reorganisation in a rigid matrix could give rise to the decrease in the lifetime for lower energy; this effect is similar to the classic red edge effect observed in polar solvents (see Demchenko, 2002). Alternatively, the longer lifetime could also reflect a longer transport time (long range hopping) to the lower energy levels within the band tail states (Jain and Ankjærgaard, 2011); however, 1 ns lifetime difference may be too small to account for multiple hopping steps. Hopping times in feldspars are likely to be in the range of microseconds (Jain and Ankjærgaard, 2011; Morthekai et al., 2012)

The phosphorescence data show lifetime components in the microsecond and millisecond time scales (Figure 4.10). These lifetimes can be attributed to the hopping mechanism suggested in our model (Figure 4.12). We expect that sample temperature should not affect the transport (hopping) times for the high energy band tail states, since a large DOS leads to large wave-function overlap. Our data confirm this expectation; there is no significant difference between 7 K and 295 K phosphorescence decay in case of the 2.82 eV emission (Figure 4.10a). On the other hand, for low energy emissions thermally assisted hopping should be important because of low wave-function overlap between the states. As expected, there is much faster decay of the PL as the temperature is raised from 7 K to 295 K for the 2.28 and 2.21 eV emissions (Figure 4.10 c, d) confirming that the lower band tail states empty faster due to the thermal effect. The 2.53 eV emission shows intermediate emptying rate (Figure 4.10 b) at room temperature.

Thermal Quenching A reduction in the PL intensity at room temperature reflects thermal quenching (Figure 4.8). This quenching is attributed to the phonon relaxation within the defect. Interestingly, thermal quenching has an apparent dependence on the excitation energy (Figure 4.8(b), inset); greater quenching for low excitation energies. It is observed that the slope of the PL intensity vs. excitation energy is differ-

ent for the room temperature and the low temperature data. The slope change at low temperature in Figure 4.8(b) suggests that the band tail width (inverse of slopes) is higher at 7 K than at the room temperature in the R28 sample. This increase in the band tail width could possibly be an effect of increased crystal field at lower temperatures. But this effect is not universal; Prasad et al., (2016) did not observe a change in the slope between 7 K and 295 K data in the R58 sample. Further mineralogical investigations may be necessary, since feldspar could exist as mineralogically exolved sub-phases on a nanometer to micrometer scale within a single crystal.

Luminescent defect In the above discussion we have assumed that an unknown defect gives rise to the giant 'red edge effect' upon interaction with the band tail states. It is generally assumed that the green – orange band in feldspar is due to the Mn^{2+}, where the Mn^{2+} luminescence centre occupies the Ca sites (Geake et al., 1977). The Mn content in our samples in shown in Table 4.1. We did not observe any correlation between the emission intensity and the Mn content in our six samples. Furthermore, the typical orange emission in Mn^{2+} takes place via the d^5 spin-forbidden transition ($^4T_1 \rightarrow {}^6A_1$); thus, the relaxation lifetimes are expected to be in millisecond range (e.g. Shi et al., 2010). Even in disordered glasses, which could be considered analogous to our situation (the defect state embedded within the band tail states), Mn^{2+} lifetimes have been observed to be on the milliseconds time scales (Zotov et al., 2002). Given these considerations, our lifetime data in the picosecond to microsecond range, suggest that a simple Mn^{2+} emission model cannot be applied to feldspars.

There could be other possible candidates for the luminescent defect. It has been demonstrated that surface states may play an important role in the red edge effect in quantum dots (Li et al., 2014; Gan et al., 2016). Fitting et al., (2009) demonstrated the appearance of the green-yellow band in silicon nanoclusters ($\sim$ 2 nm diameter); they attributed these to the oxygen deficiency centers. It is not inconceivable that the red edge effect may be arising from the alteration sites in Si tetrahedra, which are possibility more dominant at the crystal surfaces. The determination of the exact defect states requires further investigations.

Implications of this research: Band tail states play an important role in the thermal stability of trapped charge in feldspar, there is no easy, straightforward way to make a direct, routine characterisation for the samples used in optical dating. The methods used by Poolton et al., (2009) require advanced instrumentation with cryogenic ionising irradiation and luminescence spectroscopy facilities, which are not available in most laboratories. Furthermore, low temperature results may not apply to dating scenario, which typically involves $> 295\,\mathrm{K}$, because of the crystal field effect. We demonstrate here that the peak intensity of orange-green PL emission in feldspar is linked to the density of states, i.e. $\mathrm{I(E)} \propto \rho(\mathrm{E})$. This method of mapping band tail states in feldspar can be performed routinely in most laboratories to aid estimation of thermal stability of the IR trap (King et al., 2016).

To our knowledge, this paper documents the first observation of the red edge effect in macro crystalline materials. The defect and band tail state interaction model proposed here may be worth considering other solid materials exhibiting the red edge effect. For example band tail states are also known in quantum dots of different compositions (e.g., ZnO: Hoye et al., 2014, Kim et al. 2002; Graphene oxide: Liu et al. 2013). It is worth exploring whether the band tail model proposed here could solve the long-standing debate on the origin of the red edge effect in carbon nanodots. Finally, an understanding of the red edge effect and defect characterisation will help explore the use of the feldspar as tunable light sources.

4.6 Conclusion

We demonstrate the excitation-energy-dependent luminescence emission (giant red edge effect) in a wide bandgap aluminosilicate-feldspar. We conclude that this effect arises from interaction between a defect state and the band tail density in feldspar. We also conclude that the orange-green emission does not arise from Mn^{2+} as is commonly believed. Based on our new model of the giant red edge effect, we propose a simple, robust method for the measurement of band tail width in feldspar; an issue of immense relevance for its application in geochronometry and thermochronometry. Our model deserves further attention to test if it can also explain the red edge effect in carbon quantum dots.

4.7 Acknowledgement

It is our pleasure to thank Dr. Per Roos for ICP-MS measurements, and Ms. Louise Maria Helsted for the sample preparation.

Bibliography

[1] Andersen, M. T., Jain, M., Tidemand-Lichtenberg, P. (2012). Red-IR stimulated luminescence in K-feldspar: Single or multiple trap origin? Journal of Applied Physics, 112(4), 043507.

[2] Arnold, L. J., Demuro, M., Parés, J. M., Pérez-González, A., Arsuaga, J. L., de Castro, J. M. B., & Carbonell, E. (2015). Evaluating the suitability of extended-range luminescence dating techniques over early and Middle Pleistocene timescales: published datasets and case studies from Atapuerca, Spain. Quaternary International, 389, 167-190.

[3] Buylaert, J. P., Murray, A. S., Thomsen, K. J., Jain, M. (2009) Testing the potential of an elevated temperature IRSL signal from K-feldspar. Radiation Measurements 44, 560–565.

[4] Buylaert, J.P., Jain, M., Murray, A.S., Thomsen, K.J., Thiel, C., Sohbati, R., (2012). A robust feldspar luminescence dating method for Middle and Late Pleistocene sediments. Boreas 41, 435–451.

[5] Cushing, S. K., Li, M., Huang, F., & Wu, N. (2013). Origin of strong excitation wavelength dependent fluorescence of graphene oxide. ACS nano, 8(1), 1002-1013.

[6] Can, N., Garcia-Guinea, J., Kibar, R., Çetin, A., Ayvacıklı, M., & Townsend, P. D. (2011). Radioluminescence and thermoluminescence of albite at low temperature. Radiation Measurements, 46(8), 655-663.

[7] Demchenko, A. P. (2002). The red-edge effects: 30 years of exploration. Luminescence, 17(1), 19-42.

[8] Duller, G. A. T. (1997). Behavioural studies of stimulated luminescence from feldspars. Radiation Measurements, 27(5), 663-694.

[9] Eliseev, P. G. (2003). The red σ^2/kT spectral shift in partially disordered semiconductors. Journal of applied physics, 93(9), 5404-5415.

[10] Esser, B. (1987). On the theory of band tail relaxation in disordered systems. Journal of Non-Crystalline Solids, 97, 137-140.

[11] Fitting, H. J., Kourkoutis, L., Salh, R., Zamoryanskaya, M. V., & Schmidt, B. (2010). Silicon nanocluster aggregation in SiO2: Si layers. physica status solidi (a), 207(1), 117-123.

[12] Gan, Z., Xu, H., & Hao, Y. (2016). Mechanism for excitation-dependent photoluminescence from graphene quantum dots and other graphene oxide derivates: consensus, debates and challenges. Nanoscale, 8(15), 7794-7807.

[13] Galley, W. C., & Purkey, R. M. (1970). Role of heterogeneity of the solvation site in electronic spectra in solution. Proceedings of the National Academy of Sciences, 67(3), 1116-1121.

[14] Geake, J. E., Walker, G., Telfer, D. J., Mills, A. A. (1977). The Cause and Significance of Luminescence in Lunar Plagioclase. Philosophical Transactions of the Royal Society A: Mathematical, Physical and Engineering Sciences, 285, 403-405.

[15] Guralnik, B., Jain, M., Herman, F., Ankjærgaard, C., Murray, A. S., Valla, P. G., ... & Kook, M. (2015). OSL-thermochronometry of feldspar from the KTB borehole, Germany. Earth and Planetary Science Letters, 423, 232-243.

[16] Hao, Y., Gan, Z., Xu, J., Wu, X., & Chu, P. K. (2014). Poly (ethylene glycol)/carbon quantum dot composite solid films exhibiting intense and tunable blue-red emission. Applied Surface Science, 311, 490-497.

[17] Hoye, R. L., Ehrler, B., Bohm, M. L., Munoz-Rojas, D., Altamimi, R. M., Alyamani, A. Y., ... & Friend, R. H. (2014). Improved Open-Circuit Voltage in ZnO-PbSe Quantum Dot Solar Cells by Understanding and Reducing Losses Arising from the ZnO Conduction Band Tail. Advanced energy materials, 4(8).

[18] Huntley, D. J. and Lamothe, M. (2001) Ubiquity of anomalous fading in K-feldspars and the measurement and correction for it in optical dating. Can. J. Earth Sci. 38 1093–106

[19] Hütt, G., Jaek, I., Tchonka, J., (1988). Optical dating: K-feldspars optical response stimulation spectra. Quaternary Science Reviews, 7, 381–385.

[20] Henderson, B., & Imbusch, G. F. (2006). Optical spectroscopy of inorganic solids (Vol. 44). Oxford University Press.Chicago

[21] Jain, M., (2014). Feldspar, Infrared-Stimulated Luminescence. Encyclopaedia of Scientific Dating Methods, pages: 1-8.

[22] Jain, M., & Ankjærgaard, C. (2011). Towards a non-fading signal in feldspar: insight into charge transport and tunnelling from time-resolved optically stimulated luminescence. Radiation Measurements, 46(3), 292-309.

[23] Jain, M., Guralnik, B., Andersen, M. T. (2012) Stimulated luminescence emission from localized recombination in randomly distributed defects. Journal of physics: Condensed matter 24, 385402.

[24] Jain, M., Buylaert, J. P., Thomsen, K. J., Murray, A. S., (2015a). Further investigations on 'non-fading' in K-Feldspar. Quaternary International, 362, 3–7

[25] John, S. (1987). Strong localization of photons in certain disordered dielectric superlattices. Physical review letters, 58(23), 2486.

[26] King, G. E., Guralnik, B., Valla, P. G., & Herman, F. (2016a). Trapped-charge thermochronometry and thermometry: A status review. Chemical Geology, 446, 3-17.

[27] King, G. E., Herman, F., & Guralnik, B. (2016b). Northward migration of the eastern Himalayan syntaxis revealed by OSL thermochronometry. Science, 353(6301), 800-804.

[28] Kars, R. H., Wallinga, J., & Cohen, K. M. (2008). A new approach towards anomalous fading correction for feldspar IRSL dating-tests on samples in field saturation. Radiation Measurements, 43(2), 786-790.

[29] Kars, R. H., Poolton, N., Jain, M., Ankjærgaard, C., Dorenbos, P., Wallinga, J., (2013). On the trap depth of the IR-sensitive trap in Na- and K-feldspar. Radiation Measurements, 59, 103-113

[30] Kim, S. W., Fujita, S., & Fujita, S. (2002). Self-organized ZnO quantum dots on SiO 2/Si substrates by metalorganic chemical vapor deposition. Applied physics letters, 81(26), 5036-5038.

[31] Kasha, M. (1950). Characterization of electronic transitions in complex molecules. Discussions of the Faraday society, 9, 14-19.

[32] Krbetschek, M. R., Götze, J., Dietrich, A., & Trautmann, T. (1997). Spectral information from minerals relevant for luminescence dating. Radiation Measurements, 27(5), 695-748.

[33] Li, X., Zhang, S., Kulinich, S. A., Liu, Y., & Zeng, H. (2014). Engineering surface states of carbon dots to achieve controllable luminescence for solid-luminescent composites and sensitive Be^{2+} detection. Scientific reports, 4.

[34] Liu, F., Jang, M. H., Ha, H. D., Kim, J. H., Cho, Y. H., & Seo, T. S. (2013). Facile synthetic method for pristine graphene quantum dots and graphene oxide quantum dots: origin of blue and green luminescence. Advanced Materials, 25(27), 3657-3662.

[35] Li, B., Li, S.-H., (2011). Luminescence dating of K-feldspar from sediments: a protocol without anomalous fading correction. Quat. Geochronol. 6, 468–479.

[36] Li, B., Li, S.-H., (2013). The effect of band-tail states on the thermal stability of the infrared stimulated luminescence from K-feldspar. Journal of Luminescence 136, 5-10

[37] Malins, A. E. R., Poolton, N. R. J., Quinn, F. M., Johnsen, O., & Denby, P. M. (2004). Luminescence excitation characteristics of Ca, Na and K-aluminosilicates (feldspars) in the stimulation range 5–40 eV: determination of the band-gap energies. Journal of Physics D: Applied Physics, 37(10), 1439.

[38] Morthekai, P., Thomas, J., Pandian, M. S., Balaram, V., & Singhvi, A. K. (2012). Variable range hopping mechanism in band-tail states of feldspars: A time-resolved IRSL study. Radiation Measurements, 47(9), 857-863.

[39] Murray, A.S., Buylaert, J.P., Thomsen, K. J., Jain, M., (2009). The effect of preheating on the IRSL signal from feldspar. Radiation Measurements 44 (5), 554-559.

[40] Monroe, D. (1985). Hopping in exponential band tails. Physical review letters, 54(2), 146.

[41] Niehus and R. Schwarz (2006), Thermalization and recombination in exponential band tail states. Phys. Stat. Sol. (c) 3, No. 6, 1637–1644 (2006

[42] Poolton, N. R. J., Kars, R. H., Wallinga, J., & Bos, A. J. J. (2009). Direct evidence for the participation of band-tails and excited-state tunnelling in the luminescence of irradiated feldspars. Journal of Physics: Condensed Matter, 21(48), 485505.

[43] Poolton, N. R. J., Wallinga, J., Murray, A. S., Bulur, E., & Bøtter-Jensen, L. (2002). Electrons in feldspar I: on the wavefunction of electrons trapped at simple lattice defects. Physics and Chemistry of Minerals, 29(3), 210-216

[44] Poolton, N. R. J., Bøtter-Jensen, L., & Duller, G. A. T. (1995). Thermal quenching of luminescence processes in feldspars. Radiation Measurements, 24(1), 57-66.

[45] Prasad, A. K., Lapp, T., Kook, M., & Jain, M. (2016). Probing luminescence centers in Na rich feldspar. Radiation Measurements, 90, 292-297.

[46] Pelant, I., & Valenta, J. (2012). Luminescence spectroscopy of semiconductors. Oxford University Press.

[47] Rhodes, E. J., (2011). Optically stimulated luminescence dating of sediments over the past 200,000 years. Annual Review of Earth and Planetary Sciences, 39, 461-488.

[48] Robertson, J. (1996). Recombination and photoluminescence mechanism in hydrogenated amorphous carbon. Physical Review B, 53(24), 16302.

[49] Roberts, R. G., & Lian, O. B. (2015). Dating techniques: Illuminating the past. Nature, 520(7548), 438-439.

[50] Sharma, A., Gadly, T., Gupta, A., Ballal, A., Ghosh, S. K., & Kumbhakar, M. (2016). Origin of Excitation Dependent Fluorescence in Carbon Nanodots. The Journal of Physical Chemistry Letters, 7(18), 3695-3702.

[51] Smith, J.V., (1970). Physical properties of order-disorder structures with especial reference to feldspar minerals. Lithos, 2, 3, 145-160.

[52] Sritrakool, W., Sa-Yakanit, V., & Glyde, H. R. (1986). Band tails in disordered systems. Physical Review B, 33(2), 1199.

[53] Thomsen, K. J., Murray, A. S., Jain, M. & Bøtter-Jensen, L. (2008). Laboratory fading rates of various luminescence signals fromfeldspar-rich sediment extracts. Radiation Measurements 43, 1474–1486

[54] Tsukamoto, S., Denby, P.M., Murray, A.S., BZtter-Jensen, L., (2006). Time resolved luminescence from feldspars: new insight into fading. Radiat. Meas. 41, 790–795.

[55] Tsang, C., & Street, R. A. (1979). Recombination in plasma-deposited amorphous Si: H. Luminescence decay. Physical Review B, 19(6), 3027.

[56] Urbach, F. (1953). The long-wavelength edge of photographic sensitivity and of the electronic absorption of solids Phys. Rev. 92 1324

[57] Varshni, Y. P. (1967). Temperature dependence of the energy gap in semiconductors. Physica, 34(1), 149-154.

[58] Wintle AG. (1973). Anomalous fading of thermoluminescence in mineral samples. Nature 245:143–44.

[59] Yanagi, K., & Kataura, H. (2010). Carbon nanotubes: Breaking Kasha's rule. Nature Photonics, 4(4), 200.

[60] Zotov, N., Yanev, Y., & Piriou, B. (2002). Time-resolved luminescence of Fe^{3+} and Mn^{2+} ions in hydrous volcanic glasses. Physics and chemistry of minerals, 29(4), 291-299.

Chapter 5

Dynamics of the deep-red photoluminescence emission in feldspar: role of the Fe^{3+} site dependence

A. K. Prasad[1] & M. Jain[1]

[1] *Center for Nuclear Technologies, Technical University of Denmark, DTU Risø Campus, Roskilde 4000, Denmark*

Under review

Abstract: We present here new characteristics of the Fe^{3+} emission in feldspar using a combination of site-selective spectroscopy and time-resolved photoluminescence at cryogenic temperatures. Although the variation in the peak energy of Fe^{3+} emission has been known to vary across feldspar samples depending on the composition and structure, it has never shown before that this emission can vary dynamically even within a single sample. We show for the first time that Fe^{3+} emission

can be discriminated from different sites even within a single sample; the red edge effect (excitation energy dependent emission) observed here can be a powerful tool for such discrimination even at a single crystal level. Similar to the emission process, the radiative relaxation in Fe^{3+} ($^4T_1 \rightarrow {}^6A_1$) is also shown to be a dynamic process depending on whether the ion is excited using resonant or non-resonant transition. We suggest that during resonant excitation, the excited state of Fe^{3+} undergoes a spin interaction with the crystal - a process that leads to a time delay in radiative relaxation.

5.1 Introduction

It is well known that the deep red emission ($\sim 1.7\,eV$) in feldspar arises from the Fe^{3+} ion (Brooks et al., 2002; Geake et al., 1977; Telfer and Walker, 1975). This ion substitutes for Al^{3+} in the tetrahedral sites in the feldspar lattice, and it participates in processes involving ionising radiation such as cathodoluminescence and thermoluminescence (Krbetschek et al., 2002; Visocekas et al., 2014). Optical excitation of this defect has been investigated previously to infer the energy levels of the ion (White et al., 1986; Poolton et al., 1995, 1996, 2006). It is well established that the deep red emission occurs from a spin forbidden $^4T_1 \rightarrow {}^6A_1$ transition within the d^5 electrons in Fe^{3+} ion.

The emission peak of Fe^{3+} is generally located between 680-740 nm (1.82-1.67 eV) depending on the K concentration (Krbetschek et al., 1997). Brooks et al. (2002) reported variations in the CL emission of Fe^{3+} as a result of changing Fe-O bond length due to potassium ions. It has been suggested that Fe^{3+} emission peak varies both in alkali feldspar and in plagioclase feldspar depending on the K/Na ratio or the Ca/Na ratio, respectively. Furthermore, the site occupancy of Fe^{3+} in alkali feldspars plays an important role in determining the emission wavelength. For example, Fe^{3+} substitutes for T_1 tetrahedral site in ordered feldspar leading to red emission, or both T_1 and T_2 sites in disordered feldspar lattice leading to IR emission (Finch and Klein, 1999; Krbetschek et al., 2002). The main causes of these variations are the crystal field effect and the changing bond lengths of Fe-O, both of which modify the $^4T_1 \rightarrow {}^6A_1$ transition energy level.

In terms of dosimetric research, it has been well known that the red TL undergoes very strong thermal quenching (e.g., Visocekas et al.,

2014), and it has been suggested that this signal does not suffer from anomalous fading, both in TL (Zink and Visocekas, 1997) and in IRSL (Stokes & Fattahi, 2003a, Fattahi & Stokes, 2003b, Fattahi et al., 2004). There are two different views on the role of Fe^{3+} in luminescence dosimetry. One suggestion is that Fe^{3+} captures a free electron during ionising irradiation (converting to Fe^{2+}), and subsequent capture of a hole during heating results in an Fe^{3+} excited state, which then relaxes to give the red emission (Visocekas et al., 2014). Recently, Jain et al. (2015) based on their IRSL study proposed an alternative view that Fe^{3+} captures a free hole during ionising irradiation (leading to Fe^{4+}, and a subsequent capture of free electron during optical excitation gives rise to the excited state of Fe^{3+}.

Despite a great interest in Fe^{3+}, both in dosimetric and mineralogical studies, the details of the Fe^{3+} system in feldspar are still missing. In contrast to the emission spectroscopy, the excitation energy levels of Fe^{3+} have seldom been studied. There is a general lack of understanding of a) the site dependence of Fe^{3+} emission in single samples (most previous studies have focussed on relative spectral variations across samples of different compositions), b) the effect of temperature on the emission, c) the effect of excitation energy on the emission energy and the relaxation lifetime (resonant vs non resonant), and d) the effect of temperature on the relaxation lifetime. Addressing these issues will give a better view of an important emission used in luminescence dosimetry, as well as provide insights into the interactions of Fe^{3+} with the feldspar lattice.

Poolton et al. (1996) mapped the energy levels of the Fe^{3+} ion in feldspar using site-selective spectroscopy. We use this approach here combined with low temperature measurements, and time resolved study to understand the dynamics of Fe^{3+} emission. We show that this emission not just varies across samples (as shown in the previous studies), but it can also vary significantly within the same sample. We also give insight into the spin forbidden relaxation mechanism in Fe^{3+}.

5.2 Experimental

We measured Fe^{3+} emission in 11 different feldspar samples listed in Table 5.1. The Fe content of these samples was measured using ICP-MS. Measurements were carried out using the Risø Station for CryOgenic LUminecence Research (COLUR); the details are given in Chapter 2. All

the steady-state PL measurements reported here were measured using the cooled CCD detector because of its better quantum efficiency in the red and near IR range compared to the PMT. The time-resolved measurements were carried out using TCSPC facility and pulsed Xe lamp, the emission monochromator and the PMT detector.

5.3 Results

Our investigations into the temperature and excitation energy dependence of the Fe^{3+} emission, and its decay characteristics are described below.

5.3.1 Fe^{3+} excitation and emission: general characteristics

Figure 5.1(a) shows the emission spectrum of 11 different feldspars samples (Table 5.1) at room temperature. The samples were excited with photons energy of 4.67 eV and the deep red emission was recorded between 1.39 and 2.05 eV. Figure 5.1 (b) shows the corresponding excitation spectra where the emission was fixed at the peak wavelength, while the excitation was scanned from 1.9 to 4.86 eV.

We observe that the emission peak position moves from 1.67 eV in R58 to 1.8 eV in R64. The majority of the samples have emission peaks at ~ 1.7 eV; this emission arises from the forbidden $^4T_1 \rightarrow {}^6A_1$ transition (Telfer & Walker, 1975; White et al., 1986). The excitation spectra in Figure 5.1(b) show several resonant excitation peaks in the region 2.5 to 3.4 eV, and a non-resonant continuum up to > 4.5 eV. Similar to the emission spectra, the resonant excitation peaks, as well as the rise of the non-resonant continuum vary with feldspar composition.

These data confirm the earlier study by (Poolton et al., 1996, 2006), who showed that the peak position of Fe^{3+} PL emission is related to the mineralogical composition. However, we do not observe any correlation between the emission peak position with respect to plagioclase and alkali feldspar in our samples; this suggests that the peak energy variations in our samples may perhaps be controlled by other factors such as the structural state of feldspar, or the tetrahedral site dependence of Fe^{3+}.

We chose sample R56 (alkali feldspar with similar K and Na feldspar content: it is a Sanidine feldspar) as a representative sample for detailed investigations; its emission peak position is similar to that for samples

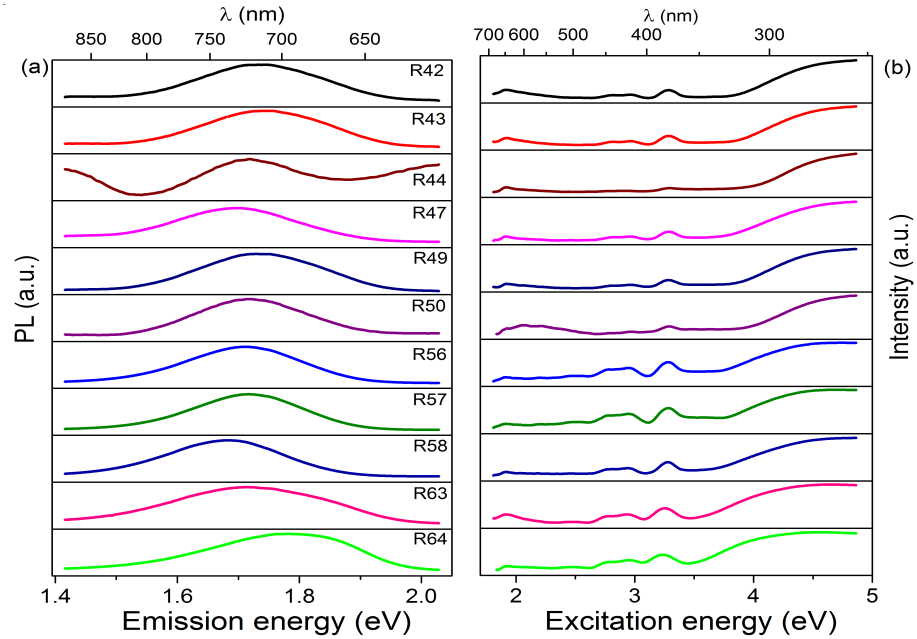

Figure 5.1: (a) Emission and (b) excitation spectra of 11 different feldspars samples measured at room temperature. The emission spectra were obtained using the excitation at 4.67 eV, whereas the excitation spectra were obtained while fixing the detection at the peak emission energy.

Table 5.1: Feldspar samples used in this studies, and their major cation (K, Na, Ca) and Fe^{3+} ion concentrations.$: Not measured.u/k:Unknown

Sample Code	Type of Feldspar	Provenance	K	Na	Ca	Fe (ng/g)
R28	M	Switzerland	0.95	0.05	0	$
R42	S	China	0.91	0.08	0.01	1185
R43	S	China	0.91	0.08	0.01	943.2
R44	M	Spain	0.91	0.08	0.01	753.4
R47	S	China	0.85	0.12	0.03	207.3
R49	S	China	0.83	0.16	0.02	691.9
R50	M	u/k	0.8	0.18	0.01	1597.4
R56	M	u/k	0.52	0.46	0.02	2124.5
R57	M	u/k	0.43	0.53	0.04	1537.3
R58	M	u/k	0.27	0.63	0.1	1607.7
R63	S	Iceland	0.03	0.29	0.69	36790.7
R64	S	Iceland	0.01	0.15	0.85	11263.7

R44, R50, R57 and R63, and lies in close vicinity of the emission peaks of R42, R47 and R49 (Figure 5.1(a)). The purpose of these detailed measurements was to understand the temperature and excitation- energy dependence of the Fe^{3+} emission.

5.3.2 Temperature and excitation-energy dependence of the Fe^{3+} emission in R56

Figure 5.2 gives a closer view of the excitation and the emission spectrum of R56 from Figure 5.1; the PL intensity is plotted on the log intensity scale for the excitation spectrum (right) and on the linear scale for the emission spectrum (left). The excitation spectrum was obtained by fixing the emission at 1.7 eV, while the emission spectrum was obtained using 4.67 eV excitation. The inset of Figure 5.2 shows the energy level diagram for the isolated Fe^{3+} defect (Poolton et al., 1996; White et al., 1986). It can be seen that there are several excitation levels but the radiative relaxation occurs only from the lowest $^4T_1(G)$ level; the absolute energy levels depend upon the crystal field in the sample. Four of these transitions are marked against the dominant emission and excitation peak in R56 (Figure 5.2).

Fe^{3+} emission is known to show a strong thermal quenching at room

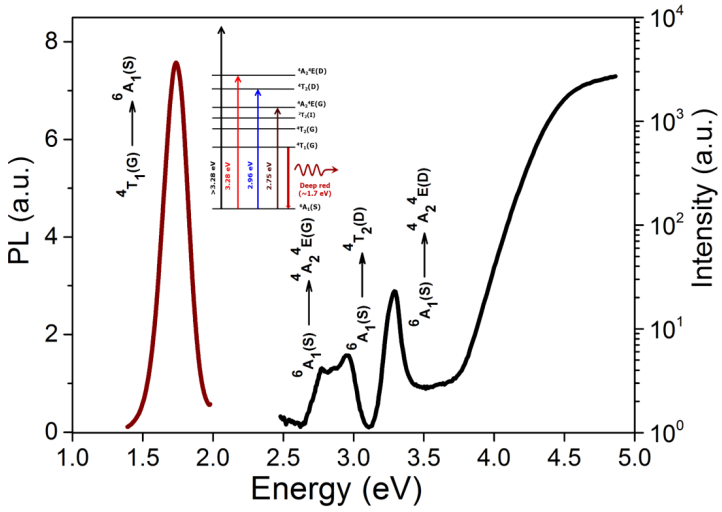

Figure 5.2: A detailed view of the emission and excitation spectra of sample R56. The inset shows the energy level diagram of an isolated Fe^{3+} within a host lattice. The main transitions following this diagram are marked against the peak data.

temperature (White et al., 1986; Poolton et al., 1995); however, there are not many studies of dynamics of the peak movement as a function of temperature. In order to examine the effect of cooling on R56, we measured PL emission spectra at different temperatures while exciting with 4.67 eV photons (Figure 5.3(a)). We observe a gradual red shift in the emission peak and an increase in the emission intensity with cooling. The emission shift has a magnitude of 0.03 eV from room temperature to 7 K. The most plausible reason for the shift is participation of higher vibrational levels at higher temperatures (phonon effect). This interpretation is also confirmed by the fact that the PL peak becomes narrower with cooling.

The effect of changing the excitation energy on the emission peak energy has never been, to our knowledge, investigated before. Figure 5.3(b) shows the emission spectra measured at 295 K, as the excitation energy was varied from 4 to 4.86 eV. Similar to the orange-green emission in feldspar (Chapter 4), we observe an excitation-energy dependent emission (Figure 5.3(b)); there is a red shift in the emission peak with a decrease in the excitation energy (red edge effect). Figure 5.4(a) shows the summary of the peak shift as a function of excitation energy in both K rich alkali feldspar (R56; black coloured 'plus' symbol) and a Na rich

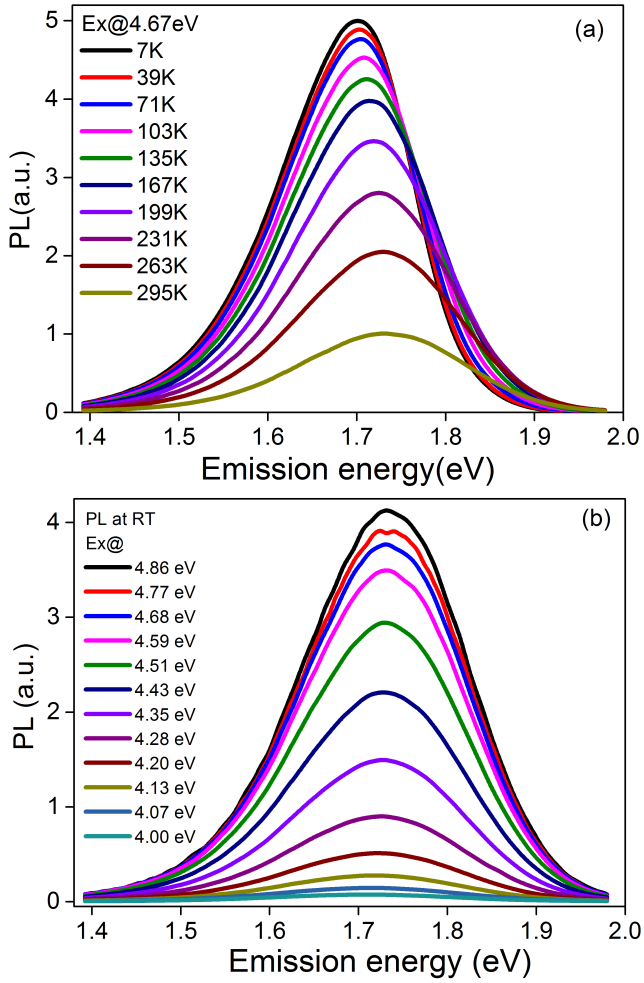

Figure 5.3: (a) PL emission spectra of R56 at different temperatures using a 4.67 eV excitation. (b) PL emission spectra of R56 measured at 295 K using different excitation energies.

alkali Feldspar (R58; red coloured 'plus' symbol) samples at room temperature. The reference excitation spectra for these samples are also plotted using the same colour scheme (black for R56 and red for R58); these excitation spectra were obtained while fixing the emission at 1.7 eV. Figure 5.4(b) is similar to Figure 5.4(a) except that the full width half maximum (FWHM) of the PL peak is plotted here. Figure 5.4(a) shows that the red-edge effect occurs both in Na and K feldspar (although with a different magnitudes) in the non-resonant excitation continuum; there is red shift of ~ 0.02 eV in R56 and ~ 0.04 eV in R58. There is also suggestion for a minor red-edge effect across the excitation peak at 3.3 eV (Figure 5.4(a)). The FWHM decreases with the rise in the non-resonant excitation energy (Figure 5.4(b)).

To gain insight into this red edge effect, we repeated the same experiment as described for Figure 5.4, but with different measurement temperatures. These temperature-dependent measurements were carried out only for the sample (R56). Figure 5.5 shows the summary of the Fe^{3+} emission peak as a function of excitation energy and temperature; peak position is shown in Figure 5.5(a), FWHM in 5.5(b) and normalised peak area in Figure 5.5(c). The red edge effect is significantly enhanced with cooling (Figure 5.5(a)), however, interestingly; the FWHM shows a peak form in the non-resonant excitation region at lower temperatures (Figure 5.5(b)). Furthermore, there is a significant overall reduction in the FWHM with sample cooling both in the resonant and non-resonant regions; this is the same as the temperature dependent phonon effect discussed for Figure 5.3(a).

Figure 5.5(c) shows that thermal quenching exists (reduction in the PL emission area with a rise in temperature) for all the excitation energies. However, interestingly, the extent of thermal quenching varies with the excitation energy. This observation of the influence of excitation energy on thermal quenching has never been reported before.

In summary, this section makes several new observations: a) a strong phonon effect in Fe^{3+} PL emission, b) a red edge effect which is enhanced with sample cooling, and c) different thermal quenching behaviour of the Fe^{3+} emission depending on the excitation energy.
As discussed in the introduction, the emission peak in Fe^{3+} has been known to shift across samples because of composition or its occupancy site. In our samples, we do not see a correlation between composition and peak position (Figure 5.1(c)), suggesting that the latter may be

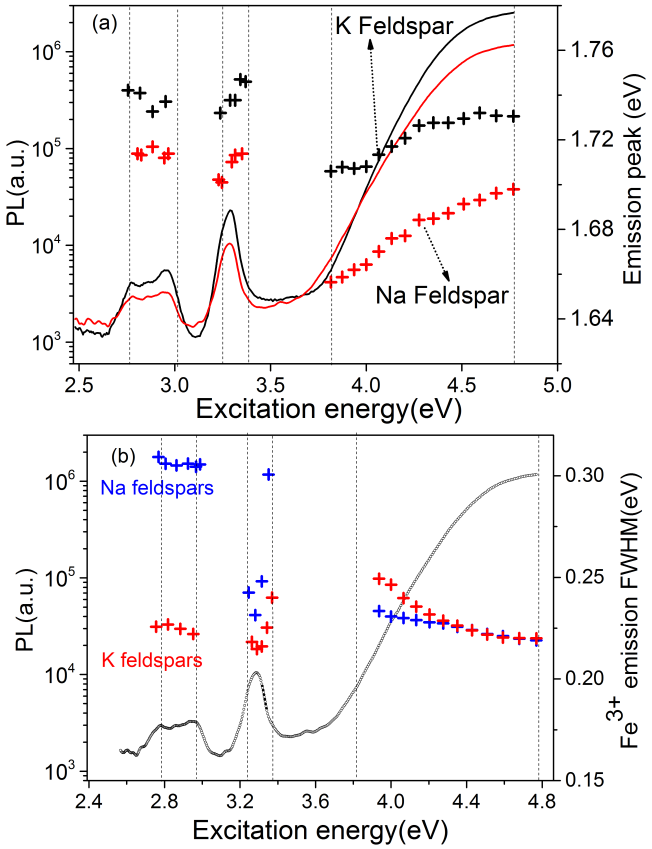

Figure 5.4: (a) Dependence of the Fe^{3+} PL emission peak on the excitation energy for R56 (K rich feldspar) and R58 (Na rich feldspar) at 295 K. The reference excitation spectrum is plotted using the same colour as the peak symbols. (b) Same as (a) but showing the full width half maximum (FWHM) of the Fe^{3+} emission peak

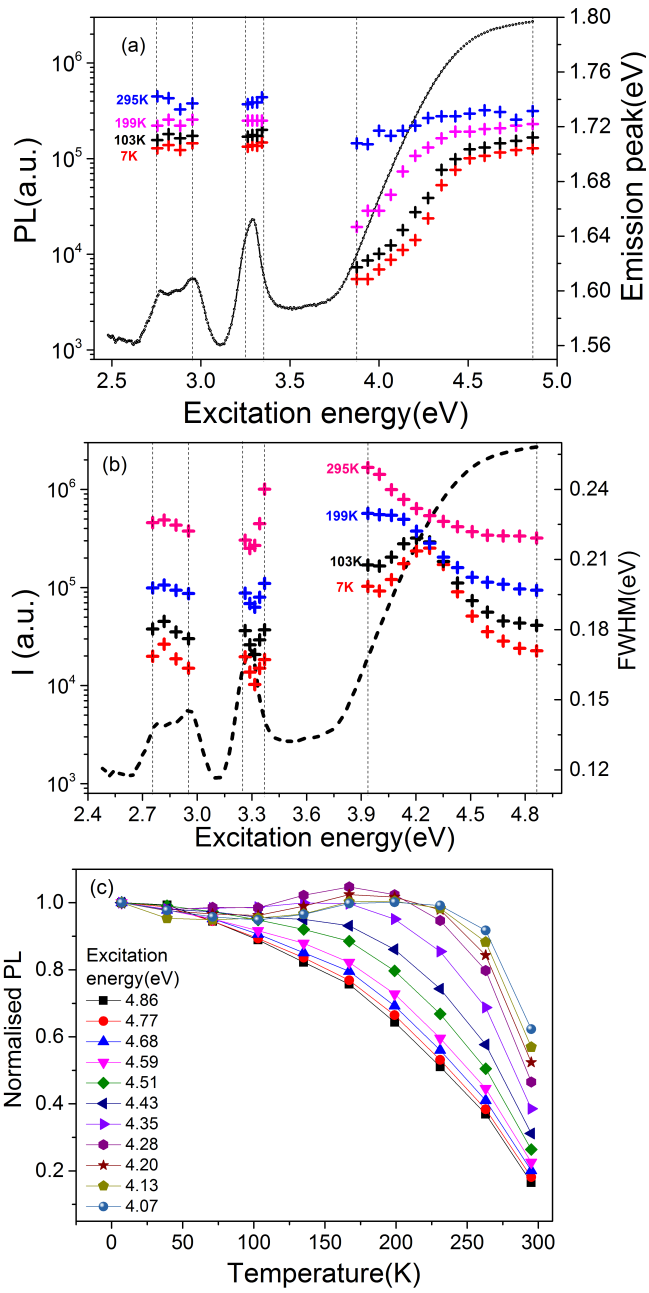

Figure 5.5: (a) Dependence of the Fe^{3+} PL emission peak on the excitation energy and on the measurement temperature for R56. (b) same as (a) but for FWHM. (c) dependence of integrated PL peak intensity on measurement temperature for different excitation energies.

an important effect. The sample R56 contains roughly equal amounts of K and Na content but we do not know if these are phase exsolved. Nonetheless, it is conceivable that red edge effect observed in our data arises from changes in the relative excitation of the T_1 and T_2 sites, or separate K and Na feldspar phases. To test this hypothesis, we chose a pure K feldspar sample (R28) (Table 5.1). The emission spectra measured with three different excitation energies are shown in Figure 5.6. Unlike sample R56 we do not see any red edge effect in R28. The three peaks are very similar and can be described by a single Gaussian function. Figure 5.6 inset shows a single peak fitting for the case of 4.86 eV excitation.

The data from R28 suggest that sample R56 must contain mixed phases or two different sites of Fe^{3+} with different crystal field around them; what we observe is a summed PL emission from both the sites. On non-resonant excitation, the relative strength of the two emissions changes, giving rise to an apparant peak shift in the summed signal. With this insight, we re-analysed the data reported in Figures 5.3, 5.4 and 5.5, but with a two peak model, representing T_1 and T_2 sites of the Fe^{3+} ion. Some of this re-analysed data is reported below.

5.3.3 Testing the two peak model in R56

Figure 5.7(a) shows the temperature dependent FWHM of the Fe^{3+} emission for all the excitation energies (4-4.86 eV) and measurement temperatures; note that Figure 5.5(b) represents only part of this excitation-emission-temperature matrix. The FWHM data show an apparent peak trend which begins to emerge at temperatures below 200 K. At temperatures below 100 K there is a clear peak at $\sim$ 4.3 eV excitation energy. These FWHM data support the two-peak model, which becomes especially clearer at low temperatures because of reduction in the phonon effect and thereby narrowing of the individual peaks. Thus, the end members on the excitation energy scale, represent dominant excitation of a single peak resulting in a narrow FWHM, whereas around 4.3 eV both the peaks are excited resulting in a wide FWHM. The overall result is a peak shaped variation in FWHM as a function of excitation energy.

With this qualitative confirmation of the application of two peak model to R56, we performed peak fitting of the emission spectra obtained using 4.86 eV at 295 K. As expected, unlike R28, the data from R56 were best described by a sum of two Gaussian peaks. As a further qualitative test of the two peak model, we measured the excitation

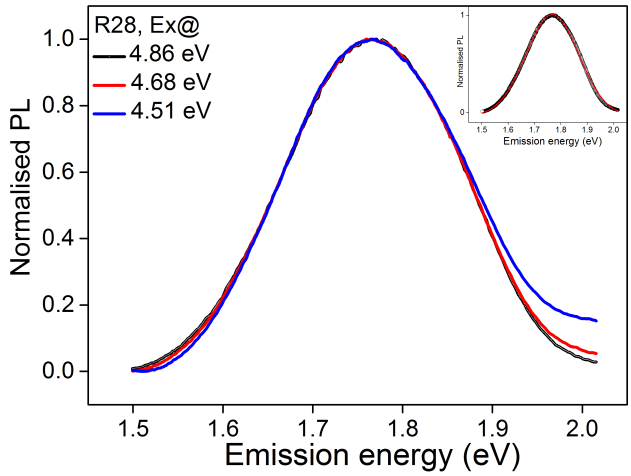

Figure 5.6: PL emission of R28 for three different excitation energies. The inset shows the fit of the 4.86 eV data to a single Gaussian peak.

spectrum of R56 at 7 K while fixing the emission window at 1.79 eV and 1.57 eV, thus trying to obtain the site specific excitation from a complex sample. A 7 K temperature was used to maximise the separation of the two peaks (Figure 5.7(a)). The data are shown in Figure 5.7(c). We observe a slight variation in the resonant peaks at $\sim$ 2.9 eV and a clear shift of the non-resonant excitation, supporting the view that different sites of Fe^{3+} are present in this R56.

Finally, to test make a quantitative test of the two-peak model, we tried to fit a sum of two Gaussian functions to all our excitation-emission-temperature data from R56. The peaks P1 and P2 are shown in Figure 5.7(d) for 7 K and 295 K only (to avoid cluttering); as can be seen in the 7 K data, although, peak fitting helps to reduce the red edge effect, it does not completely eliminate it. We also tried to force-fit two shared peak energies to all the data, but this attempt was unsuccessful; the obtained peak fits were poor suggesting that two common peaks do not adequately describe the red edge effect in R56.

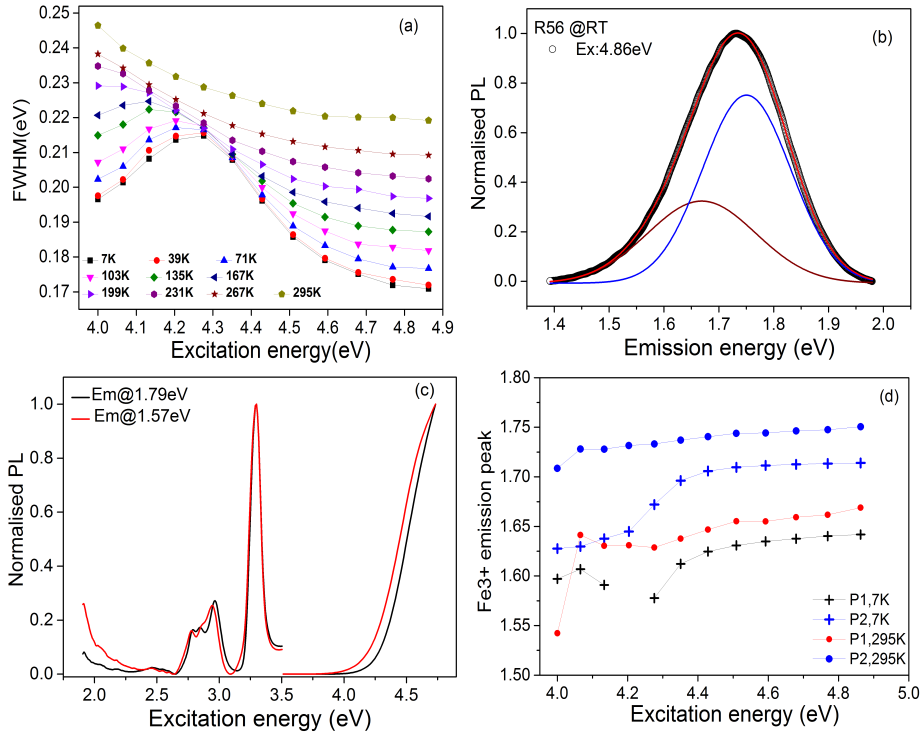

Figure 5.7: (a) Temperature dependent FWHM the Fe^{3+} PL emission for different excitation energies. (b) PL emission spectrum at 295 K (4.86 eV excitation) fitted to a sum of two Gaussian peak functions. (c) Excitation spectrum of R56 at 7 K for detection fixed at 1.79 eV and 1.57 eV. (d) Dependence of the two peak components of the Fe^{3+} emission on the excitation energy; the data obtained at 295 K or 7 K data are inter-compared.

5.3.4 Time resolved PL data

Finally, we examined the temperature dependent lifetime of Fe^{3+} emission at 1.7 eV with excitations at 4.77 eV (non-resonant) and 3.29 eV (resonant); the data are shown in Figure 5.8(a), and 5.8(b), respectively, and analysis yield summarised in Table 5.2. All the time-resolved data show a slow decay confirming the spin forbidden radiative transition in Fe^{3+} (e.g. Prasad et al., 2016). Furthermore there is an increase in the decay rate with temperature, confirming the thermal quenching mechanism in Fe^{3+}; at higher temperature the lifetime decreases because of non-radiative relaxation.

The resonant PL decay data could not be fitted to either a single exponential, or a sum of two exponential functions as the data after $\sim$ 4 ms shows an unusual kink(See Figure 5.8(b); this perhaps suggest a short-lived feedback into the resonant state before the radiative relaxation begins to dominate. It is possible that an additional time constant, involving energy transfer between the excited state and the crystal, will be involved in changing the spin state of the excited ion. The non-resonant data on the other hand show clear single exponential decay until the temperature of 200 K, while at room temperature the decay shows two exponentials. As inferred from Figure 5.7(a), the 4.77 eV photons are likely to excite only one of the Fe^{3+} emissions sites at low temperature, while exciting both the Fe^{3+} emissions sites at room temperature. Thus the single exponential and double exponential PL decay in Figure 5.8(b), may be related to the site dependent excitation of Fe^{3+} in two different phases. The energy interaction process may not apply to the non-resonant excitation, therefore we do not see a kink in these data.

Table 5.2: PL decay lifetime data of Fe^{3+} measured using R56.

Lifetimes for non-resonant (4.77 eV) and resonant(3.29 eV) excitations		7 K	103 K	199 K	295 K (ms)
4.77 eV	$\tau_{4.77}$	5.07	4.43	3.79	2.97 and 0.90
3.29 eV	$\tau_{3.3}$	4.97	4.24	3.80	3.32
	$\tau^*_{3.3}$	6.09	5.18	4.35	2.22

The lifetime values ($\tau_{4.77}$) derived from exponential fitting of the non-resonant data are summarised in Table 5.2. For the resonant data, we

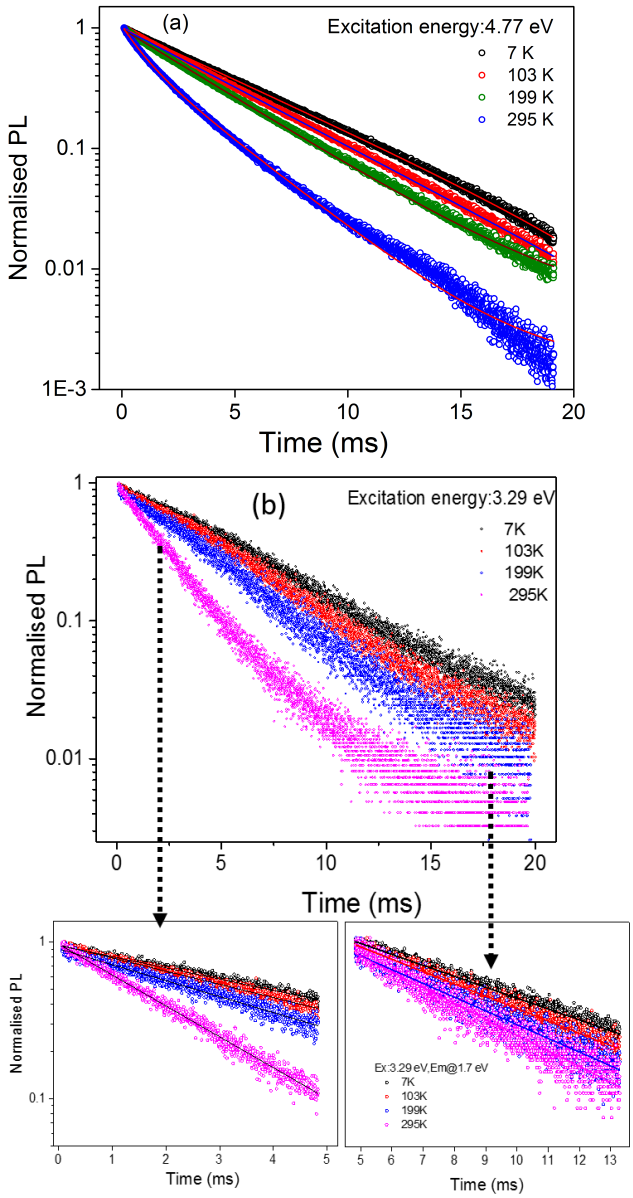

Figure 5.8: Temperature dependent PL decay measurements using (a) non-resonant excitation at 4.77 eV (b) resonant excitation at 3.29 eV. The emission detection was fixed at 1.7 eV.The closer look of the decay data before kink and after kink is pointed through arrow.

splitted the curves in two sections (Figure 5.8(b)), before and after the kink, and fitted them individually to exponential functions; the lifetimes are in summarised in Table 5.2 as $\tau^*_{3.3}$ and $\tau_{3.3}$, respectively. It can be seen that the τ values for the resonant and non-resonant excitations ($\tau_{3.3}$ and $\tau_{4.77}$) are almost same; these must, therefore, reflect the lifetime for the radiative transitions ($^4T_1 \rightarrow {}^6A_1$). The $\tau^*_{3.3}$ values (initial kink) on the other hand, in our view, possibly reflect the time scale involved in interaction between the excited state and the crystal through energy transfer. A more sophisticated model is necessary to determine the exact lifetime of this process.

5.3.5 Dose dependence of the Fe^{3+} emission

Finally, we examined if the Fe^{3+} PL emission could be exploited to measure dose in a sample. We expect that the Fe^{3+} concentration should decrease with radiation dose because of the conversion of this species to either Fe^{2+} (Visocekas et al., 2014) or Fe^{4+} (Jain et al., 2015). We tested this hypothesis by exposing our sample to different durations of X-rays and measuring the subsequent Fe^{3+} PL spectra using 3.29 eV (377 nm) optical stimulation. Figure 5.9 shows the results; we do not observe any clear dosimetric PL signal. This is likely because of a huge background arising from a large concentration of Fe^{3+} in feldspars (See Table 5.1). It implies that irradiation must change the state of only a negligible amount of Fe^{3+}.

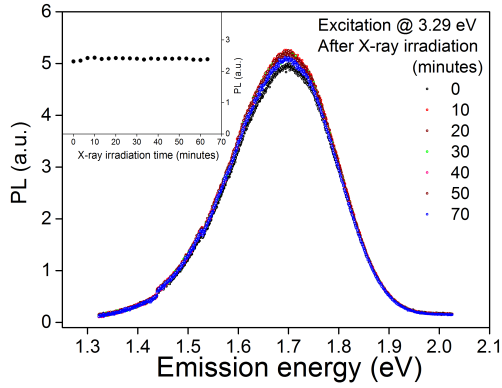

Figure 5.9: X-ray irradiation dependence of Fe^{3+} PL emission using a 3.29 eV excitation energy.

5.4 Summary and Conclusions

We carried out site selective spectroscopy of Fe^{3+} in a variety of samples, and chose an alkali feldspar sample for detailed investigations (R56). We make the following conclusions from our study:

1. Both the emission and resonant excitation peaks of Fe^{3+} vary with sample composition. However, there is no clear correlation between the emission peak and K content in our samples. This suggests that the variation in the emission must largely be dependent on the structural state and/or the tetrahedral site dependence of Fe^{3+} in our samples.

2. There is a strong red shift in the Fe^{3+} emission and a reduction in its FWHM with cooling. We attribute these effects to relaxation through the lower vibrational levels (phonon effect) of the ion. The overall changes in the peak shape with temperature suggest a homogeneous thermal broadening effect.

3. Our site-selective data for the first time demonstrate variability in Fe^{3+} within a single sample. We show a strong red edge effect (excitation-energy dependent emission) in both K rich (R56) and Na rich (R58) alkali feldspar; this effect is systematically enhanced at cryogenic temperatures. We qualitatively explain the red-edge effect (both variation in peak energy and FWHM) in terms of two different site occupancies of Fe^{3+} in R56. Our results suggest that red edge effect (especially at cryogenic temperatures) could be a powerful tool to determine the mineralogical/structural complexity within a single feldspar sample.

4. The quantitative evaluation of red edge effect using 2 shared Gaussian peaks is not successful. This aspect requires further investigations.

5. The PL decay study at room temperature and at 7 K using resonant or non-resonant excitation suggests that the $^4T_1 \rightarrow {}^6A_1$ transition is a dynamic process. During the resonant excitation an additional time step is involved, possibly due to an energy exchange between the excited state and the crystal resulting in a spin change; the time scale for this process is of the order of milliseconds and it depends on temperature. In the case of non-resonant excitation, this additional step is not involved in the relaxation process. This is an interesting, and perhaps the most important new observation of this study, which requires further investigations.

Bibliography

[1] Brooks, R. J., Finch, A. A., Hole, D. E., Townsend, P. D., & Wu, Z. L. (2002). The red to near-infrared luminescence in alkali feldspar. Contributions to Mineralogy and Petrology, 143(4), 484-494.

[2] Finch, A. A., & Klein, J. (1999). The causes and petrological significance of cathodoluminescence emissions from alkali feldspars. Contributions to Mineralogy and Petrology, 135(2-3), 234-243.

[3] Geake, J. E., Walker, G., Telfer, D. J., & Mills, A. A. (1977). The cause and significance of luminescence in lunar plagioclase. Philosophical Transactions of the Royal Society of London A: Mathematical, Physical and Engineering Sciences, 285(1327), 403-408.

[4] Poolton, N. R. J., Mauz, B., Lang, A., Jain, M., & Malins, A. E. R. (2006). Optical excitation processes in the near band-edge region of KAlSi3O8 and NaAlSi3O8 feldspar. Radiation measurements, 41(5), 542-548.

[5] Poolton, N. R. J., Bøtter-Jensen, L., & Johnsen, O. (1996). On the relationship between luminescence excitation spectra and feldspar mineralogy. Radiation measurements, 26(1), 93-101.

[6] Poolton, N. R. J., Bøtter-Jensen, L., & Duller, G. A. T. (1995). Thermal quenching of luminescence processes in feldspars. Radiation Measurements, 24(1), 57-66.

[7] Krbetschek, M. R., Götze, J., Dietrich, A., & Trautmann, T. (1997). Spectral information from minerals relevant for luminescence dating. Radiation Measurements, 27(5), 695-748.

[8] Krbetschek, M. R., Götze, J., Irmer, G., Rieser, U., & Trautmann, T. (2002). The red luminescence emission of feldspar and its wavelength dependence on K, Na, Ca–composition. Mineralogy and Petrology, 76(3-4), 167-177.

[9] Fattahi, M., Stokes, S., & Lamothe, M. (2004). Red luminescence emission from potassium feldspars stimulated by infrared. Ancient TL, 22(2), 35-44.

[10] Fattahi, M., & Stokes, S. (2003a). Red luminescence from potassium feldspar for dating applications: a study of some properties relevant for dating. Radiation Measurements, 37(6), 647-660.

[11] Prasad, A. K., Lapp, T., Kook, M., & Jain, M. (2016). Probing luminescence centers in Na rich feldspar. Radiation Measurements, 90, 292-297.

[12] Stokes, S., & Fattahi, M. (2003b). Red emission luminescence from quartz and feldspar for dating applications: an overview. Radiation Measurements, 37(4), 383-395.

[13] Telfer, D. J., & Walker, G. (1975). Optical detection of Fe^{3+} in lunar plagioclase. Nature, 258(5537), 694-695.

[14] Visocekas, R., Barthou, C., & Blanc, P. (2014). Thermal quenching of far-red Fe 3+ thermoluminescence of volcanic K-feldspars. Radiation Measurements, 61, 52-73.

[15] Zink, A. J. C., & Visocekas, R. (1997). Datability of sanidine feldspars using the near-infrared TL emission. Radiation Measurements, 27(2), 251-261.

[16] Wintle, A. G. (1973). Anomalous fading of thermo-luminescence in mineral samples. Nature, 245(5421), 143-144.

[17] White, W. B., Matsumara, M., Linnehan, D. G., Furukawa, T., Chandrasekhar, B. K. (1986). Absorption and luminescence of Fe^{3+} in single-crystal orthoclase. Am. Mineral. 71 (14) 15–19.

Chapter 6

Probing metastable Sm^{2+} and optically stimulated tunnelling emission in YPO_4:Ce,Sm

A. K. Prasad[1], M. Kook[1], M. Jain[1]

[1] *Center for Nuclear Technologies, Technical University of Denmark DTU Risø Campus, Roskilde-4000, Denmark.*

Published in: Radiation Measurements, in press.

Abstract: When the model dosimetry system YPO_4: Ce^{3+}, Sm^{3+} is exposed to X-rays, the charge state of the dopants changes, becoming Ce^{4+} and Sm^{2+} via hole and electron trapping, respectively which are metastable; the original charge states can be achieved through electron transfer back from Sm^{2+} to Ce^{4+} via optical stimulation. The work presented here adds further details to the energy levels of the metastable Sm^{2+} defect and the electron transfer processes by undertaking measurements of a) Sm^{2+} excitation spectrum through the internal $^5D_0 \rightarrow {}^7F_2$ emission at 7 K), b) relaxation lifetime of Sm^{2+} ($^5D_0$ state) and its temperature dependence to provide insights into thermal quenching, and c)

the kinetics of localised recombination from Sm^{2+} to Ce^{4+} on nanoseconds to seconds time scales using sub-band-edge excitation.

Keywords: Radiophotoluminescence, low temperature spectroscopy, localised recombination, excited-state tunnelling, thermal quenching, Sm^{2+} and Ce^{3+}, relaxation lifetime.

6.1 Introduction

Doping wide band-gap materials with rare earth ions introduces defect levels within the bandgap which makes them useful in many applications, such as charge storage phosphors for use in luminescence dosimetry (Chakrabarti et al., 1989; Meijerink et al., 1991), display phosphors and optical memory (Thiel et al., 2002; Ding et al., 2016), and persistent luminescent materials (Matsuzawa et al., 1996; Hölsa et al., 2001). The extensive knowledge accumulated over the last four to five decades in identifying the behaviour and energy levels of lanthanide dopants within the band gap of a host material gives us a clear idea about whether they will act as an electron or a hole trap on exposure to ionizing radiation (for summary, see Dorenbos et al., 2003, 2011). In this respect, YPO_4 co-doped with Ce^{3+} and Sm^{3+} ions shows excellent promise as a model system for fundamental studies: on irradiation with X–rays, these defects form the metastable states Ce^{4+} and Sm^{2+} whose energy levels can be precisely characterised for controlled charge transfer (Dorenbos et al., 2003; Poolton et al., 2012).

Previous work to understand the luminescence charge transfer properties of YPO_4:Ce^{3+}, Sm^{3+} have used synchrotron radiation (4-20 eV) and both optical and thermoluminescence spectroscopy (Pieterson et al., 2001; Poolton et al., 2010, 2012; Dorenbos et al., 2011; Mandowski and Bos, 2011; Bos et al., 2010). These studies have also allowed determination of the electron and hole trap energies within the band-gap. However, understanding the precise nature of energy transfer from Sm^{2+} to Ce^{4+} processes requires detailed information concerning the excited state energy levels of the metastable Sm^{2+} defect, and this is still very much work-in-progress. The first indications of the Sm^{2+} excited state energy levels came from the optically stimulated luminescence (OSL) excitation spectra measured via the Ce^{3+} emission (Bos et al., 2010). As this involves excited-state tunnelling from Sm^{2+} to Ce^{4+}, the transitions were

significantly broadened due to interference with 4f 5d (SmA, SmB) bands (which are the most effective conduit for the tunnelling), and only limited spectroscopic information was obtainable. By using a low flux 1.92 eV laser stimulation at 10 K, Poolton et al. (2012) were able to exclusively probe isolated Sm^{2+} emission 4f-4f transition, and thereby determine the ground state energy levels in more detail. In the same study a 2.33 eV laser probe for the emission at 10 K confirmed the simultaneous presence of both stable Sm^{3+} ions and metastable Sm^{2+} ions in the YPO_4 host. Regarding charge transfer, the OSL in YPO_4: Ce, Sm has previously been studied using the 2.79 eV excitation which photo-ionises the Sm^{2+} followed by recombination via the conduction band (delocalised charge transfer) at the Ce^{4+} (Poolton et al., 2010). In contrast, thermal decay (TL) has shown a tunnelling emission corresponding to a continuum of localised recombination probabilities, superimposed on the TL peaks produced by delocalised recombination (Dobrowolska et al., 2014). Detailed understanding of the tunnelling kinetics is tedious using the TL signal because of a continuum of temperature dependent excitation probabilities and an overlap between localised and delocalised processes. This problem can be avoided using an energy specific, sub-bandgap excitation leading to a direct charge transfer from Sm^{2+} to Ce^{4+}.

The missing details of the YPO_4:Ce^{3+}, Sm^{3+} model system are: knowledge about the exact energy levels of the excited state of metastable Sm^{2+}, and the relaxation rates from the excited-to-ground states of the ion. Furthermore, the charge transfers kinetics using Sm^{2+} excited state tunnelling is not understood at the moment; there is a general need for such information on model systems, as it is important for testing and refining our theoretical understanding of stimulated localised recombination emission (e.g. see Jain et al., 2012, 2015).

In this article, we move towards a more complete picture of the YPO_4: Ce, Sm model system by measuring for the first time the detailed excitation spectra of metastable Sm^{2+} at 7 K via the Sm^{2+} emission itself; this allows us to determine the precise location of the ion's excited states. We also measure the temperature dependent relaxation lifetime and dose-dependency of this internal Sm^{2+} emission (Stokes shifted OSL or radio-photoluminescence), without relying on any charge transfer to Ce^{4+}. Finally, we study the optically stimulated tunnelling recombination from the excited states of Sm^{2+} to the Ce^{4+}. The method of isolating the luminescence processes of individual metastable defects (rather than

relying on the charge transfer between defects) is an important outcome of this work which can be applied to the other lanthanide co-dopants, as well as to complex natural materials, such as feldspars.

6.2 Instrumentation and sample details

The yttrium phosphate sample used in this study was co-doped with 0.5% cerium and 0.5% samarium, and prepared by solid state reaction (for details, see Bos et al., 2008). All measurements were made using the Risø station for CryOgenic LUminescence Research (COLUR) at DTU Nutech. This system consists of a Horiba Fluorolog-3 spectrofluorometer, upgraded to include a temperature controlled (7-300 K) closed-loop cryostat, an X-ray irradiation facility (40 kV, 100 µA copper anode with 3 ms action X-ray shutter), and multiple ports for laser excitation and photo-detection, for use in a number of dual-probe type experiments. The sample is in vacuum, attached directly to the cryostat cold finger.

Luminescence excitation spectra were measured with a 450 W Xenon CW lamp and detected with a photomultiplier tube (PMT; S1 response). A series of appropriate long-pass filters were placed between the sample and the emission monochromator to remove second order excitation light.

Time resolved luminescence measurements were measured using time-correlated single photon counting (TCSPC), with a 657 nm ($\sim$ 1.89 eV) laser diode as the source. The laser has a maximum power of 40 mW, and works in either CW mode, or can be modulated up to 155 MHz with rise/fall times of < 3 ns, with a minimum pulse width $\sim$ 50 ns. Dose-dependent OSL curves were obtained with the laser in CW mode and directly recorded using a PMT (with U340 filters), external to the Fluorolog monochromators; this exclusively samples the Ce^{3+} emission.

6.3 Results and Discussion

6.3.1 Low temperature luminescence properties of Sm^{2+}

X-irradiation of YPO_4: Ce, Sm (9.2 eV bandgap) leads to the formation of free electrons and holes. The original charge states of the dopants (Sm^{3+}, Ce^{3+}) change to metastable state (Sm^{2+}, Ce^{4+}). On capturing the electrons and holes they return to their original (Sm^{3+}, Ce^{3+}) configuration after several days via non-radiative ground-state tunnelling,

or via external stimulation by heat or light resulting in TL and OSL, respectively. Figure 6.1(a) shows the laser excited Sm^{2+} emission spectra at 7 K for different X-ray irradiation durations. The emission arises exclusively from the internal 4f ($^5D_0 \rightarrow {}^7F_{2,3,4}$) transitions at 1.70, 1.64 and 1.54 eV, respectively, all of which increase in intensity with dose. The dose-dependent change in the PL intensity confirms that we are directly probing the metastable Sm^{2+}; such signal in dosimetry is commonly named as radio-photoluminescence (Schulman et.al., 1951). Only some Sm^{3+} are converted to Sm^{2+} and the inset to Figure 6.1(a) shows the $^4G_{5/2} \rightarrow {}^6H_{5/2,7/2,9/2,11/2}$ transitions of Sm^{3+}, excited in a non-dosed sample under 3.06 eV laser excitation; the separate spectral emission features of Sm^{2+} and Sm^{3+} are clearly distinguished. These results are in good agreement with those of Poolton et al. (2012) confirming the reliability of our measurements.

The excitation spectrum of Sm^{2+} was recorded at 7 K after 3 hours of X-ray irradiation with the detection fixed at 1.70 eV (the $^5D_0 \rightarrow {}^7F_2$ transition) and the excitation energy varying from 1.75 to 2.05 eV (Figure 6.1(b). As Sm^{2+} has a trap depth of 2.3 eV (Bos et al., 2010; Poolton et al., 2010) excitation in the energy range 1.75 - 2.1 eV has insufficient energy to evict charge from the centre via the conduction band. The observed peaks, therefore, represent the internal transitions within Sm^{2+}, an interpretation further strengthened by the fact that the signal does not decay with time (steady state). The clearly resolved peaks in the present excitation spectrum contrast with those in previous work where the transitions were observed via Ce^{3+} emission by excited state tunnelling (Dorenbos et al., 2011; Bos et al., 2010; Poolton et al., 2010, 2012); this charge transfer process in the earlier work led to extensive broadening of the transitions, making most of the features almost indistinguishable. The resolution of the spectral features obtained here allow for the first time a clear identification of the excited levels of Sm^{2+} in the YPO_4 host. These excitation peaks arise from internal 4f-4f transitions of Sm^{2+} and, in combination with the previous work regarding analysing the emission lines (Poolton et al., 2012), we tentatively assign $^7F_0 \rightarrow {}^5D_{0,1,2,3}$ at 1.837, 1.879, 1.898 and 1.977 eV respectively, and $^7F_1 \rightarrow {}^5D_0$ at 1.785 eV. Low intensity phonon replicas ($\sim$ 20 meV) associated with each electronic transition are also observed.

The time resolved luminescence of the main Sm^{2+} peak emission excited using the 1.89 eV laser at 7 K, is shown in Figure 6.1(c); the in-

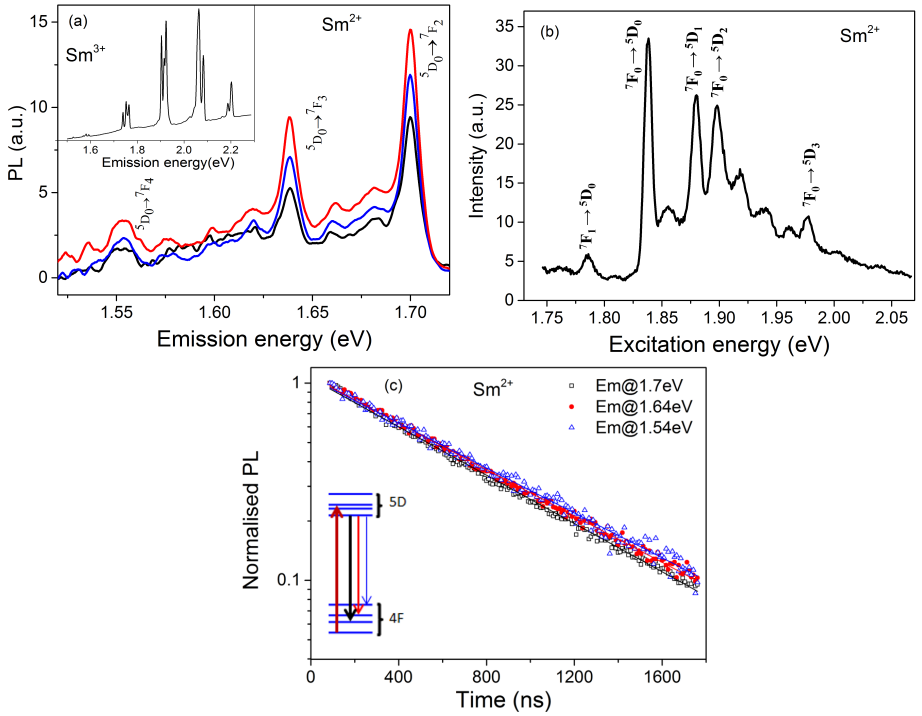

Figure 6.1: (a) Emission features of metastable Sm^{2+} in YPO_4: Ce, Sm, under 1.89 eV stimulation after 30, 45 and 60 minutes of X-ray irradiation (black, blue and red curves, respectively). The inset shows emission corresponding to Sm^{3+} in un-irradiated material, using 3.06 eV laser. (b) Excitation spectrum of Sm^{2+} in YPO_4: Ce, Sm after 3 hours of X-ray irradiation, recorded for emission fixed at 1.7 eV. (c) Time-resolved measurement of Sm^{2+} emissions under 1.89 eV laser stimulation, fitted with a single exponential function. The inset shows the relevant energy levels. All measurements are made at 7 K.

set shows the relevant excitation and emission energy levels. The data, when fitted with a single exponential function, yield lifetimes of (751 ± 16), (729 ± 11) and (704 ± 10) ns for the emission peaks at 1.54, 1.64 and1.70 eV respectively (corresponding to $^5D_0 \rightarrow {}^7F_{4,3,2}$). These lifetime estimates are consistent within 2σ uncertainty.

6.3.2 Temperature dependent luminescence properties of Sm^{2+}

The temperature dependence of the Sm^{2+} PL emission excited by the 1.89 eV laser is shown in Figure 6.2(a). This shows that the peaks at 1.70 eV and 1.64 eV ($^5D_0 \rightarrow {}^7F_{2,3}$) are broadened as the temperature is increased in the range of 100-300 K, and the peaks become rapidly quenched at temperatures higher than 130 K. This thermal quenching behaviour of Sm^{2+} has been reported before by Poolton et al. (2012); our data mimics the trend reported by these authors.

Thermal enhancement and thermal quenching of a signal can occur due to interplay of many different mechanisms (see for e.g. Pal et al., 2013). In comparison to PL intensity, the lifetime is a more robust parameter to understand thermal quenching due to a non-radiative pathway. Therefore, in order to accurately define the kinetics of thermal quenching in our signal we examined the lifetime dependence of Sm^{2+} on temperature.

Figure 6.2(b) shows the luminescence decay of the Sm^{2+} emission at 1.7 eV ($^5D_0 \rightarrow {}^7F_2$) at different temperatures, analysed in each case with single exponential function (after background subtraction). The average lifetime of the Sm^{2+} emission at 1.7 eV ($^5D_0 \rightarrow {}^7F_2$) in the temperature range 10-140 K yields (706 $\pm$ 5) ns, whereas at higher temperature the lifetime decreases very rapidly, being $\sim$ (98 $\pm$ 1) ns at 220 K. Figure 6.2(c) shows the temperature dependence of the integrated PL intensity for emission peaks between 1.69-1.72 eV (denoted as "1.7 eV") and the temperature dependence of the lifetime for the 1.7 eV emission peak. We note that the 1.625-1.65 eV (denoted as "1.64 eV") emission showed the same trend as 1.7 eV peak (not shown here for clarity).

The lifetime data show an excellent reproducibility (Figure 6.2(c)). The lifetime and the PL data show a broadly similar trend with temperature, suggesting that Mott-Seitz mechanism can explain the overall thermal quenching of the Sm^{2+} photoluminescence in the YPO_4: Ce, Sm system; in this mechanism, the increased probability of non-radiative relaxation pathway at higher temperature leads to a simultaneous reduction in signal intensity and a lower lifetime (e.g. Ueda et al., 2015, Pal et al. 2013, Calderon et al, 1990, Pagonis et al., 2010). We note that tunnelling loss through the SmA and SmB bands becomes detectable above 200 K (Fig. 5 of Poolton et al., 2012), and is, therefore, not likely to be responsible for the decreasing trend observed in our data up to at least

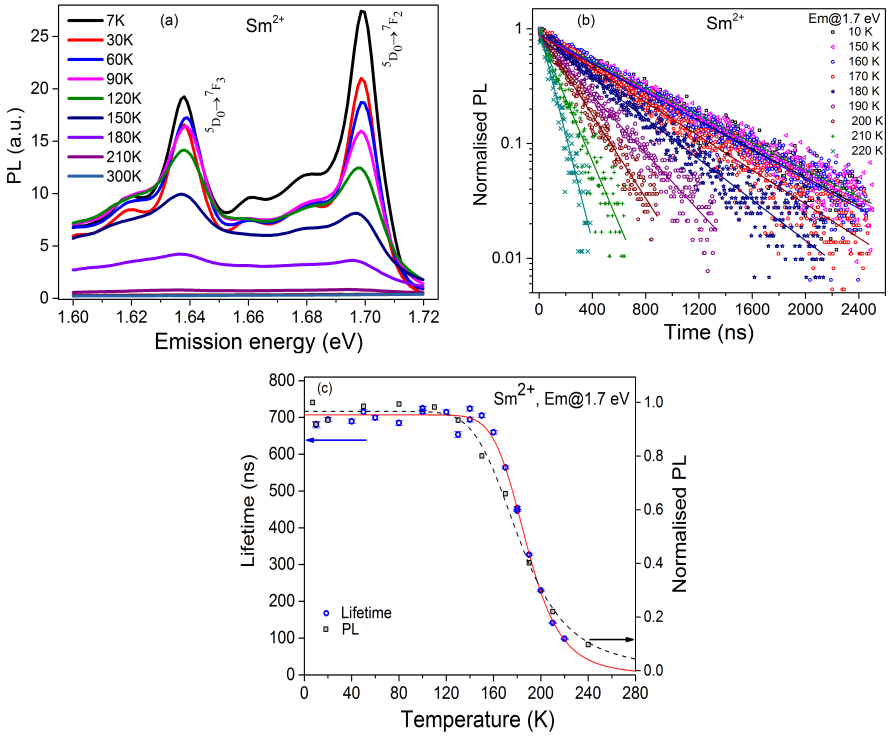

Figure 6.2: Temperature dependence of the Sm^{2+} emission under 1.89 eV laser excitation, after 3 hours of X-ray irradiation: (a) emission spectra, (b) Time-resolved measurements of $^5D_0 \rightarrow {}^7F_2$, transition at different temperatures, fitted with an exponential function, and (c) lifetime and integral PL intensity as a function of measurement temperature; the data are fitted with Equation 6.1 and 6.2, respectively (see text).

200 K. A slight deviation in the PL and lifetime data may originate due to thermal partitioning of electrons in the ground states (^7F multiplet) of the Sm^{2+}, which will vary with temperature and likely affect the PL intensity; but this effect will not alter the excited state lifetime.

Based on the Mott-Seitz mechanism, the temperature dependence of lifetime can be described by the following function (Pal et al. 2013; Calderon et al, 1990):

$$\frac{1}{\tau(T)} = \frac{1}{\tau_r} + \frac{1}{\tau_{nr}} \exp\left(\frac{-\Delta E}{kT}\right) \tag{6.1}$$

Where $\tau(T)$ is the measured temperature dependent lifetime, $1/\tau_r$ is probability of radiative transition, where τ_r corresponds to the measured lifetime before the onset of thermal quenching, $1/\tau_{nr}$ is the frequency factor for the non-radiative transition probability, ΔE is the threshold energy for non-radiative transition and k is Boltzmann's constant. The fitting of equation 6.1 to the lifetime data (Figure 6.2(c)) yielded a quenching energy of 0.20 ± 0.01 eV, $\tau_r = 706 \pm 5$ ns, and $1/\tau_{nr} = (5.4 \pm 1.8) \times 10^{11}$ s^{-1}.

Similarly, the reduction in the PL intensity with temperature can be analysed using the thermal quenching equation, which can be derived from Equation 6.1 (Chitambo et al., 2007).

$$I(T) = \frac{I(0)}{1 + C \exp\left(\frac{-\Delta E}{kT}\right)} \tag{6.2}$$

Here I(T) represents the integrated PL intensity at temperature T (K), I(0) is the intensity at absolute zero temperature; ΔE (eV) is the thermal quenching energy and k (eV.K^{-1}) is the Boltzmann's constant, and C is a constant equal to the ratio τ_n/τ_{nr} (Calderon et al., 1990; Pagonis et al., 2010; Chithambo et al., 2007). The fit for Equation 6.2 to the PL intensity data is shown as a dashed curve in Figure 6.2(c). This fit gives slightly different values than those derived from the lifetime data ($\Delta E = 0.14 \pm 0.01$ eV; C= $(6.1 \pm 4.7) \times 10^3$; note that the value of C derived from the best fit to the lifetime data is 3.8×10^5. Because of the reasons discussed before, i.e. that the possible effect of thermal partitioning in the ground states on the PL intensity, we consider the lifetime data to be a more reliable indicator of the thermal quenching kinetics; thus we conclude that the threshold for non-radiative transition for $^5D_0$ state of Sm^{2+} in YPO_4 is ~ 0.20 eV.

6.3.3 Optically induced tunnelling luminescence

As mentioned earlier, electrons from excited states of Sm^{2+} (SmA and SmB bands); can transfer via tunnelling to the Ce^{4+} centre, resulting in Ce^{3+} emission; although this mechanism has been used earlier to characterise the Sm^{2+} defect (Bos et al., 2010; Poolton et al., 2012), the kinetics of the optically induced charge transfer process have not been explored before. After irradiating the sample with X-rays, we excited Sm^{2+} with

1.89 eV laser at room temperature and measured the resulting luminescence signal from the Ce^{3+} emission (with U340 filters). Figure 6.3(a) shows the OSL emission spectrum resulting from this process. As expected this emission grows with X-ray irradiation time due to increased concentrations of Sm^{2+} and Ce^{4+}. The characteristic 5d-4f emission doublet of Ce^{3+} is clearly observed at 3.47 eV and 3.73 eV; this arises from the $^5d_1 \rightarrow {}^2F_{7/2,5/2}$ transitions (Laroche et al, 2001).

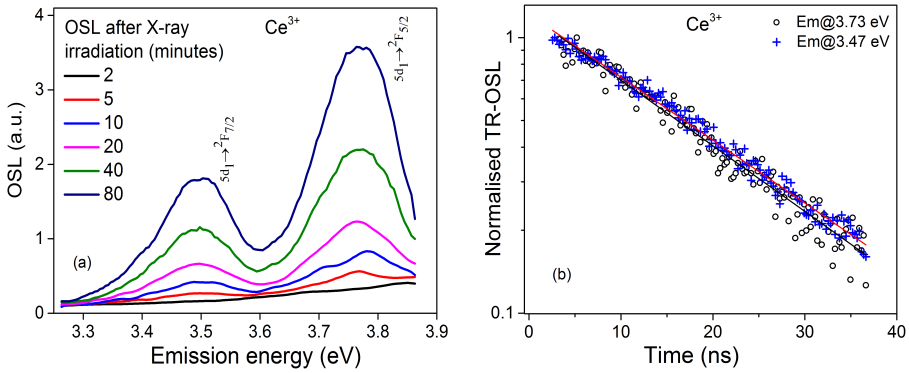

Figure 6.3: Characteristics of optically stimulated luminescence emission arising from excited state tunnelling from the metastable Ce^{3+} to Ce^{4+} states. The signals detected using Sm^{2+} emission (U340 transmission band) are produced by electron-hole recombination at the Ce^{4+}center. The data are recorded at room temperature under 1.89 eV laser excitation. (a) OSL emission spectra produced after different X-ray irradiation durations (or dose), and (b) Time-resolved OSL emissions (at 3.47 and 3.73 eV) fitted with a single exponential function.

To understand the dynamics of the optically induced tunnelling process, we made Time-Resolved OSL (TR-OSL) measurements using 1.89 eV laser excitation for both the emissions, i.e. 3.47 eV and 3.73 eV. Figure 6.3(b) shows the obtained TR-OSL data which show an exponential decay. These data were fitted with a single exponential function, yielding lifetimes 19.4 ± 0.1 ns and 19.2 ± 0.6 ns for 3.47 eV and 3.73 eV emission peaks, respectively. These lifetimes correspond well with the published lifetime of Ce^{3+} excited state (Laroche et al., 2001) which was 23 ns. Interestingly, the predicted $^5D_0$ excited state lifetime of Sm^{2+} at room temperature is about 7 ns based on the parameters derived from Equation 6.1, implying that the $^5D_0$ could potentially be feeding to the tunnelling active states (SmA and SmB bands) and thereby Ce^{4+}, while the Ce^{3+} excited state relaxation is ongoing; this process could give rise to an ini-

tial non-exponentially (peak shape) in the TR-OSL. However, based on our TR-OSL data, it can be inferred that both the $^5D_0$ and the tunnelling active states in the Sm^{2+} must empty very rapidly (at least an order of magnitude faster than the Ce^{3+} relaxation rate) at room temperature so as to give clean single exponential decay representative of Ce^{3+}. Thus, at room temperature there must be much faster emptying of the $^5D_0$ state (possibly to the tunnelling bands) than that predicted by thermal quenching model, and an insignificant retrapping from the tunnelling active states to the $^5D_0$ state.

Since the excitation with 1.89 eV is sub-conduction band, the only mechanism of charge transfer is tunnelling from Sm^{2+} excited state to Ce^{4+}. Understanding the excited state tunnelling process is of interest in order to understand the behaviour of both artificial and natural dosimeters (e.g. see Jain et al., 2012). However, this understanding is usually hampered by complexity of the materials of interest. For example, decades of research has been devoted to tackling the anomalous fading problem in feldspars, which arises due to tunnelling loss from the dosimetric trap (see Jain and Ankjærgaard, 2011 for a comprehensive discussion). Our model YPO_4: Ce, Sm gives us an opportunity to isolate the excited state tunnelling process and use it to test our theoretical understanding of tunnelling in randomly distributed defects. With this objective we measured the CW-OSL using the 1.89 eV laser excitation after different X-ray irradiation durations. Figure 6.4(a) shows the CW-OSL decay curves recorded using a separate PMT with U340 filters; the corresponding emission spectra are plotted in Figure 6.3(a).

The truncated-distribution tunnelling OSL model of Jain et al (2015) predicts that the shape of the OSL decay curve should depend both on the hole density (e.g. due to increasing dose), and on the truncation of the nearest neighbour distribution (e.g. due to prior heating or ground state tunnelling). We apply their model equation to our data in Figure 6.4(a) obtained after different X-ray irradiation times:

$$OSL \propto -\frac{dn}{dt} = 3n_0\rho' z(t')^{-1}[\ln(t'b) - \xi]^2 \exp(-\rho'[\ln(t'b) - \xi]^3) \quad (6.3)$$

Here n is the instantaneous, n_0 the initial trapped electron concentration, ρ' is the number density of the trapped holes, b $[s^{-14}]$ is the attempt to tunnel frequency, ρ is a variable, which is a linear function

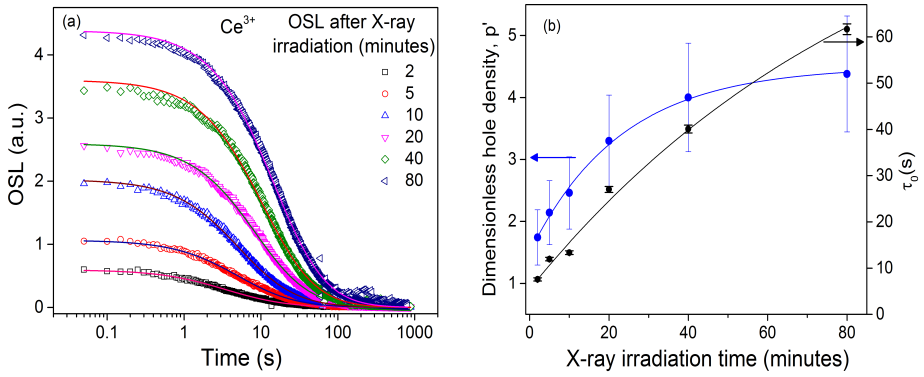

Figure 6.4: (a) Tunnelling OSL decay curves produced after different X-ray irradiation durations (or dose); these data are fitted with the truncated distribution tunnelling model (Equation 6.3), (b) Dimensionless hole density (ρ') and the truncation parameter τ_0 derived from fitting of OSL decay curves in Figure 6.4(a) to Equation 6.3, plotted as a function of X-ray irradiation duration (see text).

of time $(\tau_0 + zt)$, $\xi = \ln(\frac{s}{p})$, where s is frequency factor and p is optical excitation probability per unit time. The Equation 6.3 fits well to all the OSL curves in Figure 6.4(a) confirming that the excited state tunneling model describes well the observed OSL signal produced by localized recombination.Two fitting parameters that deserve closer scrutiny here are the dimensionless hole ρ', which should increase with dose, and the truncation parameter (τ_0) which should increase with irradiation time because of ground state tunneling. Both these parameters are plotted in Figure 6.4(b); their trend with X-ray irradiation time (or dose) confirms the model predictions (Equation 6.3).

6.4 Conclusion

Using low temperatures and sub-conduction-band excitation, new details of the metastable defects in co-doped, X-ray irradiated YPO_4: Ce, Sm have been measured. These include resolving the excited states of Sm^{2+} by intra-defect transitions, measurement of the excited state lifetimes of Sm^{2+} (temperature dependent) and Ce^{3+}, and dynamics of the optically induced excited-state tunnelling pathway from $Sm^{2+} \rightarrow Ce^{4+}$. The methods are ideal for exploring metastable states in other lanthanide co-doped wide band-gap materials, and for understanding charge recom-

bination processes in complex natural dosimeters such as feldspars.

6.5 Acknowledgment

Prof. A. J. J. Bos is thanked for providing YPO_4: Ce, Sm sample and Dr. N. R. J. Poolton is thanked for participation during the various stages of this study. Dr. Torben Lapp is thanked for his support in the commissioning of low temperature facility.

Bibliography

[1] Bos, A. J. J., Dorenbos, P., Bessière, A, Viana, B. (2008). Lanthanide energy levels in YPO4. Radiation Measurements 43, 222 – 226.

[2] Bos, A. J. J., Poolton, N. R. J., Wallinga, J., Bessière, A., Dorenbos, P. (2010). Energy levels in YPO+4:Ce^{3+}, Sm^{3+} studied by thermally and optically stimulated luminescence. Radiat. Meas. 45, 343-346.

[3] Calderon, T, Millan, Jaquet, F., Sole, G., J. (1990). Optical properties of Sm^{2+} and Eu^{2+} in natural fluorite crystals. Nucl. Tracks Radiat. Meas.,17, 557-561.

[4] Chakrabarti, K., Mathur, V.K., Thomas, L.A., Abbundi, R.J. (1989). Charge trapping and mechanism of stimulated luminescence in CaS: Ce; Eu. J. Appl. Phys. 65, 2021–2023.

[5] Chithambo, M.L. (2007). The analysis of time-resolved optically stimulated luminescence. II: Computer Simulations and Experimental Results. J. Phys. D.: Appl. Phys. 40, 1880-1889.

[6] Dorenbos, P. (2003). Systematic behaviour in trivalent lanthanide charge transfer energies J. Phys.: Condens. Matter 15, 8417–843.

[7] Dorenbos, P., Bos, A. J. J., Poolton, N. R. J. (2011). Electron transfer processes in double lanthanide activated YPO_4, Optical Materials 33, 1019–1023.

[8] Ding, D., Pereira, L. M. C., Bauters, J. F., Heck, M.J. R., Welker, G., Vantomme, A., Bowers, J. E., Dood, M.J. A., Bouwmeester, D.(2016). Multidimensional Purcell effect in an ytterbium-doped ring resonator. Nature Photonics 10, 385–388.

[9] Dobrowolska, A., Bos, A. J. J., Dorenbos, P. (2014). Electron tunnelling phenomena in YPO_4: Ce, Ln (Ln= Er, Ho, Nd, Dy). Journal of Physics D: Applied Physics 47, 33.

[10] Hölsa, J., Jungner, H., Lastusaari, M., Niittykoski, J. (2001). Persistent luminescence of Eu^{2+} doped alkaline earth aluminates, MAl2O4: Eu^{2+}. J. Alloys Compd. 323, 326–330.

[11] Jain, M., Sohbati, R., Guralnik, B., Murray, A., Kook, M., Lapp, T., Prasad, A.K., Thomsen, K.J., Buylaert, P. (2015). Kinetics of infrared stimulated luminescence from feldspars. Radiat. Meas. 81, 16-22.

[12] Jain, M., and Ankjærgaard, C. (2011). Towards a non-fading signal in feldspar: Insight into charge transport and tunnelling from time-resolved optically stimulated luminescence. Radiation Measurements, 46, 292–309.

[13] Jain, M., Guralnik, B., Andersen, M. T. (2012). Stimulated luminescence emission from localized recombination in randomly distributed defects. Journal of physics: Condensed matter 24, 385402.

[14] Laroche, M., Girard, S., Margerie, J. Moncorge, J., Bettinelli, M., Cavalli,E.(2001). Experimental and theoretical investigation of the $4f^n \leftrightarrow 4f^{n-1}5d$ transitions in YPO_4 :Pr^{3+} and YPO_4 :Pr^{3+}, Ce^{3+}. J. Phys.: Condens. Matter, 13, 765–776.

[15] Meijerink, A., Schipper, W.J., Blasse, G. (1991). Photostimulated luminescence and thermally stimulated luminescence of Y2SiO5 : Ce^{3+}, Sm^{3+}. J. Phys. D: Appl. Phys. 24, 997–1002.

[16] Mandowski, A., Bos, A. J. J. (2011). Explanation of anomalous heating rate dependence of thermoluminescence in YPO_4:Ce^{3+}, Sm^{3+} based on the semi-localized transition (SLT) model Radiation Measurements 46 1376-1379.

[17] Matsuzawa, T., Aoki, Y., Takeuchi, N., Murayama, Y. (1996). New long phosphorescence phosphor with high brightness, $SrAl_2O_4$: Eu^{2+}, Dy^{3+}. J. Electrochem. Soc. 143, 2670–2673.

[18] Pal, P., Penhouët, T., D'Anna ,V., Hagemann, H.(2013). Effect of temperature and pressure on emission lifetime of Sm^{2+} ion doped in MFX (M=Sr, Ba; X=Br, I) crystals. J. Lumin., 142, 66–74.

[19] Pieterson, L. V., Reid, M. F., Burdick, G. W., and Meijerink , A.(2001). 4fn $\leftrightarrow$ 4fn-15d transitions of the light lanthanides: Experiment and theory. Phys. Rev. B 65, 045113.

[20] Poolton, N. R. J., Bos, A. J. J., Dorenbos, P. (2012). Luminescence emission from metastable Sm^{2+} defects in YPO_4: Ce, Sm.J. Phys.: Condens. Matter 24,225502.

[21] Poolton, N. R. J., Bos, A. J. J., Jones, G.O., Dorenbos, P. (2010). Probing electron transfer processes in YPO_4: Ce, Sm by combined synchrotron–laser excitation spectroscopy. J. Phys.: Condens. Matter 22, 185403.

[22] Pagonis, V., Ankjærgaard, C., Murray, A., Jain, M., Chen, R., Lawless, J., Greilich, S. (2010). Modelling the thermal quenching mechanism in quartz based on time-resolved optically stimulated luminescence. Journal of Luminescence, 130(5), 902-909.

[23] Schulman, J.H., Ginther, R.J., Klick, C.C., Alger, R.S., Levy, R.A. (1951). Dosimetry of X-rays and gamma-rays by radiophotoluminescence. J. Appl. Phys. 22, 1479-1487.

[24] Thiel, C.W., Sun, Y., Cone, R.L. (2002). Progress in relating rare-earth ion 4f and 5d energy levels to host bands in optical materials for hole burning, quantum information and phosphors. J. Mod. Opt. 49, 2399–2411.

[25] Ueda, J., Dorenbos, P., Bos, A. J. J., Meijerink, A., Tanabe, S. (2015). Insight into the Thermal Quenching Mechanism for $Y_3Al_5O_{12}$: Ce^{3+} through Thermoluminescence Excitation Spectroscopy. J. Phys. Chem. C, 119, 25003-25008.

Chapter 7

Optical dating in a new light: A direct, non-destructive probe of trapped electrons

A. K. Prasad[1], N. R. J. Poolton[1], M. Kook[1], M. Jain[1]

[1] *Center for Nuclear Technologies, Technical University of Denmark DTU Risø Campus, Roskilde-4000, Denmark*

Accepted in: Scientific Reports - Nature

Abstract: Optically stimulated luminescence (OSL) dating of quartz and feldspar minerals is widely used in Quaternary geochronology for understanding climate changes, landscape development, human evolution, and dispersal; feldspar in particular covers an age range from a few tens of years to about 0.5 million years (Ma). OSL is derived from the optical eviction of trapped electrons in the lattice followed by radiative recombination with the trapped holes elsewhere; detection is in the anti-Stokes energy. In this study we present for the first time a new method of optically reading the trapped electron population in feldspar. This method is based on excitation with near infra-red photons (around

1.4 eV) and detecting the internal radiative relaxation (a Stoke-shifted emission) within the dosimetric trap itself, thus producing an Infra-Red Photo-Luminescence (IRPL) signal. We investigate the physical characteristics of the new IRPL signal through low temperature (7-295 K) investigations, and demonstrate the potential of using it for optical dating. Our results herald that this signal does not suffer from anomalous fading, and the ease and simplicity of its measurement will provide a firm basis for routine accurate dating for ages up to $\sim$ 0.5 Ma.

7.1 Introduction

Geochronology based on optical methods is an important area contributing to the understanding of past climate, environments, landscape development and human evolution and dispersal in the last 0.5 Ma (Roberts et al. 2015, Roberts and Lian et al. 2015, Rhodes, 2011). Optically stimulated luminescence (OSL) dating, also known as optical dating, was first proposed and demonstrated by Huntley et al. (1985), and uses the light-sensitive electron traps in commonly available minerals on Earth's crust such as quartz and feldspars. The OSL (or, when Infrared light is specifically used for stimulation, IRSL) signal intensity in these minerals is a function of the population of the trapped charge within the crystal lattice, which in turn is a function of how long the crystal was exposed to ionising radiation since its deposition in a sediment layer. In practice, OSL dating involves separation of quartz and feldspars from the sediment sample, followed by stimulation of quartz with blue light ($\sim$ (470 $\pm$ 30) nm), and feldspar with near infrared light ($\sim$ (870 $\pm$ 40) nm) to obtain the OSL and IRSL respectively (e.g., Bøtter-Jensen et al., 2010). These signals are then calibrated into absorbed dose from ionising radiations (Unit Gy= J/Kg), by building a luminescence dose-response curve using a laboratory beta (^{90}Sr/^{90}Y) source. Age is calculated by dividing the absorbed dose by the annual dose rate; the latter is estimated through the assay of radioactivity in the sediment and cosmic ray influx at the site.

The fundamental mechanism of the OSL or IRSL dating technique is eviction of trapped electrons by optical excitation, and subsequent radiative recombination of these electrons with trapped holes in the crystal. Figure 7.1(a) illustrates the accepted mechanism of IRSL production in a feldspar (see Jain and Ankjærgaard, 2011); infrared light excites

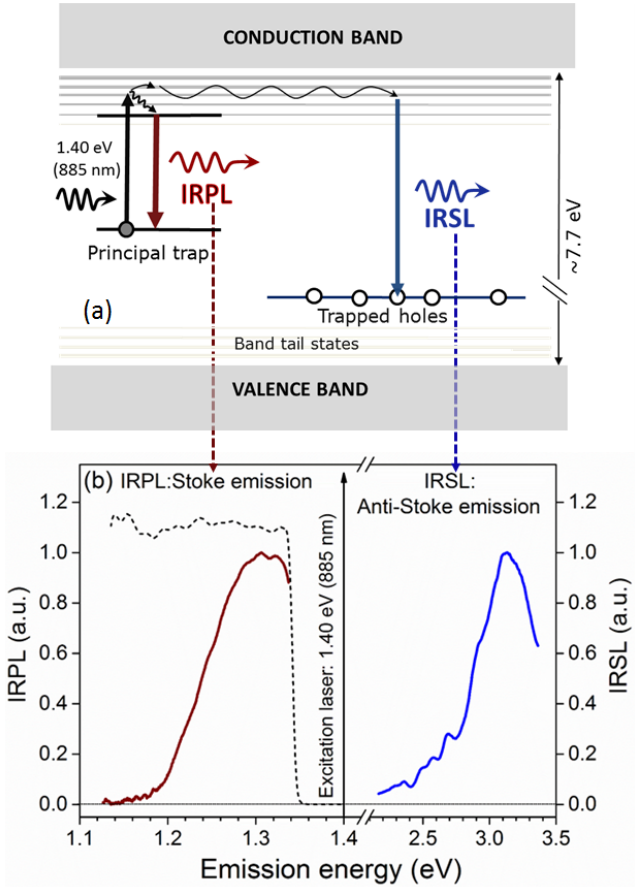

Figure 7.1: (a) A schematic showing the mechanism of IRPL and IRSL generation in feldspar. (b) IRPL and IRSL emission spectra at 295 K of irradiated sedimentary K-feldspar R47 sample on exposure to 885 nm (1.4 eV) laser light.The dotted curve represents the transmission of the long- pass interference filter used for IRPL detection.

trapped electron to a higher energy state within the IR dosimetric trap, followed by diffusion within the band tail states and radiative recombination with a hole trapped elsewhere in the lattice. This mechanism implies that OSL/IRSL readout destroys the chronometric/dosimetric information (trapped electrons and holes) stored in the crystal. In other words, OSL/IRSL is a destructive technique by default, as readout affects the existing electronic (metastable) state of the crystal. This inherent destructive aspect of OSL/IRSL measurement requires that the luminescence readout be as efficient as possible (since the signal can be measured only once), and that any irreversible (sensitivity) changes between the readout of the natural and the laboratory generated OSL/IRSL signals are corrected for. In contrast, an alternative trapped charge dating technique, electron-spin-resonance (ESR), can directly read the trapped electrons in a non-destructive manner; however, the ESR dating method has had a restricted application in sediment dating because of the difficulty of optical zeroing of the signal prior to burial (Grün et al., 1989). Furthermore, ESR dating method is not applicable to feldspar because of the lack of a readily identifiable dosimetric signal.

Feldspars are particularly attractive for geochronometry since they have a more extended dating range compared to quartz. For the typical dose rate in nature ($\sim$ 2 Gy/ka), the trap reservoir that gives rise to IRSL in feldspar saturates at $>$ 0.5 Ma compared to only about 0.1 Ma in quartz. However, historically, this potential of IRSL has not been exploited because of the loss of trapped charge with time due to quantum mechanical tunnelling, a process commonly referred to as anomalous fading (Wintle, 1973); this prompt loss of trapped electrons gives rise to age underestimation. In recent years, this problem has been tackled with some success by selectively sampling only the distant electron-hole populations, generating IRSL signals which are less likely to fade in nature (Tsukamoto et al. 2006; Thomsen et al., 2008; Jain and Ankjærgaard, 2011; Buylaert et al., 2009, 2012; Li and Li, 2011). Although these post IR- IRSL (pIR-IRSL) or pulsed IRSL (PIRSL) signals are significantly more stable than IRSL, it is still debated whether they are completely stable on geological time scales or not (Jain et al. 2015b; Buylaert et al. 2012). Furthermore, pIR-IRSL signals do not reset as rapidly as IRSL on exposure to daylight and the technique suffers from undesirable effects such as thermal transfer because of heating and optical stimulations at high temperatures (e.g. 290 °C). Pulsed IRSL signals do not suffer from

the problems of bleachability or thermal transfer (Jain et al., 2015b); however, signal sensitivity is an issue here since more than 90 % of the signal is deliberately rejected in the readout.

Given the inherent potential of feldspar dating in extending the dating age range, it is imperative to explore new methods that do not suffer from the above problems. Models of IRSL in feldspar suggest that there is a significant relaxation of the electrons from the excited to the ground state of the dosimetric trap subsequent to removal of the excitation light, and that this process must dominate in the distant electron hole pairs (Jain and Ankjærgaard, 2011; Jain et al. 2015a). Similarly, work on IR radio-fluorescence (luminescence emitted during exposure to a source of ionizing radiation; IR- RF) suggests that the NIR emission ($\sim$ 865 nm) arises from a radiative transition during the trapping of electrons from the conduction band to the dosimetric trap (Trautmann et al., 1999). Combining the observations of IR-RF with the IRSL model suggests that during IR excitation there should be a luminescence emission corresponding to the radiative relaxation of electrons from the excited to the ground state of the IR trap (dosimetric trap). Such a signal for example has been shown in model systems (analogues to feldspar) such as YPO_4: Ce, Sm where it is indeed possible to measure dose-dependent, but time-stable luminescence by monitoring radiative relaxation within the metastable Sm^{2+} (the electron trap) (Poolton et al. 2012; Prasad et al., 2016b). With this background, we explore for the first time the Stokes shifted NIR signals in feldspar, produced from radiative relaxation within the IR dosimetric trap, after the samples have been exposed to ionizing radiation. We demonstrate that the new signal a) arises from the same dosimetric IR trap as IRSL, b) is a steady state, i.e. it can be measured non-destructively, and c) it may be used to measure natural doses accurately without any correction for anomalous fading.

7.2 Experimental section

7.2.1 Samples

A range of natural sedimentary and museum single crystal feldspar material was used, as summarized in Table 7.1. The feldspars themselves fall into the two common ranges; alkali $(K_x,Na_{1-x})AlSi_3O_8$ and plagioclase $Na_{1-x}Ca_xAl_{1+x}Si_{3-x}$ O_8 Sample compositions given are for the bulk, and take no account of potential phase segregation on the micro-scale;

they were determined by XRF analysis using XRF attached with Risø TL/OSL reader. The error in individual K, Na, Ca chemical content is ± 0.01.

7.2.2 Methods

All the low temperature measurements were made using the Risø station for CryOgenic LUminescence Research (COLUR) at DTU Nutech. This facility consists of a Horiba Fluorolog-3 spectrofluorometer, upgraded to include: a temperature controlled (7-300 K) closed-loop cryostat, an in-situ X-ray irradiation facility (40 kV, 100 µA) copper anode with 3 ms action X-ray shutter), and multiple ports for laser excitation and photo-detection for use in a number of dual probe type experiments. The sample is attached directly to the cryostat cold finger and measured under vacuum (2.5×10^{-5} mB).

Emission spectra from 910 to 1100 nm after different X-ray irradiations were measured by excitation with 885 nm (1.4 eV), 500 mW laser and detection with Jobin-Yvon HR-320 spectrometer (300 lines/ mm grating) coupled to a liquid nitrogen cooled CCD detector.

Excitation spectra were measured using a combination of 450 W Xe lamp and, for longer wavelengths, a 20 W tungsten halogen lamp (for longer wavelengths). The excitation wavelength was selected using a double grating Czerny-Turner monochromator while the detection was made with the same CCD system as above, but with a 925 nm long pass filter (OD:4) to avoid any second order and scattered light. Luminescence lifetime measurements were measured using a time-correlated single photon counting (TCSPC) and an 842 nm (1.47 eV) laser diode excitation. The laser has a maximum power of 90 mW, and works in either CW mode or can be modulated with rise/fall times of < 18 ns; it was controlled via Horiba spectrometer software.

All the dosimetric measurements were carried out using the Risø TL/OSL reader (for details see; Bøtter-Jensen et al., 2010, Lapp et al., 2015). All beta dose dependent IRPL measurements at room temperature were made with a Risø TL/OSL DA-20 reader with spectrometer attachment (Prasad et al., 2016a). It consists of a fibre-coupled Shamrock 193i spectrograph attached to an EMCCD (iXon Ultra 888). The signal is collected through a fibre bundle (consist of 114 fibers with 200 µm diameter), which is assembled to form a circle of 3 mm diameter towards the sample side and a rectangle towards the spectrometer side. To measure

Table 7.1: Protocol used for the laboratory bleaching experiment

Step-1:	Illumination with blue light (72 mW/cm^2) at 450 °C for 100 s
Step-2:	IRPL (885 nm laser exposure at room temperature for 250 s)
Step-3:	Beta irradiation (700 Gy, 2000 s beta irradiation)
Step-4:	Preheat - 250 °C for 60 s
Step-5:	IRPL (885 nm laser exposure at room temperature for 250 s)
Step-6:	Blue light exposure at temperature (T= 25 to 450 °C) for 100 s
Step-7:	IRPL (885 nm laser exposure at room temperature for 250 s)

Table 7.2: The IRPL SAR protocol

Step-1:	Preheat (250 °C for 60 s)
Step-2:	IRPL (885 nm laser exposure at room temperature for 250 s)- **IRPL, Lx, Ln**
Step-3:	Bleaching (blue light -300 °C for 100 s)
Step-4:	Test dose (350 Gy, 1000 s beta irradiation)
Step-5:	Preheat (250 °C for 60 s)
Step-6:	IRPL (885 nm laser exposure at room temperature for 250 s)- **IRPL, Tx, Tn**
Step-7:	Bleaching (blue light -300 °C for 100 s)
Step-8:	Regeneration dose and repeat Step-1

the dose dependent IRPL, the sample was mounted into a steel cup and placed in the sample wheel of Risø TL/OSL Reader, the irradiation of the samples was achieved with ^{90}Sr/^{90}Y β source (dose-rate 0.35 Gy/s). The IRPL spectra were recorded by excitation with a 885 nm laser and detection from 920 nm to 1050 nm by setting the 300 lines/mm grating. A band pass interference filter at 875 nm (FWHM: 25 nm) was set at the excitation side and a long pass filter with 925 nm (OD:4) was set at the detector side.

The measurement protocols related to characterising the dosimetric behaviour of the samples are summarised in Table 7.1 to Table 7.3.

Table 7.3: The dual IRSL-IRPL SAR protocol

Step-1:	Preheat (250 °C for 60 s)
Step-2:	IRSL at room temperature for 50 s - IRSL: Lx, Ln
Step-3:	IRPL (885 nm laser exposure at room temperature for 250 s) - IRPL, Lx, Ln
Step-4:	Bleaching (blue light -300 °C for 100 s)
Step-5:	Test dose (350 Gy,1000 s beta irradiation)
Step-6:	Preheat (250 °C for 60 s)
Step-7:	IRSL at room temperature for 50 second - IRSL: Tx, Tn
Step-8:	IRPL (885 nm laser exposure at room temperature for 250 s) - IRPL, Tx, Tn
Step-9:	Bleaching (blue light -300 °C for 100 s)
Step-10:	Regeneration dose and repeat Step 1.

7.3 Results and discussion

7.3.1 Internal transition in the IR dosimetric trap: IR Photoluminescence (IRPL)

The IR dosimetric trap in feldspar shows a resonance peak around 1.45 eV, first observed by Hütt et al. (1988). A detailed survey of this peak on a variety of samples has shown that the excitation spectrum consists of two to three overlapping peaks (e.g. Baril and Huntley, 2003a). The temperature dependence of this peak (Poolton et al., 2009; Andersen et al., 2012) suggests that the electron-hole recombination is mediated through the band tail states, and a single electron trap gives rise to the IRSL signal. The emissions corresponding to IR ($\sim$ 1.45 eV) excitation have been reported to be in the UV ($\sim$ 3.76 eV), UV-Violet ($\sim$ 3.13 eV), green-orange ($\sim$ 2.18 eV) and red ($\sim$ 1.71 eV) bands (Krbetschek et al. 1997, Baril and Huntley, 2003b), with the UV-Violet being the most commonly used emission in IRSL dating. Notably, all these emissions occur in the anti-Stokes mode (emission energy > excitation energy); there exist no investigations of possible Stokes shifted emissions (emission energy < excitation energy) within the IR dosimetric trap, which is the subject of this study.

To explore the existence of dosimetric, Stokes-shifted emission in feldspar, we selected a typical sedimentary K-feldspar sample (R47, see Table 7.1) that exhibits a bright IRSL. After receiving an X-ray dose for 2 hours, we excited this sample with a laser emitting at 1.4 eV (885 nm). This energy is near the peak of the IRSL resonance typically found

in feldspar. Figure 7.1(b) shows the presence of a strong Stokes-shifted emission at 295 K, peaking at 1.3 eV (955 nm). Briefly, the spectrum is measured with a CCD coupled to a spectrograph with a sharp-cut long-pass filter at 925 nm being used to block the scattered laser light; for full experimental details, see Methods Section 7.2.2. Also shown in Figure 7.1(b) is the anti-Stokes IRSL emission spectrum at 295 K from the same sample, and its mechanism is represented in the Figure 7.1(a); this spectrum is similar to those reported in earlier studies (e.g. Baril and Huntley, 2003b) and consists of a dominant broad band in the near UV/violet, peaking at 3.1 eV.

In order to examine the characteristics of this new Stokes shifted signal, we measured its excitation spectrum while fixing the emission window at 955 nm (1.3 eV), as shown in Figure 7.2(a). For comparison, we also measured the IRSL excitation spectrum while fixing the emission in the UV window using the U340 filter (centre wavelength: 340 nm, FWHM:85 nm). The two excitation spectra are similar: peak fitting gives two components (1.45 and 1.49 eV) in the Stokes shifted emission and three components (1.42, 1.45 and 1.55 eV) in the IRSL emission. There is an overlap in the main resonance peak at 1.45 eV in both the spectra, strongly suggesting that the two signals are arising from the same trap.

To confirm that the new Stokes shifted signal contains dosimetric information, its signal intensity was measured as a function of X-ray duration. The data are shown in Figure 7.2(b); there is a systematic increase in the signal intensity with prior dose, but the emission spectrum itself does not show any shift in the peak position with dose.

Based on the excitation and dosimetric characteristics shown in Figure 7.2, we interpret this new Stokes shifted photoluminescence signal to arise from resonant (IR) excitation of the trapped electron within the IR dosimetric trap, followed by radiative relaxation from the excited state to the ground state (Figure 7.1(a) and 7.1(b), left side). The signal intensity increases with irradiation dose because of an increase in the trapped electron population. We name this Stoke's shifted emission as the IR PhotoLuminescence (IRPL) signal. In literature, such an emission mechanism is commonly referred to as radio-photoluminescence (Schulman et al., 1951), however, because of the potential confusion with radio luminescence in IR wavelength range in feldspar (e.g. Lapp et al., 2012, Krbetschek et al., 2000), we have chosen to remove the prefix 'radio' from

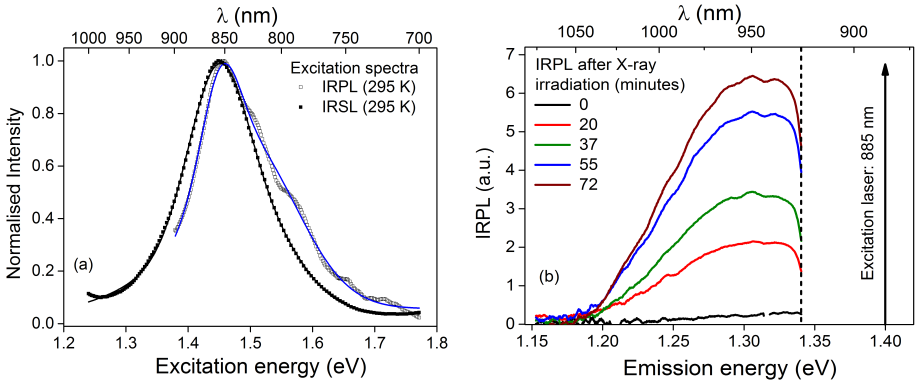

Figure 7.2: (a) A comparison of IRPL and IRSL excitation spectra for R47 at 295 K: solid curves are best fits to the data, with parameters given in Table 7.5. (b) X-ray dose dependent IRPL spectra from sample R47 at 295 K using 1.4 eV (885 nm) stimulation. The vertical dashed line indicates the sharp-cut off long pass filter cut-on, needed to block the scattered laser light.

radio-photoluminescence.

In the following we further explore the physics and the dosimetric behavior of the IRPL.

7.3.2 Low temperature investigations for IRPL mechanism

In this section, we report on the low temperature characteristics of IRSL and IRPL to understand the details of the IRPL mechanism. The sample R47 was first bleached under SOL simulator for 48 hours, then mounted on the cold finger of a cryostat and gives in-situ X-irradiation; at 7 K. For full experimental details, see the Methods Section 7.2.2.

Figure 7.3(a) shows the IRSL excitation spectra measured at295 K and 7 K using the UV emission passed by a U340 filter. At 295 K we observe a broad peak at 867 nm (1.43 eV); peak fitting in the excitation energy range 1.25-1.78 eV shows three overlapping bands at 1.43 eV, 1.45 eV, and 1.55 eV. There is a drastic reduction in the intensity at 7 K compared to that at room temperature, in agreement with the data published by Poolton et al. (2009). Figure 7.3(b) shows the excitation spectrum of IRPL for the 955 nm (1.3 eV) emission at 7 K and 295 K; the IRPL signal shows the opposite effect compared to IRSL, i.e., the peak intensity at 1.45 eV increases with lowering the temperature. The IRPL

excitation spectrum has broad resonance features at 1.45 eV and 2.1 eV. The low energy peak represents the excited state resonance in the IR dosimetric trap; Gaussian fitting of the 7 K data shows components peaks at 1.39 eV, 1.46 eV (main) and 1.53 eV. The 2.1 eV peak could potentially represent the conduction band transition; the reduction in peak intensity after 2.1 eV is likely due to an increase in the probability of electron-hole recombination (IRSL) relative to the probability of retrapping (IRPL).

Figure 7.3(c) shows the comparison of the IRPL emission spectra measured at 7 K and 295 K using the CCD detector and the resonance excitation at 1.4 eV. The emission intensity increases by about 30% by lowering the temperature from the 295 K to 7 K, and the emission spectrum becomes narrower. Peak fitting of the 7 K, IRPL emission shows two overlapping bands peaking at 1.26 eV and 1.31 eV.

These spectroscopic observations confirm our conceptual model of IRSL and IRPL production (Figure 7.1(a)). The temperature dependent IRSL excitation spectra shown by Poolton et al. (2009) and Andersen et al. (2012) suggest that majority of IRSL is generated by electron diffusion within the band tail states (e.g. Poolton et al., 2002, Morthekai et.al, 2012); the large reduction in the IRSL intensity at 7 K occurs because of freezing of electron transport in the band tail states. The minor IRSL emission observed at 7 K in Figure 7.3(a) most likely results from direct tunneling from the excited state of the IR dosimetric trap to the recombination center (Poolton et al., 2009). In contrast to the IRSL, the IRPL signal arises from the internal transition within the IR dosimetric trap (excited $\rightarrow$ ground state); therefore, the signal is enhanced at low temperature due to a combination of reduced loss of electrons from the excited state to the band tail states and possible reduced thermal quenching within the centre.

Figure 7.3(d) examines the dosimetric behavior of the IRPL signal at 7 K. The IRPL intensity increases with X-ray irradiation time and, as with the room temperature measurements (Figure 7.2(b)), the spectra show neither a change in spectral shape nor a shift in peak energy with dose; the only difference between measurements made at 295 K and 7 K is the narrowing of the IRPL peak at 7 K. The inset to Figure 7.3(d) shows the dose response curve (integrated peak signal vs. the X-ray irradiation time) fitted with single saturating exponential growth function.

We further investigated the stability of the signal when probed with the IR laser at 7 K, 77 K and 295 K. After X-ray irradiation at 7 K, the

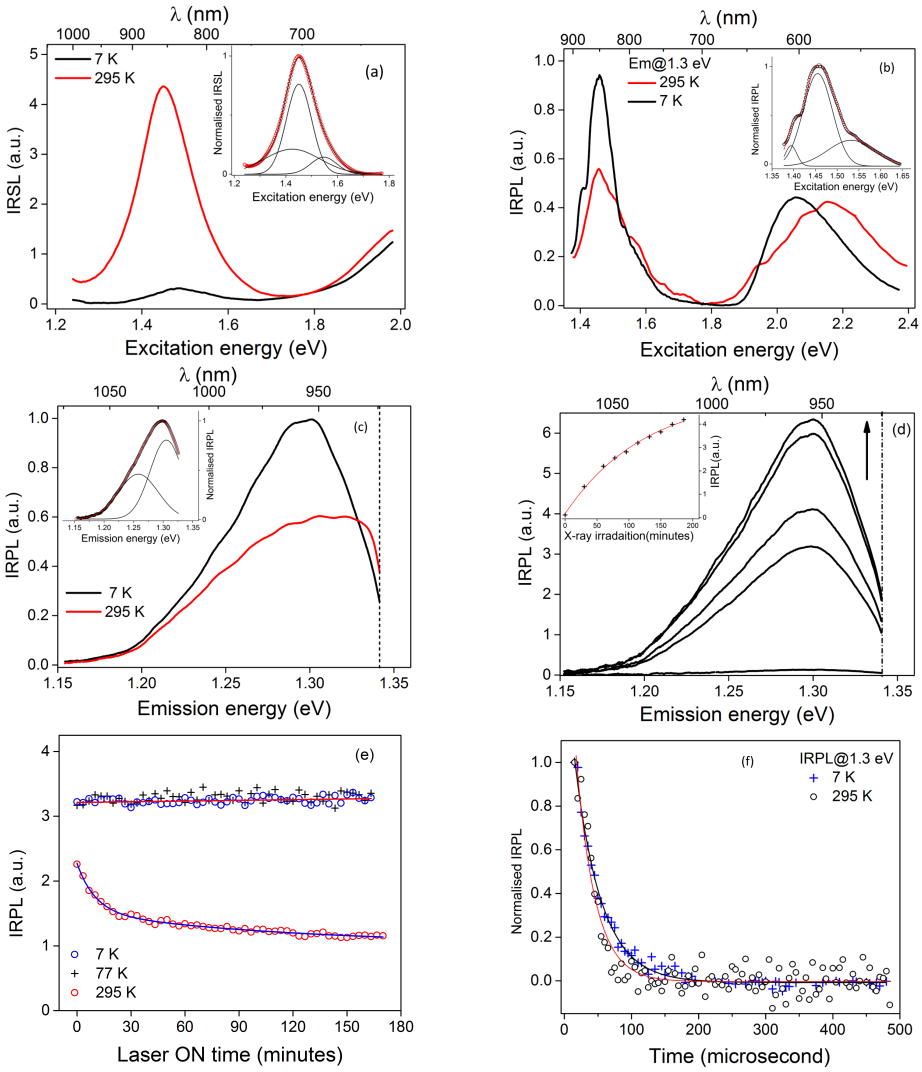

Figure 7.3: Summary of the main luminescence features for sedimentary sample R47 at 7 K and 295 K. Fitting parameters are given in Table 7.5. (a) IRSL excitation spectra; the inset shows peak fitting for 295 K data. (b) IRPL excitation spectrum after 3 hours of X-ray irradiation, recorded for emission fixed at 1.3 eV (955 nm). The inset shows peak fitting for 7 K data. (c) IRPL emission spectrum after irradiation; the inset shows the peak fitting for 7 K data. The vertical dotted line indicates the sharp-cut off long pass filter position. (d) X-ray dose dependence of IRPL spectra at 7 K, under 1.4eV (885nm) stimulation; the upward arrow shows the intensity increases as X-ray irradiation time. The inset shows the integrated dose response of IRPL. (e) Stability of IRPL under 1.4 eV(885 nm), 500 mW laser exposure. Data for 7 K and 77 K were fitted with a linear function whereas for 295 K a sum of two exponential decays is used. (f) The IRPL time-decay characteristics under 1.47 K (842nm), 90 mW laser excitation and emission at 955 nm (1.3 eV). A single exponential decay function is used for fitting.

sample was excited with the 885 nm (1.4 eV) laser for about 3 hours, and the IRPL spectrum was monitored continuously during this time. Figure 7.3(e) shows the integrated IRPL signal intensity as a function of laser exposure time. There is negligible change in the IRPL intensity at 7 K and 77 K (fitted slope: 0.0024 ± 0.0025 per hour under laser exposure) whereas at 295 K there is a rapid decrease by about 40% in the first 20 minutes, followed by a very slow decay in the remaining time. These data suggest that the IR trap behaves like a closed system at cryogenic temperatures; the time-stable IRPL signal at 7 K is also consistent with there being very little IRSL emission at 7 K. Even at 77 K there is a negligible loss of electrons from the IR dosimetric trap, however, at room temperature, about 40% of these electrons are lost to the trapped holes via diffusion through the band tail states. Both electron-hole recombination (IRSL) as well as anomalous fading, are thought to be rate limited by proximal hole availability (Murray et al, 2009, Jain and Ankjærgaard, 2011, Jain et al., 2015). Thus, it could be argued for this particular sample that about 55% (end of IRPL stimulation) of the trapped electrons are sufficiently far away from any holes to undergo spontaneous or stimulated recombination; these electrons dominantly undergo retrapping after IR excitation, and are, therefore, likely to be less prone to anomalous fading compared to those participating in the IRSL signal. The important practical implication of these data is that these distant electrons can be probed directly using IRPL, and that the dosimetric information for optical dating can be obtained non-destructively at cryogenic temperature.

An important aspect of the IRSL process that has never previously been investigated, is how long does an electron remain in the excited state subsequent to the IR excitation (i.e. the excited state lifetime); this parameter determines the efficiency of the IRSL signal and is critical for the numerical models of IRSL (Jain et al., 2012, 2015a). The IRPL signal allows a way forward in determining this crucial parameter, directly. Figure 7.3(f) shows the time decay of the IRPL signal measured at 7 K and 295 K, using a time correlated single photon counting system (TCSPC) and a pulsed laser of wavelength 842 nm (1.47 K), average output power of 90 mW and switching speed of 3 ns. The data was fitted with a single exponential decay function, which yield the IRPL lifetime of (29 ± 2) µs at 295 K and (40 ± 1) µs at 7 K. Since IRPL originates from internal transition within the IR dosimetric trap, these values correspond to the lifetime of the excited state at 295 and 7 K respectively.

The faster decay of the excited state population at 295 K could be attributed to the thermal activation of: a) non-radiative relaxation within the centre commonly seen in many defects (e.g. Zhang et al., 1993, Lyu et al., 1991, Prasad et.al., 2016b), and/or b) loss of electrons from the excited state to the band tail states as evidenced in the generation of the IRSL signal at 295 K (Figure 7.1(a)). Based on IRSL excitation spectrum at 7 K (Figure 7.3(a)), direct excited state tunneling is expected to be a minor component at room temperature (Poolton et al. 2009). The combined relative probability of these non-radiative losses at 295 K can be estimated from the lifetime data: $P_{nr}/(P_r + P_{nr}) = 27\%$, where $P_r + P_{nr} = 1/29\ \mu s^{-1}$ and $P_r \approx 1/40 \mu s^{-1}$ (7 K). The drop in the intensity of the initial IRPL signal in Figure 7.3(e) ($(3.2-2.25)/3.2 = 30\%$) is thus entirely consistent with that predicted from the lifetime data. If this drop in the IRPL intensity was only due to the non-radiative internal relaxation, then the IRPL data at 295 K would be invariant with time just like the 7 K data. But this is not the case; there is a significant loss in the IRPL with time at 295 K ($\sim 55\%$ at the end of stimulation; see previous section), attesting to the fact that loss of electrons from the excited state to the band tail states is a significant factor in determining the excited state lifetime at room temperature.

7.3.3 Sample dependence of IRPL

In order to investigate the dependence of IRPL on the sample composition we measured the IRSL and IRPL signals on a variety of feldspar samples (See Table 7.1). The IRSL and IRPL signals were measured in the Risø TL/OSL reader after a dose of 700 Gy and a preheat of 250 °C. Figure 7.4(a) shows the correlation between the two signals in samples in both the alkali (Na/K) and plagioclase (Na/Ca) feldspar groups. The IRSL signal was integrated over a measurement time of 50 s whereas the IRPL signal was integrated over 220 s. There is generally a positive correlation between the two signals, confirming that they have the same source. Figure 7.4(b) shows the correlation between IRPL and the K, Na, Ca contents. On an average there appears to be a positive correlation between the IRPL intensity and the K content (Figure 7.4(b)). It is also evident that the IRPL signal is not unique to the alkali feldspars only. Figure 7.4(b) shows how the intensity of IRPL signal varies with the composition. It is evident that IRPL sensitivity shows a bias towards higher K content.

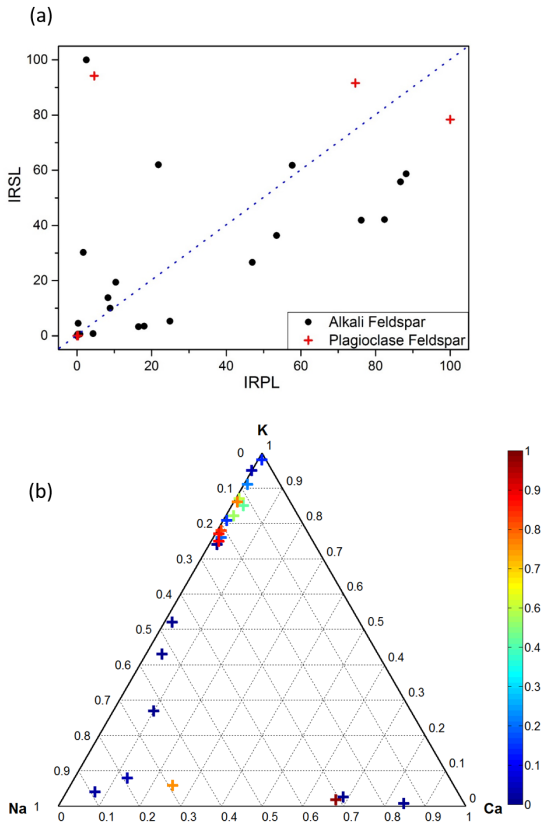

Figure 7.4: (a) Comparison of the normalised IRSL and IRPL for 25 different feldspar samples listed in Table 7.1, split between the alkali (Na/K) and plagioclase (Na/Ca) feldspar series (b) Ternary diagram showing sample position and IRPL intensity as per the colour scheme in the legend.

The detailed spectral, dose and time-resolved measurements presented in sections 7.3.1 and 7.3.2 have concentrated on the brightly emitting K-rich sedimentary feldspar R47. In order to show that the characteristics are not unique to that sample, complimentary measurements are now described on two further K-rich samples (which are available as supplementary information (SI)), one a single crystal museum specimen (R28; dimensions $2\times2\times1$ mm^3) and a second sedimentary material, R51 (granular, 180-250 µm. R28 was used previously by Poolton et al. (2009), Kars et al. (2013) and Andersen et al. (2012) for detailed spectroscopic measurements on the IRSL signal. The data are shown in SI-1 for R51 and SI-2 for R28, and the fitting parameters for the excitation, emission and TCSPC data are summarized in Table 2. The general conclusion from these measurements is that the IRPL shows a similar behavior in the three samples (R47, R51 and R28).

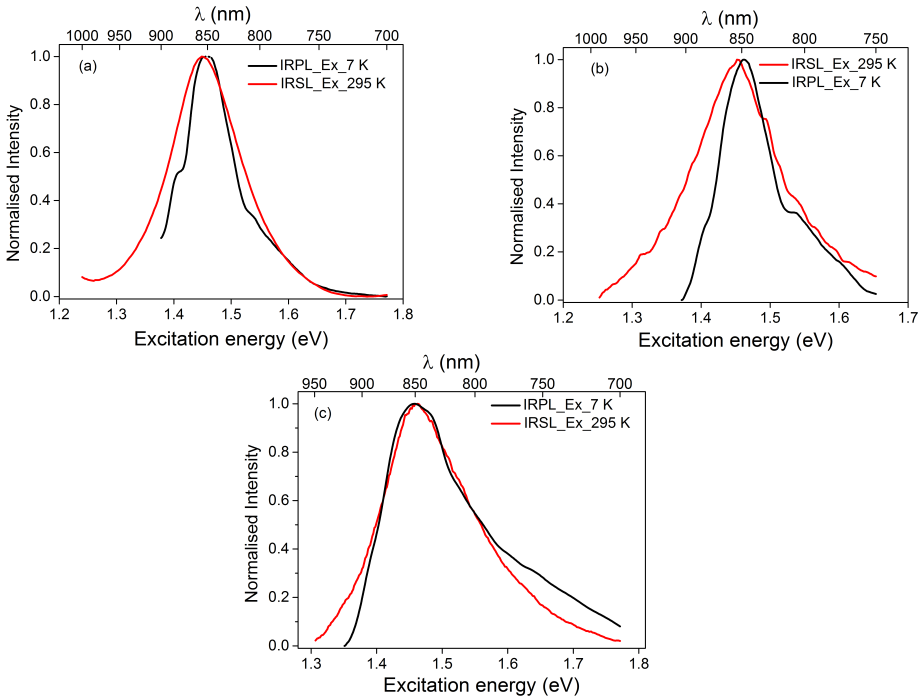

Figure 7.5: Comparison of excitation spectrum of IRPL at 7 K and IRSL at 295 K for (a) R47, (b) R51 and (c) R28

A comparison of the IRSL (295 K) and IRPL (7 K) excitation spectra for the three samples, R47, R51, and R28, are presented in Figure 7.5(a),

(b) and (c) respectively. There is a good agreement between the resonant peak positions of the IRPL and IRSL signals. Interestingly, there is a tendency for an overlap between the high energy side of the peaks, while at the lower energy side the IRPL falls off more rapidly than the IRSL. This suggests that there may be another resonance level corresponding to the second excited state at around >1.6 eV (seen more clearly in the sample R28).

7.4 Application of IRPL in Optical dating

In this section we explore the application of IRPL signal for sediment dating (evaluating natural dose) using additive dose and regenerative dose protocols that are generally used in optical dating.

7.4.1 Additive beta dose response curve

We measured the additive dose, beta dose response curves for sample R47 after bleaching the aliquots for $\sim$ 24 hours under the SOL simulator and heating at 450 °C for 100 s. After bleaching, the aliquots were irradiated with a beta source followed by IRPL signal measurement for 250 s; this cycle was repeated until a cumulative dose of 17 kGy was given to the sample. The time and dose-dependence of IRPL data are shown in Figure 7.6(a). The signal increases up to about 3.7 kGy of added dose, after which there is no detectable increase in the signal. The IRPL curves for additive doses up to 1.3 kGy show an initial rise in the signal intensity in the first 10 seconds after which the signal appears to reach a steady state. At doses above 1.3 kGy, there is about 10% reduction in the signal intensity between 50-250 seconds of stimulation. These data suggest that most of the IR dosimetric traps quite simply undergo excitation-relaxation transitions upon stimulation with IR light, without the significant loss of electron (note that the depletion seen in Figure 7.3(e) occurs over 20 minutes). This interpretation is in confirmation with our current understanding of feldspar (Jain and Ankjærgaard, 2011), which suggests that IRSL reflects the decay of a small population consisting of the nearby electron-holes, while thermal assistance during IR stimulation is necessary to access a larger population of distant electron-holes (e.g. as in the case of post IR-IRSL signals, Thomsen et al, 2008).

Figure 7.6(b) shows the additive beta dose response curves measured in the above procedure for our three samples; the signal in R47 reaches

Table 7.4: List of samples, their bulk composition as determined by XRF and signal intensities. S represents feldspars of sedimentary origin, and M represents museum single crystal samples. Data shown in bold indicate samples where detailed measurements are provided. The bold indicates that the IRPL characteristics of these samples were explored in detail (see in section 7.3.3 u/k:unknown.

Sample Code	Type of Feldspar	Provenance	K	Na	Ca	Normalised IRPL(%)	Normalised IRSL(%)	IRPL/IRSL Ratio
Only cup	-	-	-	-	-	0	0	–
R41	M	Brazil	0.97	0.01	0.01	16.5	3.3	0.2
R28	**M**	**Switzerland**	**0.95**	**0.05**	**0**	**4.3**	**0.8**	**0.2**
R42	S	China	0.91	0.08	0.01	8.9	10	1.12
R43	S	China	0.91	0.08	0.01	8.3	13.8	1.66
R44	M	Spain	0.91	0.08	0.01	24.9	5.3	0.21
R45	M	Norway	0.87	0.12	0.01	57.7	61.8	1.07
R46	M	Norway	0.86	0.13	0.01	76.2	41.9	0.55
R47	**S**	**China**	**0.85**	**0.12**	**0.03**	**47**	**26.6**	0.57
R48	M	Russia	0.83	0.16	0.02	53.5	36.3	0.68
R49	S	China	0.83	0.16	0.02	10.4	19.4	1.87
R50	M	u/k	0.8	0.18	0.01	18	3.5	0.19
R51	M	Norway	0.78	0.21	0.01	82.4	42.1	0.51
R52	M	Norway	0.77	0.22	0.01	86.7	55.8	0.64
R53	M	India	0.76	0.22	0.02	21.8	62	2.84
R54	M	Norway	0.75	0.23	0.02	88.2	58.7	0.67
R55	M	u/k	0.74	0.24	0.02	0.3	4.5	15
R56	M	u/k	0.52	0.46	0.02	0.8	0.6	0.75
R57	**M**	**u/k**	**0.43**	**0.53**	**0.04**	**0.2**	**0.6**	**3**
R58	M	u/k	0.27	0.63	0.1	1.7	30.2	17.8
R59	M	India	0.04	0.89	0.07	2.5	100	40
R60	M	u/k	0.08	0.79	0.13	4.6	94.2	20.5
R61	M	Norway	0.06	0.69	0.25	74.6	91.6	1.23
R62	M	UK	0.02	0.31	0.67	100	78.4	0.78
R63	S	Iceland	0.03	0.29	0.69	0	0	–
R64	S	Iceland	0.01	0.15	0.85	0.3	0.01	0.033

Table 7.5: Summary of fitting parameters for the samples R47, R51 and R28. Peak fittings shown in bold indicate main (dominating) peak.

		Feldspar samples		
Experiments	Temperature [K]	R47 [eV]	R51 [eV]	R28 [eV]
IRPL excitation spectrum	7	1.394 ± 0.006 1.455 ± 0.009 1.53 ± 0.01	1.399 ± 0.005 1.458 ± 0.003 1.541 ± 0.003	1.463 ± 0.005 1.568 ± 0.008
IRPL emission spectrum	7	1.258 ± 0.001 1.305 ± 0.003	1.223 ± 0.003 1.286 ± 0.001	1.232 ± 0.001 1.304 ± 0.002
IRSL excitation spectrum	295	1.42 ± 0.0 1.451 ± 0.002 1.55 ± 0.01	1.32 ± 0.01 1.372 ± 0.004 1.446 ± 0.008 1.49 ± 0.09	1.358 ± 0.002 1.453 ± 0.004 1.527 ± 0.008
TCSPC	7	40 ± 1 µs	47 ± 2 µs	48 ± 4 µs
TCSPC	295	28 ± 2 µs	29 ± 4 µs	41 ± 7 µs

a saturation level at about 2 kGy, whereas in R51 and R28 the saturation level occurs around 5 kGy. The important conclusion of these measurements are: a) it is easily possible to measure IRPL signal without worrying about signal depletion (apparent 10% depletion occurs only at very high doses that are not useful for dose estimation in any case), and b) that all the samples show the expected saturating exponential dose response behavior with a dynamic range that is similar to IRSL.

7.4.2 Regenerative beta dose response curve

The Single Aliquot Regenerative Dose (SAR) protocol is currently the commonly used method for feldspar dating (see Murray and Wintle, 2000, Wallinga et al., 2000), and the aim here is to verify if an equivalent method can be used to extract dose information using the IRPL signal. However, in order to apply a regenerative dose protocol, it is important to be able to empty the signal during a SAR cycle. Figure 7.6(c) shows the bleaching of the IRPL signal with blue light for 100 s at various temperatures following the protocol in Table 7.2. The remaining signal was calculated by taking the ratio of IRPL in Step 7 divided by Step 5. There is nearly complete zeroing of the signal for illumination of 100 s at 450 °C, and > 90% bleaching at 300 °C. As shown earlier, there was no detectable depletion of IRPL in the individual 100 s readouts (see

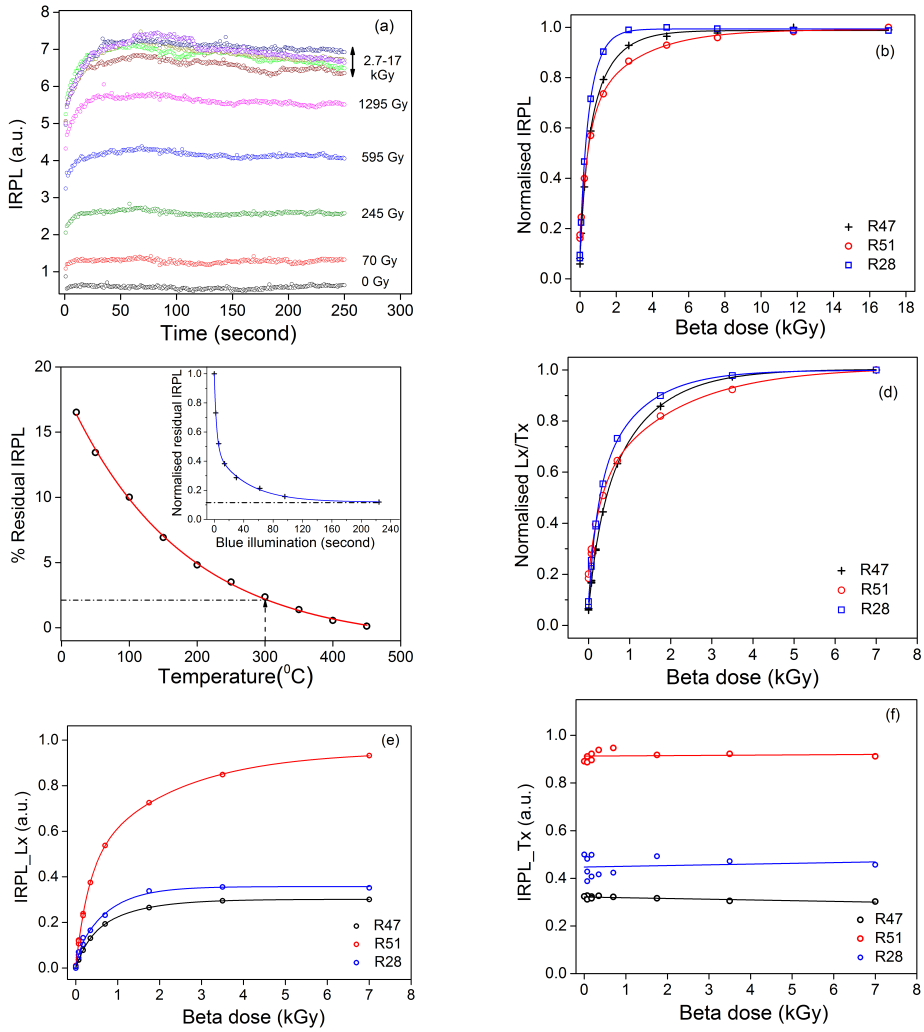

Figure 7.6: Summary and comparison of the dose and bleaching properties of IRPL in 3 representative K-feldspars; R47 and R51, and single crystal R28. (a) Dose dependent IRPL in R47 at 295 K as a function of the laser (1.4 eV, 885 nm) stimulation time. (b) Additive beta dose response of the samples; the points represent the time integral over the first 250 s of laser exposure. (c) Residual IRPL (test dose normalised) after blue illumination for 100 s at different temperatures. Inset: the residual IRPL as a function of blue illumination time at 295 K. (d) The SAR dose response of the samples using the protocol in Table 7.3. Individual Lx and Tx data are shown in Figures 7.6(e) and 7.6(f), respectively. (e) Regenerative dose IRPL (Lx) of the samples as a function of beta dose. (f) Test dose IRPL (Tx) of the samples as a function of regeneration dose.

Figure 7.6(a)) so any signal loss can be solely attributed to the blue light exposure.

The same protocol was used to measure the signal depletion with blue light at room temperature; however, here the blue light illumination in step 6 consisted only of 2 s duration. The steps 5 and 6 were repeated for a cumulative blue light illumination of 224 s. Figure 7.6(c) inset shows the depletion of the IRPL signal with blue light at room temperature; there appear to be two components to this depletion (the data are fitted to a double exponential function), an initial rapid depletion within a few seconds and a slower depletion in tens of seconds reaching a steady state value at about 250 s. These components possibly represent bleachability of traps depending on the distance between the trapped electrons and their nearest hole sites.

Based on the above temperature dependent bleaching data Figure 7.6(c) we chose 300 °C as a good compromise for zeroing the signal, as we do not want to heat the sample too much to avoid sensitivity changes (these things will be optimised in the future work). The resulting SAR protocol is outlined in Table 7.3 and the dose response curves from the three samples are shown in Figure 7.6(d). 86% of saturation signal intensity corresponds to 1.42 kGy for R28, 1.84 kGy for R47, and 2.75 kGy for R51. There was excellent recycling ratio within 1% of unity confirming that this SAR protocol is appropriate for the IRPL signal. Figures 7.6(e, f) shows the individual responses of the regenerative signal (Lx) and the test dose signal (Tx), respectively, as a function of dose. There is almost no sensitivity change (Figure 7.6(f)) in the IRPL signal during the SAR measurement for all the sample.

In order to measure the natural dose in the samples so as to test the stability of IRPL signal we further modified the SAR sequence based on our prior knowledge that the IRPL signal does not show any detectable depletion in the laboratory measurement of over 100 s. Thus, we introduced an IRSL measurement for 50 s using LED stimulation (870 nm peak, FWHM 40 nm) before each IRPL measurement. This prior IR readout can be beneficial, since it should remove any unstable signal contribution to the IRPL signal, howsoever small. The dual IRSL-IRPL protocol is outlined in Table 7.4. Aliquots of K-feldspar (R47) were measured using this protocol; these samples have not been previously exposed to light and have retained the trapped charge due to natural dose accumulated during deposition. Figure 7.7(a) shows the dose response of

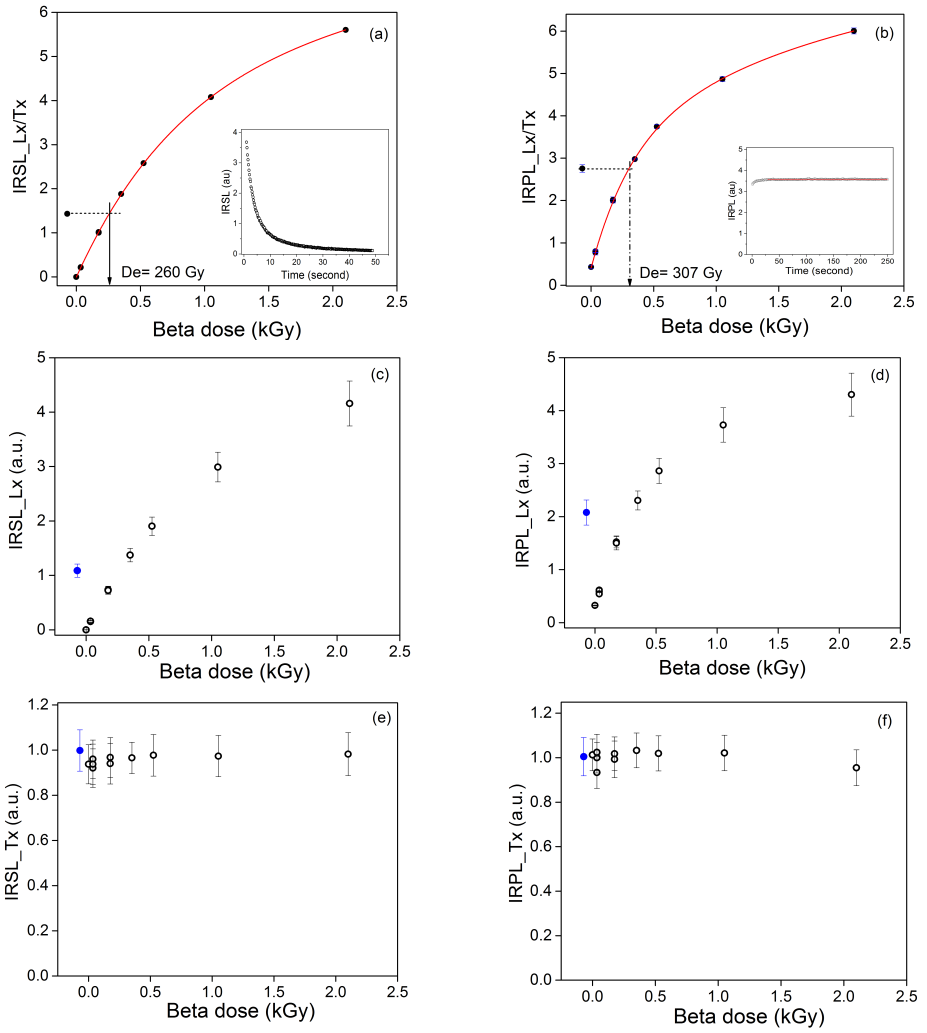

Figure 7.7: Details of dosimetry measurements for sedimentary feldspar R47. Figures (a) and (b) show the natural dose measurement via IRSL and IRPL respectively, using the dual IRSL-IRPL protocol (Table 7.4); in each case, data is fitted with two saturating exponential growth functions. The figure insets show the luminescence intensity vs. stimulation time. Figures (c) and (d) respectively show the regenerative doses IRSL (Lx) and IRPL (Lx) as a function of beta dose; the blue data points represent natural signal, (Ln). Figures (e) and (f) show the test doses IRSL (Tx) and IRPL (Tx) respectively, as a function of the corresponding regeneration dose in the SAR cycle; blue data points represent the natural signals, Tn.

IRSL signal, while the inset shows the natural IRSL signal decay. Figure 7.7(b) shows the dose response of IRPL signal, while the inset shows the natural, steady state IRPL signal. The equivalent dose using IRSL measurement was ∼260 ± 6 Gy, while that using the IRPL was ∼ (307 ± 20) Gy. The IRPL dose is consistent with the dose of ∼ 284 ± 9 Gy measured on this sample using the pIRIR 450 °C protocol widely used to reduce the fading rate in feldspar (Thomsen et al., 2008; Buylaert et al., 2012). Clearly, the IRSL signal suffers from in the well-known anomalous fading, while the IRPL signal seems to be stable, confirming that the majority of electrons do not participate in the IRSL process since they do not have a nearby recombination center, and for the same reason they do not suffer from anomalous fading. The Figure 7.7(c) and (d) show the individual responses of the regenerative signal (Lx) evaluated with IRSL and IRPL signal, whereas the test dose signal (Tx), is shown in the Figure 7.7(e) and (f) for IRSL and IRPL signal respectively, as a function of dose. The test dose intensity suggests that there is undetectable IRPL sensitivity change between the natural and the regenerative SAR cycles.

7.5 Conclusion and Outlook:

This study demonstrates that the IR dosimetric trap in feldspar can be probed directly to read the population of trapped electrons, without depending on the electron-hole recombination as in the common OSL/IRSL dating technique. The new signal, Infra-red Photoluminescence (IRPL), is generated from the internal radiative relaxation within the IR dosimetric trap upon excitation with the IR light, and can be read non-destructively. The IRPL signal is amenable to both additive dose and regeneration dose measurement protocols for optical dating. Preliminary dosimetric investigations suggest that this signal is more stable than IRSL signal, and give a dose similar to the post IR-IRSL (pIRIR-290) signal.

The IRPL signal opens a new way of measurement of dosimetric information for optical dating; it is analogous to the ESR method, i.e., it directly probes the trapped electrons. The preliminary survey of samples presented in this work suggests that in the alkali feldspar series, the signal selection may be biased towards K-feldspars, thus simplifying the internal dose rate issue. The IRPL signal shows a similar dynamic dose response range and allows possibilities of preheating as IRSL; it thus does not suffer from problems faced by infra-red radiofluorescence that

is also believed to result from radiative transition within the electron traps (although not experimentally demonstrated), but generated by the interaction of high energy ionizing radiation with the lattice.

The new optical method (IRPL) for dating feldspars that circumvents many issues relating to traditional OSL method. As future prospect, we envision the potential of IRPL for using it in practical dating applications for up to $\sim$ 0.5 Ma (and potentially beyond); it is thus seen as a step-change in optical dating techniques.

7.6 Acknowledgement

It is our pleasure to thank Dr. Jan-Pieter Buylaert for some samples and Mr. Karsten Bracht Nielsen for introducing the spectral analysis function in the Analyst software of Risø TL/OSL reader.

7.7 Supplementary Information(SI)

Results: Figure 7.8(a) and Figure 7.9(a) show the IRSL excitation spectrum of R51 and R28 at 7 K and 295 K. The 295 K spectrum for both sample shows a resonance feature in the 1.25-1.65 eV for R51 and 1.3-1.78 eV for R28. The inset of these figures shows the peak fitting of IRSL excitation spectrum at 295 K. The 7 K, IRSL excitation spectrum shows a significantly reduced intensity. Figure 7.8(b) and Figure 7.9 (b) show the excitation spectra of IRPL emission for emission at 955 nm (1.3 eV) at 7 K for R51 and R28 respectively. The IRPL excitation spectrum for R51 shows two feature in the excitation energy range 1.35-1.65 eV, 1.9-2.2 eV, whereas, the IRPL excitation spectrum for R28 shows slightly different peak features at 1.35-1.78 eV, 2-2.4 eV. The Low energy peak; 1.35-1.65 eV for R51 and 1.35-1.78 eV for R28, fitting of the IRPL excitation spectrum is presented. Figure 7.8(c) and Figure 7.9(c) shows the X-ray dose dependence of the IRPL emission spectra in the range of 1.1-1.34 eV at 7 K in R51 and R28, respectively. The inset of these figures shows the peak fitting of the IRPL emission spectrum. The integrals of these signals are plotted as a function of dose (X-ray irradiation time) in Figure 7.8(d) and Figure 7.9(d) respectively; the data are fitted with a single saturating exponential function. Figure 7.8(e) and Figure 7.9(e) represent the IRPL emission stability on the exposure of 1.4 eV (885 nm) laser at 7 K over 60 minutes for R51 and R28 respectively, confirming its non-destructive readout characteristics. Figure 7.8(f) and Figure 7.9(f) shows the temperature dependent lifetime of IRPL emission for R51 and R28 respectively. The data are fitted to single exponential functions and the derived lifetimes are summarized in Table 7.5. The general conclusion from these measurements is that the IRPL shows a similar behavior in the three samples (R47, R51 and R28) (see text).

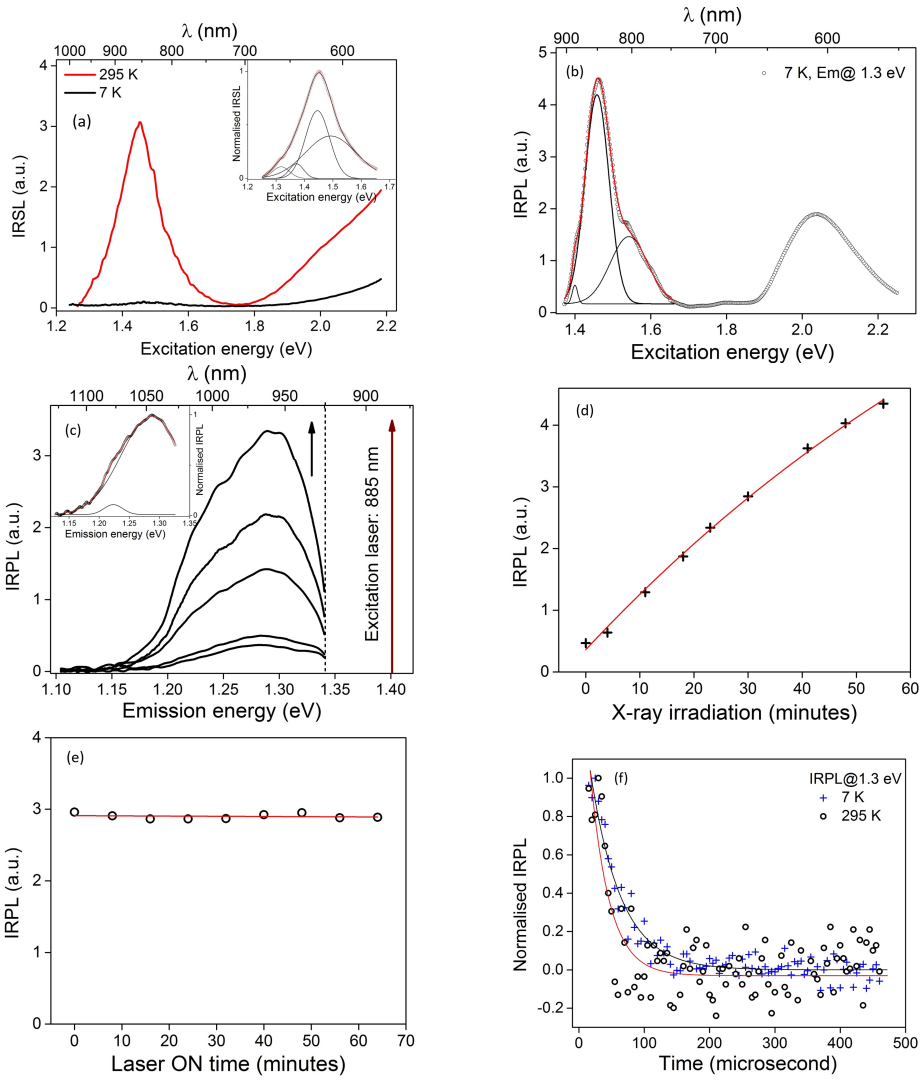

Figure 7.8: Summary of the main luminescence features for sedimentary K-feldspar, R51 at 7 K and 295 K. Fitting parameters are given in Table 7.5.(a) IRSL excitation spectra. Inset: peak fitting of the spectrum at 295 K.(b) IRPL excitation spectrum after 3 hours of X-ray irradiation, recorded at 7 K for emission fixed at 1.3 eV (955 nm). Peak fitting is in the IR range only. (c) X-ray dose dependence on the IRPL spectra at 7 K, under 1.4 eV (885 nm) stimulation; the arrow indicates the intensity evolution with irradiation time. The inset shows peak fitting of the spectrum.(d) X-ray irradiation time (dose) dependent IRPL, fitted with a single saturating exponential.(e) Stability of IRPL at 7 K under 1.4 eV (885 nm), 500 mW laser exposure. The data was fitted with a linear function.(f) Time decay of the IRPL measured at 955 nm (1.3 eV), using 1.47 eV (842 nm), 90 mW laser excitation. The data is fitted with single exponential decay functions.

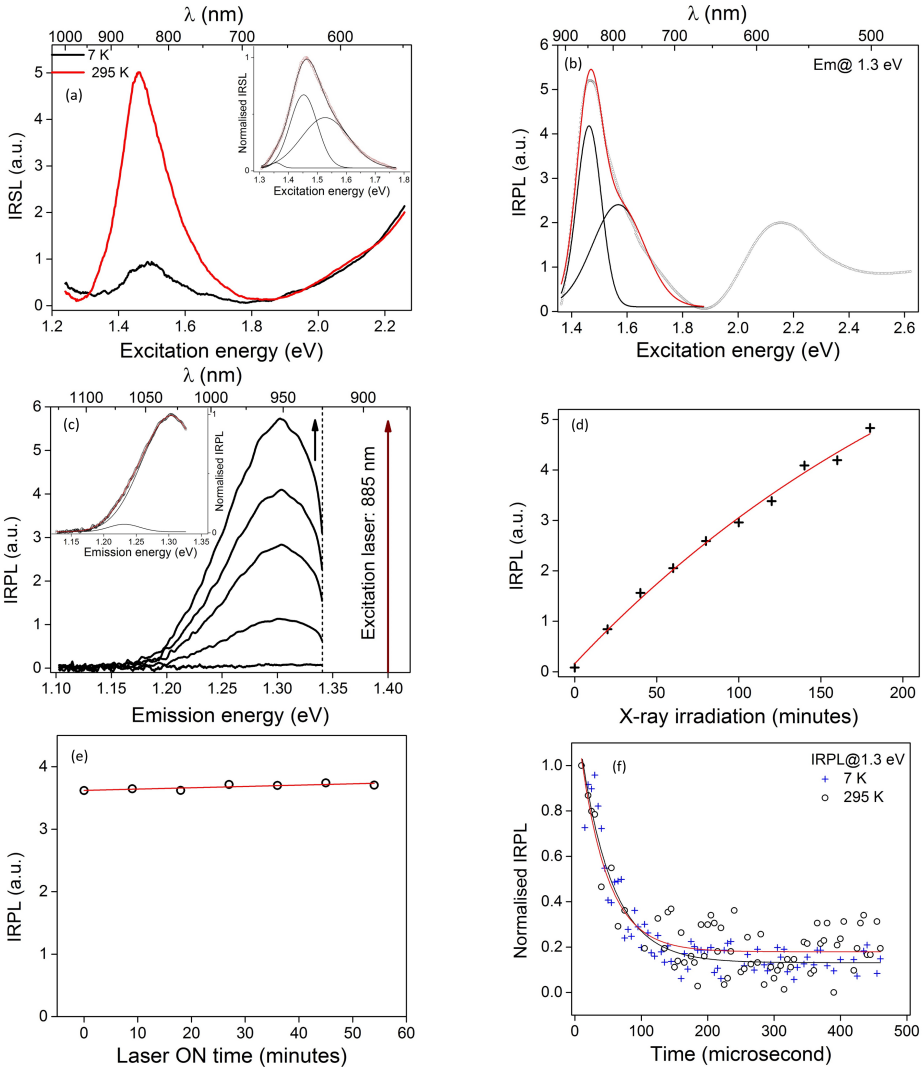

Figure 7.9: Summary of the main luminescence features for museum single crystal K-feldspar specimen R28 at 7 K and 295 K. Fitting parameters are given in Table 7.5.(a) IRSL excitation spectra. Inset: peak fitting at 295 K. (b) IRPL excitation spectrum at 7 K after 3 hours of X-ray irradiation, recorded for emission fixed at 1.3 eV (955 nm). The peak fitting is for the IR range only. (c) X-ray dose dependence on IRPL spectra, measured at 7 K, under 1.4 eV (885 nm) stimulation; the upward arrow shows the intensity increases as X-ray irradiation time, and curve fitting given in the inset.(d) X-ray irradiation time (dose) dependent IRPL, fitted with a single saturating exponential.(e) Stability of IRPL under 1.4 eV (885 nm), 500 mW laser exposure. The data was fitted with linear function.(f) Time decay of the IRPL measured at 955 nm (1.3 eV), using 1.47 eV (842 nm), 90 mW laser excitation. The data is fitted with single exponential decay functions.

Bibliography

[1] Andersen, M. T., Jain, M., Tidemand-Lichtenberg, P. (2012). Red-IR stimulated luminescence in K-feldspar: Single or multiple trap origin? Journal of Applied Physics, 112(4), 043507.

[2] Buylaert, J. P., Jain, M., Murray, A. S., Thomsen, K. J., Thiel, C., & Sohbati, R. (2012). A robust feldspar luminescence dating method for Middle and Late Pleistocene sediments. Boreas, 41(3), 435-451.

[3] Buylaert, J. P., Murray, A. S., Thomsen, K. J., & Jain, M. (2009). Testing the potential of an elevated temperature IRSL signal from K-feldspar. Radiation Measurements, 44(5), 560-565.

[4] Baril, M. R., & Huntley, D. J. (2003a). Optical excitation spectra of trapped electrons in irradiated feldspars. Journal of Physics: Condensed Matter, 15(46), 8011.

[5] Baril, M.R., & Huntley, D. J. (2003b). Infrared stimulated luminescence and phosphorescence spectra of irradiated feldspars. Journal of Physics: Condensed Matter, 15(46), 8029.

[6] Bøtter-Jensen, L., Thomsen, K. J., & Jain, M. (2010). Review of optically stimulated luminescence (OSL) instrumental developments for retrospective dosimetry. Radiation Measurements, 45(3), 253-257.

[7] Grün, R. (1989). Present status of ESR-dating. International Journal of Radiation Applications and Instrumentation. Part A. Applied Radiation and Isotopes, 40(10-12), 1045-1055.

[8] Huntley, D. J., Godfrey-Smith, D. I., & Thewalt, M. L. (1985). Optical dating of sediments. Nature, 313(5998), 105-107.

[9] Hütt, G., Jaek, I., & Tchonka, J. (1988). Optical dating: K-feldspars optical response stimulation spectra. Quaternary Science Reviews, 7(3-4), 381-385.

[10] Jain, M. (2014). Feldspar, Infrared-Stimulated Luminescence. Encyclopedia of Scientific Dating Methods, 279-284.

[11] Jain, M., & Ankjærgaard, C. (2011). Towards a non-fading signal in feldspar: insight into charge transport and tunnelling from time-resolved optically stimulated luminescence. Radiation Measurements, 46(3), 292-309.

[12] Jain, M., Guralnik, B., & Andersen, M. T. (2012). Stimulated luminescence emission from localized recombination in randomly distributed defects. Journal of Physics: Condensed Matter, 24(38), 385402.

[13] Jain, M., Sohbati, R., Guralnik, B., Murray, A. S., Kook, M., Lapp, T., Prasad, A.K., Thomsen, K.J. & Buylaert, J. P. (2015a). Kinetics of infrared stimulated luminescence from feldspars. Radiation Measurements, 81, 242-250.

[14] Jain, M., Buylaert, J. P., Thomsen, K. J., & Murray, A. S. (2015b). Further investigations on 'non-fading' in K-Feldspar. Quaternary International, 362, 3-7.

[15] Kars, R. H., Poolton, N. R., Jain, M., Ankjærgaard, C., Dorenbos, P., & Wallinga, J. (2013). On the trap depth of the IR-sensitive trap in Na-and K-feldspar. Radiation Measurements, 59, 103-113.

[16] Krbetschek, M. R., Trautmann, T., Dietrich, A., & Stolz, W. (2000). Radioluminescence dating of sediments: methodological aspects. Radiation Measurements, 32(5), 493-498.

[17] Krbetschek, M. R., Götze, J., Dietrich, A., & Trautmann, T. (1997). Spectral information from minerals relevant for luminescence dating. Radiation Measurements, 27(5), 695-748.

[18] Li, B., & Li, S. H. (2011). Luminescence dating of K-feldspar from sediments: a protocol without anomalous fading correction. Quaternary Geochronology, 6(5), 468-479.

[19] Lapp, T., Kook, M., Murray, A. S., Thomsen, K. J., Buylaert, J. P., & Jain, M. (2015). A new luminescence detection and stimulation head for the Risø TL/OSL reader. Radiation Measurements, 81, 178-184.

[20] Lapp, T., Jain, M., Thomsen, K. J., Murray, A. S., & Buylaert, J. P. (2012). New luminescence measurement facilities in retrospective dosimetry. Radiation Measurements, 47(9), 803-808.

[21] Lyu, L. J., & Hamilton, D. S. (1991). Radiative and nonradiative relaxation measurements in Ce^{3+} doped crystals. Journal of luminescence, 48, 251-254.

[22] Morthekai, P., Thomas, J., Pandian, M. S., Balaram, V., & Singhvi, A. K. (2012). Variable range hopping mechanism in band-tail states of feldspars: A time-resolved IRSL study. Radiation Measurements, 47(9), 857-863.

[23] Murray, A. S., & Wintle, A. G. (2000). Luminescence dating of quartz using an improved single-aliquot regenerative-dose protocol. Radiation measurements, 32(1), 57-73.

[24] Murray, A. S., Buylaert, J. P., Thomsen, K. J., & Jain, M. (2009). The effect of preheating on the IRSL signal from feldspar. Radiation Measurements, 44(5), 554-559.

[25] Poolton, N. R. J., Kars, R. H., Wallinga, J., & Bos, A. J. J. (2009). Direct evidence for the participation of band-tails and excited-state tunnelling in the luminescence of irradiated feldspars. Journal of Physics: Condensed Matter, 21(48), 485505.

[26] Poolton, N. R. J., Wallinga, J., Murray, A. S., Bulur, E., & Bøtter-Jensen, L. (2002). Electrons in feldspar I: on the wavefunction of electrons trapped at simple lattice defects. Physics and Chemistry of Minerals, 29(3), 210-216

[27] Poolton, N. R. J., Bos, A. J. J., & Dorenbos, P. (2012). Luminescence emission from metastable Sm^{2+} defects in YPO_4: Ce, Sm. Journal of Physics: Condensed Matter, 24(22), 225502.

[28] Prasad, A. K., Lapp, T., Kook, M., & Jain, M. (2016a). Probing luminescence centers in Na rich feldspar. Radiation Measurements, 90, 292-297.

[29] Prasad, A. K., Kook, M., & Jain, M. (2016b). Probing metastable Sm^{2+} and optically stimulated tunnelling emission in YPO_4: Ce, Sm. Radiation Measurements, In press.

[30] Rhodes, E. J. (2011). Optically stimulated luminescence dating of sediments over the past 200,000 years. Annual Review of Earth and Planetary Sciences, 39, 461-488.

[31] Roberts, R. G., Jacobs, Z., Li, B., Jankowski, N. R., Cunningham, A. C., & Rosenfeld, A. B. (2015). Optical dating in archaeology: thirty years in retrospect and grand challenges for the future. Journal of Archaeological Science, 56, 41-60.

[32] Roberts, R. G., & Lian, O. B. (2015). Dating techniques: Illuminating the past. Nature, 520(7548), 438-439.

[33] Schulman, J. H., Ginther, R. J., Klick, C. C., Alger, R. S., & Levy, R. A. (1951). Dosimetry of X-rays and gamma-rays by radiophotoluminescence. Journal of Applied Physics, 22(12), 1479-1487.

[34] Thomsen, K. J., Murray, A. S., Jain, M., & Bøtter-Jensen, L. (2008). Laboratory fading rates of various luminescence signals from feldspar-rich sediment extracts. Radiation measurements, 43(9), 1474-1486.

[35] Tsukamoto, S., Denby, P. M., Murray, A. S., & Bøtter-Jensen, L. (2006). Time-resolved luminescence from feldspars: new insight into fading. Radiation Measurements, 41(7), 790-795.

[36] Trautmann, T., Dietrich, A., Stolz, W., & Krbetschek, M. R. (1999). Radioluminescence dating: a new tool for Quaternary geology and archaeology. Naturwissenschaften, 86(9), 441-444.

[37] Wintle, A. G. (1973). Anomalous fading of thermo-luminescence in mineral samples. Nature, 245(5421), 143-144.

[38] Wallinga, J., Murray, A., & Wintle, A. (2000). The single-aliquot regenerative-dose (SAR) protocol applied to coarse-grain feldspar. Radiation Measurements, 32(5), 529-533.

[39] Zhang, Z., Grattan, K. T., & Palmer, A. W. (1993). Temperature dependences of fluorescence lifetimes in Cr^{3+} doped insulating crystals. Physical Review B, 48(11), 7772.

Chapter 8

Summary and conclusion

The main purpose of my Ph.D. research was to understand defect-related luminescence processes in wide bandgap materials. The two materials I have investigated are feldspar, a natural mineral which is widely used in optical dating, and yttrium phosphate (co-doped with Ce^{3+} and Sm^{3+}), a model analogue for feldspar-like materials. I made extensive use of multi-probe, low-temperature techniques for my research; however, when I started my Ph.D., the facilities required to perform such techniques were not yet fully available at DTU Nutech. This gave me the opportunity to actively participate in the instrumentation development necessary to enable the complex experiments undertaken during my research. My inputs to instrumentation development were in: (i) optical interface modelling using the Zemax software, and commissioning and testing of the Risø TL-OSL spectrometer, and (ii) commissioning and testing of the Risø Station for CryOgenic LUminescence Research (COLUR).

Feldspar and quartz are the two main minerals used in luminescence dating. With novel developments in infra-red stimulated luminescence (IRSL) dating over the last decade, feldspar is increasingly considered as a reliable dosimeter. Feldspar is especially important for dating old samples (about >100 ka), as quartz is unreliable in this time range because of the signal saturation effect. In the past, feldspar has been widely studied using spectroscopic techniques that typically involve ionizing ra-

diation (for example, cathodoluminescence, radioluminescence, ionoluminescence, thermoluminescence, optically stimulated luminescence etc.). Similarly, there have been many efforts to understand the time scales of luminescence emissions (from nanoseconds to seconds) using Time-Resolved Optically Stimulated Luminescence (TR-OSL). Although, these techniques have played an important role in developing a robust phenomenological model of dosimetric signals in feldspar, they suffer from the fundamental limitation that both trapped electrons and trapped holes are involved in the luminescence generating mechanism. In order to further advance the luminescence dating technique, it is important to be able to (i) characterize the defects related to electron traps and the hole traps, individually, and (ii) study charge-transfer and energy-transfer across these defects. Site-specific photoluminescence spectroscopy, especially at low temperatures, is a powerful tool to undertake such characterization. This technique has, for example, been widely used to study defects in semi-conductors and optical materials, but its application to natural dosimeters used in luminescence dating has been limited. A better understanding of luminescence defects and processes in quartz and feldspar will place the OSL dating technique on a more firm footing, and possibly lead to further enhancement of its capabilities.

Inspired by both the complexity and the enormous potential of feldspar in the novel, inter-disciplinary field of luminescence dating, I focused my research on obtaining a better understanding of luminescent defects in feldspar. In the following sections, I provide a brief summary, the highlights and the expected impact of my research.

8.1 Summary: Contributions to the feldspar luminescence model

Chapter 1 is an introduction to this thesis and chapter 2 presents the instrumentation details for the experiments carried out in this research. Chapters 3 to 7 in this thesis present different physical aspects of feldspar, and a feldspar analogue, as a luminescence dosimeter. Chapter 3 makes a reconnaissance of the application of radioluminescence (RL), X-ray excited optical luminescence (XEOL) and site-specific photoluminescence (PL) spectroscopy techniques, in combination with time-resolved measurements, to characterize the four main emission bands, viz. UV (4.27 eV), violet (3.04 eV), orange-green (2.1 - 2.5 eV) and deep red (1.65 eV), in

feldspar. Chapters 4 and 5 present detailed investigations on the orange-green emission, and the deep red emission, respectively. Together the main conclusions of Chapters 3, 4 and 5 are:

1) The UV and violet-blue emissions show resonant excitations arising from a distribution of energy levels.

2) The broad green, or the orange-green emission, arises from interaction of a deep lying defect (>2 eV) with the band tail states. Contrary to common perception, it is also argued that this emission is not due to the Fe^{3+} ion.

3) The deep red emission arises from Fe^{3+}, but its emission energy can vary dynamically even within a single sample due to the site dependence of the ion. The non-resonant UV excitation spectrum of Fe^{3+} is discussed in the context of the band-tail model. It is also shown that the PL of Fe^{3+} cannot be used as a dosimetric signal.

These results illustrate the complexity of feldspar as a luminescent system, and the importance of band tail states in luminescence generation. After these emission characterisation, the issue of excited state tunneling in feldspar is addressed by examining the feldspar-analogue model system - YPO_4:Ce,Sm (Chapter 6). Just like feldspar, this system consists of a random distribution of defects and an electron trapping site Sm^{2+} that has its excited state below the conduction band. By detailed spectroscopic analysis of the metastable Sm^{2+} (electron trap), we obtained insight into the two main optically induced transitions in this system: internal radiative relaxation, which is dominant at low temperatures (<150K), and, phonon relaxation and tunneling to Ce^{4+}, which become dominant at higher temperatures. Analysis of the kinetics of the excited state tunneling mechanism (from Sm^{2+}) to the Ce^{4+} confirmed the application of the prevalent mathematical model of optically stimulated tunneling in feldspar.

The study of Sm^{2+} in Chapter 6 inspired me to look for a similar intra-defect luminescence in the IR dosimetric trap (IR trap) in feldspar. These investigations resulted in the discovery of a new signal termed infra-red photoluminescence (IRPL). The details of IRPL presented in Chapter 7 suggest that the internal radiative relaxation from the IR trap can be probed in a quasi-steady-state mode (without significant loss of trapped electrons) at low temperatures. The time scales of relaxation within the IR trap are also presented for the first time; this is important information for the mathematical models of optically stimulated tunnel-

ing in feldspar. This chapter gives a direct experimental verification that only a fraction of the IR traps (fading pupulation) are sampled during IRSL; thus there exists a large reservoir of IR traps which may be sampled for more accurate feldspar dating.

In summary, the results presented in Chapters 3 to 7 significantly improved our existing feldspar model by giving new insights into the recombination sites and their interactions with the band tail states, the internal characteristics of the IR trap, and the mechanism of excited state tunneling.

8.2 Research highlights

My research has significantly advanced our understanding of the feldspar dosimeter system, and has led to development of new measurement techniques, which will significantly impact the future of luminescence dating. The key, new findings of my research are:

1. Discovery of the excitation-energy dependent emission in the orange-green (2.1-2.5 eV) emission band. It was observed that the orange-green PL emission shifts strongly with the excitation energy, irrespective of feldspar composition. This phenomenon, called the 'red edge effect', has to my knowledge, never been reported from crystalline materials; it has only been seen in polar solvents and carbon based quantum dots. A novel phenomenological model for the red edge effect has been developed. It is demonstrated that this effect arises from photo-ionisation of a deep lying defect by direct electron excitation to the band tail states. Subsequent interaction between the excited state of the defect and hopping and thermalisation processes in the band tail result in the red edge effect.

2. It is shown that the red-edge effect discussed above can be used to estimate the width of the band tail states in feldspar. Furthermore it is inferred that the orange-green emission in feldspar may not arise from Mn^{2+} as is commonly believed. It is speculated that this emission is possibly related to surface alteration defects if feldspar.

3. It is observed that both the emission and resonant excitation peaks of Fe^{3+} can vary within the same sample. There is a strong red shift in the Fe^{3+} emission with decreasing excitation energy; this suggests a site dependence of Fe^{3+} on the deep red emission. This effect is significantly enhanced at low temperatures because of the phonon effect.

4. There is an excitation energy dependence (resonant vs. non-

resonant) of the main radiative transition ($^4T_1 \rightarrow {}^6A_1$) in Fe^{3+}. We suggest that excitation of the Fe^{3+} ion to its higher resonance energy levels may involve an additional time step related to spin-lattice interaction. This is an important new physical insight into the Fe^{3+} system which requires further investigations.

5. It is shown that direct mapping of the metastable energy levels of Sm^{2+} can be obtained using the defects internal radiative transition. So far the mapping of Sm^{2+} or other electron trapping metastable defects has been done using the process of tunneling-based electron-hole recombination, which results in broad, diffuse excitation peaks. The direct probing, as done during this research, gives sharply-resolved peaks, and thus, a precise and accurate mapping of the transition levels. The temperature dependence of the metastable Sm^{2+}) lifetime is also presented for the first time; this gives insight into the thermal quenching mechanism.

6. The kinetics of excited state tunneling using a controlled experiment are tested for the first time. Although, excited state tunneling has been proposed to be important in feldspar and other materials, there has been no direct testing of the mathematical models using a controlled experiment. The analysis of OSL decay curves resulting from optically induced, sub-conduction band electron transfer ($Sm^{2+} \rightarrow Ce^{4+}$) provides such a test for the first time. It was concluded that the prevalent mathematical model of excited-state tunneling makes an accurate description of the $Sm^{2+} \rightarrow Ce^{4+}$ system.

7. This research has discovered a Stokes shifted infra-red photoluminescence (IRPL) signal in feldspar. Currently, optical dating of feldspar using the IRSL technique relies on transfer of electrons from the IR dosimetric trap to holes located elsewhere in the lattice. Similar to the Sm^{2+} defect in YPO4, it is shown that IRPL arises from intra-defect excitation and subsequent radiative emission within the IR trap. The IRPL signal can be probed non-destructively (especially at low temperatures), and it is appears that it does not suffer from anomalous fading. IRPL provides a new method of studying the IR trap without relying on electron-hole recombination. Application of IRPL to sediment dating has been demonstrated.

8.3 Impact of this research

It is my expectation that my Ph.D. research will make a contribution not only in the field of luminescence dosimetry but also in the study of optical materials. The different areas in which my research is expected to have most impact are described below.

1. Band tail states play an important role in determining thermal stability of trapped charge in feldspar; an issue of immense relevance for use of feldspar in geochronometry and thermochronometry. However, there is no easy, straightforward way to make a direct, routine characterization of band tail states in samples used in optical dating. Based on our understanding of the giant red edge effect, we propose a simple, robust method for measurement of band tail width in feldspar. A simple and less expensive excitation spectrometer could be developed to enable routine measurement of the band tail states in different laboratories, which in combination with the thermal measurements, should give a robust estimate of the thermal stability of the IR trap.

2. In carbon based quantum dots, the red edge effect has attracted immense attention, and it has still not been explained satisfactorily. Understanding this effect is very important for the potential applications of quantum dots in optics. Our model involving interaction between a deep defect state and the band tail states gives an alternative explanation of the red edge effect. This model deserves testing on the quantum dot systems, as these nanomaterials also contain band tail states. Furthermore, the red-edge-effect model presented here may be a step forward towards designing tunable light sources using feldspar.

3. Site selective emission of Fe^{3+} in feldspar may have implications for quality testing of feldspar samples in luminescence geochronometry. For example, a greater disorder or multiple (sub) phases within feldspar will lead to an excitation-energy dependent emission from individual samples. Since this is a steady-state (non-decaying) signal, its application can easily be extended to the single-grain level for understanding a relationship between dose, anomalous fading, and the structural/mineralogical composition of the grain (or in principle, microscopic levels within a grain). Thus, the red edge effect in the deep red emission arising from Fe^{3+}, may eventually be used as a quality control criterion. Furthermore, the new mechanism proposed here for interaction between the excited state of Fe^{3+} and the feldspar lattice may be worth considering for other spin-forbidden defect systems.

4. The technique of direct mapping of the Sm^{2+} energy levels, using X-rays, low temperatures and site-selective spectroscopy, may be used to characterize other metastable charge trapping centers in wide bandgap materials.

5. The infra-red photoluminescence (IRPL) signal opens a new window in optical dating methods. It has importance for direct examination of the electron-trapping center in feldspar. Being a non-destructive method, the light emission in IRPL is not an issue; thus sophisticated instrumentation could be developed to probe spatial heterogeneity of IR traps even within microscopic sub-phases of single grains of feldspar. This should help to both unravel and exploit the complexity of feldspar as a chronometer. The discovery of the IRPL signal is the most important outcome of my Ph.D. and I expect that the IRPL technique will revolutionize luminescence dating.

Amit Kumar Prasad

He received his five-year integrated M.Sc. degree in Photonics from Cochin University of Science and Technology in India on ''Quantum control of photodissociation dynamics in HD^+ probed by intense femtosecond shaped laser pulses using 3D coincidence momentum imaging technique''. This work was carried out in collaboration with Weizmann Institute of Science in Israel. He has also worked as a visiting researcher at many leading national and international institutions. Amit was selected as a National Fellow of Photonics of India and a participant of seven days interaction sessions with Nobel Prize winners.

After completing his master degree, he was offered a Ph.D. position at Technical University of Denmark in the area of luminescence spectroscopy. His main contributions during his Ph.D. research are: (a) Groundbreaking discovery of Stokes-shifted, Infrared Photoluminescence (IRPL) signal from the principal trap in Feldspar: Envision as step change in optical dating technology. (b) Discovery of excitation dependent emission (a red edge effect) in Feldspar: New and simple method to measure band tail width.

Dr. Prasad will join the Technion – Israel Institute of Technology to work on the application of sequences of ultrashort laser pulses to reveal the real-time electron dynamics associated with exciton generation, fission, separation and transport in semiconductor nanostructures. His research interests cover the areas of ultrafast spectroscopy and microscopy, quantum biology, optogenetics, recollision physics, geophotonics (development of new optical dating method) and optical computing.

He has also made active efforts on the popularization of science education, especially mathematics, in his rural vicinity in India.

His favourite scientists: Prof. Ahmed H. Zewail, Prof. Richard Feynman and Dr. A. P. J. Abdul Kalam.